UNIVERSITY OF SOUTHAMPTON

Faculty of Physical and Applied Sciences

Optoelectronics Research Centre

Adaptively Shaped Advanced Ultrafast Laser Sources

Nikita Daga

Thesis for the degree of Doctor of Philosophy

May 2011

Declaration of Authorship

I, Nikita Daga, declare that this thesis titled, 'Adaptively Shaped Advanced Ultrafast Laser Sources' and the work presented in it are my own. I confirm that:

- This work was done wholly or mainly while in candidature for a research degree at this University.

- Where any part of this thesis has previously been submitted for a degree or any other qualification at this University or any other institution, this has been clearly stated.

- Where I have consulted the published work of others, this is always clearly attributed.

- Where I have quoted from the work of others, the source is always given. With the exception of such quotations, this thesis is entirely my own work.

- I have acknowledged all main sources of help.

- Where the thesis is based on work done by myself jointly with others, I have made clear exactly what was done by others and what I have contributed myself.

- Parts of this work have been published as stated in Appendix A of this thesis.

Signed: _____

Date: _____

I realise very well that the reader has no great need to know all this; but I need to tell him.

Rousseau

UNIVERSITY OF SOUTHAMPTON

Optoelectronics Research Centre

Abstract

Doctor of Philosophy

by Nikita Daga

The aim of the work presented in this thesis is to investigate adaptively shaped advanced ultrafast laser sources in the near-(NIR) and the mid-infrared (MIR) regimes. The set-up involves shaping a NIR pulse using an adaptively controlled liquid crystal spatial light modulator (LC-SLM) in a pulse shaper. The shaped NIR pulse is then transferred to the MIR via a synchronously pumped optical parametric oscillator (SPOPO).

Initially, experiments are conducted to investigate adaptive phase control of the input pulse of a 500 fs fibre-based chirped pulse amplification (CPA) system, which is an attractive pump source for the SPOPO. Results are obtained using both bulk and fibre stretchers in the system. The adaptive process was controlled by a simulated annealing algorithm and three times improvement in the autocorrelation peak intensity was demonstrated, with close to transform-limited pulse durations of 800 fs at pulse energies as high as $65\,\mu$J. Following this, a home-built adaptively shaped fibre CPA system is tested for its average power and energy scalability while maintaining high quality pulses by amplitude and phase pre-shaping. For these results, the LC-SLM is controlled using a differential evolution algorithm and a train of pulses is produced with an average power of 12.6 W at a 50 MHz repetition rate, which are compressible to high fidelity pulses with duration of 170 fs. High-quality, high-energy pulses are obtained even when the repetition rate of the system is reduced to as low as $\sim$400 kHz.

The second part of the work is to experimentally investigate the effects of various parameters in the transfer of pulse shape from the NIR to the MIR in a SPOPO with a Nd:YLF picosecond pump source and incorporating the factors, high fidelity transfer is achieved. The pulse was characterised using the cross-correlation sonogram technique. Cross-correlation based frequency resolved optical gating is also studied as the method of idler pulse characterisation and the advantages and disadvantages compared to the sonogram technique are discussed.

Finally, the two technologies of an adaptively shaped ultrafast fibre CPA system and the pulse shape transfer in a SPOPO are experimentally combined to form an advanced adaptively shaped ultrafast laser source for various applications.

Contents

Acknowledgements

This thesis and the work presented here would not be possible without the help and support of many people during the course of my PhD. First and foremost, I would like to express sincere gratitude to my supervisor, Prof. David P. Shepherd, whose expertise, patience, and understanding added considerably to my PhD experience.

This work would not have been possible without my *on-site Guru*, Hazel Hung, in whom I have also found a very good friend. I cannot thank her enough for all her support throughout. I would also like to thank Dr. Sarah Stebbings, for just being her, ever so helpful and enthusiastic. She helped immensely in keeping my morale up even when things were looking bleak. For helping me in the lab, especially with the long cavity length tunings and in grabbing things from the shelves far above my reach, I would like to thank Florian Kienle, whose witty remarks made the lab a fun and happy place to be. I surely could not have asked for a better team to work with.

Thanks also go to Dr. Jerry Prawiharjo and Dr. Naveed Naz whose in-depth knowledge of Matlab and C++ codes helped me speed up the lab work. I am grateful to Prof. David C. Hanna for his lucid explanations of even the most complex principles which helped me not only in the lab but also better my understanding of the subject. I would also like to thank Dr. Jeremy Frey for his invaluable input on the sum frequency generation experiment.

I would like to extend my gratitude to Dr. Jonathan Price and Dr. Fei He for their perseverance and patience during the collaborative work on the fibre CPA system. I would also like to acknowledge the help of Corin Gawith from Covesion for providing the PPLN crystal used in the OPO and XFROG set-ups.

I convey special acknowledgement to Eve Smith and the administrative staff at the ORC for their indispensable help in dealing with everyday work issues, small and big alike, to make life easier for us at the ORC. Thanks also go to Simon Butler and the team of technicians for modifying the many bits in the workshop to suit the needs of the experiment.

I am particularly grateful to the EPSRC for funding the project and my PhD.

Many thanks also go to Linda and Prof. Rick Trebino for their encouragement and valuable discussions on various occasions which has greatly helped me in the lab as well as while writing this thesis.

Outside of lab, I would like to thank the teams and members of the OSASC at the University of Southampton, IoP : Physics in the field, Royal Society summer science

Abbreviations

2D	**T**wo **d**imensional
AC	**A**uto**c**orrelation
AOCC	**A**daptive **O**ptimal **C**oherent **C**ontrol
AOM	**A**cousto-**o**ptic **m**odulator
AR	**A**nti-**r**eflection
ASE	**A**mplified **s**timulated **e**mission
CARS	**C**oherent **A**nti-Stokes **R**aman **S**cattering
CCD	**C**harge **c**oupled **d**evice
CCS	**C**ross-**c**orrelation **s**onogram
CPA	**C**hirped **p**ulse **a**mplification
CW	**C**ontinuous **w**ave
DDL	**D**ispersive **d**elay **l**ine
DE	**D**ifferential **E**volution
DFG	**D**ifference **f**requency **g**eneration
DM	**D**ichroic **m**irror
EA	**E**volutionary **a**lgorithm
EOM	**E**lectro-**o**ptic **m**odulator
FFT	**F**ast **F**ourier **t**ransform
FRAC	**F**ringe-**r**esolved **au**to-**c**orrelation
FROG	**F**requency **r**esolved **o**ptical **g**ating
fs	**F**emtosecond
FWHM	**F**ull **w**idth at **h**alf **m**aximum
GDD	**G**roup **d**elay **d**ispersion
GSA	**G**eneralised **s**imulated **a**nnealing
GVD	**G**roup **v**elocity **d**ispersion

GVM	**G**roup **v**elocity **m**ismatch
HR	**H**ighly **r**eflecting
HT	**H**ighly **t**ransmitting
JADE	**S**elf-**a**daptive **d**ifferential **e**volution
LC	**L**iquid **c**rystal
LC-SLM	**L**iquid **c**rystal **s**patial **l**ight **m**odulator
LD	**L**aser **d**iode
LMA	**L**arge **m**ode **a**rea
LWP	**L**ong **w**ave **p**ass
MIR	**M**id-**i**nfrared
ND	**N**eutral **d**ensity
NIR	**N**ear **i**nfrared
nm	**N**ano**m**etre
ns	**N**ano**s**econd
OBPF	**O**ptical **b**and-**p**ass **f**ilter
OC	**O**utput **c**oupler
OI	**O**ptical **i**solator
OPA	**O**ptical **p**arametric **a**mplification
OPO	**O**ptical **p**arametric **o**scillator
ORC	**O**ptoelectronics **R**esearch **C**entre
OSA	**O**ptical **s**pectrum **a**nalyser
PA	**P**re-/**p**ower **a**mplifier
PBS	**P**olarisation **b**eam **s**plitter
PCF	**P**hotonic **c**rystal **f**ibre
PCGP	**P**rinciple **c**omponent **g**eneralized **p**rojections
PG-FROG	**P**olarisation **g**ate **FROG**
PM	**P**olarisation **m**aintaining
PMT	**P**hoto-**m**ultiplier **t**ube
PPLN	**P**eriodically **p**oled **L**ithium **n**iobate
ps	**P**ico**s**econd
QPM	**Q**uasi **p**hase **m**atching
RHS	**R**ight **h**and **s**ide
RMS	**R**oot **m**ean **s**quare

SA	**S**imulated **a**nnealing
SD	**S**elf **d**iffracting
SD-FROG	**S**elf **d**iffraction **FROG**
SESAM	**Se**miconductor **s**aturable **a**bsorber **m**irror
SFG	**S**um **f**requency **g**enereation
SFM	**S**um **f**requency **m**ixing
SH	**S**econd **h**armonic
SHG	**S**econd **h**armonic **g**eneration
SLM	**S**patial **l**ight **m**odulator
SM	**S**ingle **m**ode
SPM	**S**elf **p**hase **m**odulation
SPOPO	**S**ynchronously **p**umped **o**ptical **p**aramteric **o**scillator
SSO	**S**elf **s**imilar **o**scillator
TBP	**T**ime **b**andwidth **p**roduct
TOD	**T**hird **o**rder **d**ispersion
TPA	**T**wo **p**hoton **a**bsorption
TWO	**T**emporal **w**alk-**o**ff
UV	**U**ltraviolet
VSFS	**V**ibrational **s**um **f**requency **s**pectroscopy
WDM	**W**avelength **d**ivision **m**ultiplexer
XFROG	**C**ross-correlation **FROG**

For Mum and Dad,

and in loving memory of

Masi and Nari Babaji.

Chapter 1

Introduction

1.1 Coherent Control

Bond selective manipulation of matter with light has been a study of great interest to physicists, chemists and biologists. With ultrafast optical pulses, the bond excitation occurs faster than the rapid redistribution of the energy away from the specific bond making it possible to drive a chemical reaction towards a desired product or even away from an undesired one [1]. Although many experiments have already achieved coherent control in the visible and near-infrared (NIR) wavelength regimes, the most common molecular vibrational modes are in the mid-infrared (MIR) region. Therefore, shaped femtosecond pulses in this fingerprint regime become important. These shaped pulses find various applications in driving conformational changes in proteins, spectroscopy, coherent control and imaging [2–6].

Active manipulation of molecules using coherent light was first suggested by Brumer and Shapiro [7]. It involves the excitation of a mode through two or more pathways simultaneously, resulting in a quantum mechanical interference between the reaction pathways. The two pathways interfere constructively or destructively depending on the relative phase of two continuous-wave (CW) lasers. By controlling the relative phases and amplitudes of the light sources, the reaction can be directed to the desired outcome. Another technique of coherent control was suggested by Tannor and Rice [8, 9] which suggested using pairs of short pulses to manipulate quantum mechanical wave packets.

In other words, this can be viewed as optimal control in which an *optimally* shaped electromagnetic field is used to obtain the desired final quantum mechanical state [10]. Judson and Rabitz [2] then proposed the Adaptive Optimal Coherent Control (AOCC) scheme in 1992. In this arrangement, a feedback loop was incorporated along with a learning algorithm into the experimental set-up. Due to the adaptive nature, the need for prior information of the molecular system to be controlled was eliminated.

With progress in the field of experimental ultrafast optics, the first demonstration of AOCC in a molecular system was performed in 1997 [11]. In the experiment, population transfer to the excited state in a dye molecule was optimised using femtosecond pulses shaped by an acousto-optic pulse shaper and it included a feedback loop. Control of independent chemical reaction pathways [12], molecular dissociation [5, 13] and molecular manipulation [5, 14, 15] are now possible due to further developments in the AOCC method. Experiments related to biochemical and biomedical applications [6, 16] have successfully demonstrated control of even highly complex molecular systems using this technique.

All of the experiments listed above were carried out using visible or NIR radiation. Very few experiments are found at the ultraviolet (UV) or MIR wavelength regimes due to the limitations of pulse shaping apparatus. Pulse shaping with deformable mirrors has been demonstrated [17] in this regime, but due to the long wavelengths of MIR radiation, the mirror movement has to be large for a significant phase change. Moreover, the pixel resolution of such a device is poor. The commonly used LC-SLM and acousto-optic modulators (AOM) have much greater resolution, but tend to absorb UV and MIR radiation. Roth et al. [18] have demonstrated adaptive pulse shaping in the UV with a fused silica AOM thus opening opportunities for AOCC in a new wavelength region. Lately, shaped UV pulses at the third harmonic of Titanium sapphire have been demonstrated using a LC-SLM [19].

Direct pulse shaping in the MIR has been demonstrated with a free-electron laser [20] but the method used could generate only simple, linearly chirped pulses which are also not programmable. Such a MIR source has been used in successful demonstrations

of coherent control [21–24] leading to molecular dissociation, but this method is not capable of dynamically finding the optimum linear chirp required.

Coherent control in the MIR regime can be achieved through indirect pulse shaping for producing arbitrarily shaped pulses. It involves shaping a visible or NIR pulse using a LC-SLM or AOM before transferring the pulse shape to the MIR via a nonlinear optical process. Indirect pulse shaping in the MIR has been shown via difference frequency generation (DFG) [25, 26], and optical parametric amplification (OPA) [27, 28]. Recently, Shim et al. reported direct pulse shaping in the MIR using a germanium AOM [29, 30].

Prior experiments in the Optical Parametric Oscillator (OPO) group at the Optoelectronics Research centre (ORC) have successfully demonstrated adaptive pulse shaping using a synchronously pumped optical parametric oscillator (SPOPO), allowing idler wavelengths up to $3.5\,\mu$m. Furthermore, the principles for applying adaptive control, including implementation of a simulated annealing (SA) algorithm to the system, have already been explored. Indirect control of the idler has been achieved via optimisation of a two photon absorption (TPA) signal demonstrating simple pulse compression and the generation of compressed double pulse with variable time delay [31].

More recently, the fidelity of parametric transfer in a SPOPO has been studied numerically and experimentally [32]. This included a detailed numerical investigation of parametric transfer via DFG [33], followed by a numerical study to understand the effects of various parameters on fidelity of transfer in a SPOPO [34]. Chapter 7 of the work presented in this thesis proceeds further from here to support these numerical investigations through experimental demonstrations. In that chapter, experimental demonstration of transfer using a solid state bulk pico-second (ps) pump source is demonstrated. The work is then extended to use a femtosecond (fs) fibre pump source in place of the bulk ps source. Successful preliminary demonstration of pulse shape transfer attempts, to optimise surface sum frequency mixing, which has potential application in analysing surfaces and interfaces for biochemistry and biophysics [35–37], are highlighted in the final chapter with a possible direction for future work.

Besides coherent control, the adaptive pulse shaping technique has also found various applications in pulse compression [38], ultrashort pulse propagation in fibres [39], chirped pulse amplification (CPA) [40, 41] etc. This is discussed in detail in the following section.

1.2 Adaptive control of ultrashort pulse propagation in fibres

High energy femtosecond pulses are required for a wide range of industrial and scientific applications such as ultrafast spectroscopy, pumping parametric devices, material processing and plasma-based x-ray generation. High energy femtosecond pulses can be generated using the CPA technique where the pulse is initially stretched, then amplified to avoid the nonlinear effects and system damage, and later recompressed [42]. Compared to the traditional bulk crystal and glass laser sources, Yb-fibre based systems can be directly diode-pumped, have high gain and suffer less from thermo-optical problems, making them attractive high power laser sources [43]. Further, coupling with continuous-wave diode pumping has allowed the realisation of compact, ultrafast laser systems with more than $100\,\mathrm{W}$ average power at various repetition rates [43, 44]. Energy levels reaching the milli-joule levels have also recently been demonstrated with the use of novel fibre designs such as the photonic crystal fibre (PCF) [45]. However, due to long total device length of up to several metres and a highly confined mode area, these devices suffer from nonlinear effects such as self-phase modulation (SPM). Imperfect correction of spectral phase distortions caused by high order dispersion and residual nonlinear effects in the stretcher and amplifier can lead to non-transform-limited pulses at the output of the compressor. These effects can degrade the final pulse quality, limiting the maximum available peak power from the femtosecond source.

One of the methods to overcome these pulse distortions is to incorporate an adaptive pulse shaper [46] in the set-up to control the phase (and/or amplitude) of the pulses. This technique has been used with Ti:Sapphire lasers and CPA systems to overcome SPM, as well as the induced distortions due to the residual stretcher/compressor dispersion mismatch [38, 40, 41, 47]. Adaptive pulse shaping has also been used to control the

propagation of ultrashort pulses in optical fibres [48]. Recently, there have been two experimental demonstrations of combining adaptive pulse shaping with fibre-based CPAs. In the first report, Schimpf et al. [49] describe pre-shaping the spectral amplitude of the pulse and show high quality pre-compensation of low average power pulses at B-integrals [see chapter 4] as high as 16. According to the method employed by the authors, the influence of the dominant nonlinear effect of SPM is controlled via the intensity profile. The set-up is used to shape to a certain spectral shape only at the output. The pulse shaper is usually used for pre-compensation due to power handling limitations and efficiency considerations imposed by the system [50]. For a CPA set up, dispersion, nonlinearity and gain narrowing effects require attention and the use of an adaptive system cuts down the need for computing the design of a compensation element. In a later report, we have demonstrated [51] the use of pre-shaping the spectral phase in a fibre CPA system. The peak of the autocorrelation trace of the final compressed pulse was used as the feedback parameter in the adaptive control loop. A three-fold increase in the autocorrelation peak intensity was reported for near-transform-limited recompressed pulses with durations of $800\,\mathrm{fs}$ at pulse energies of $65\,\mu\mathrm{J}$ and a corresponding B-integral of ~ 8. This experiment is discussed in detail in chapter 4 of this report. In chapter 5, a dual layer LC-SLM is implemented in a fibre CPA system for adaptive amplitude and phase pre-shaping. The dual layer LC-SLM was controlled using a differential evolution (DE) algorithm. The system produced a train of pulses with an average power of $12.6\,\mathrm{W}$ at $50\,\mathrm{MHz}$ repetition rate. These were compressible to pulses of $170\,\mathrm{fs}$ duration.

1.3 Motivation and Aim

With the growing need for adaptively controlled fibre-based MIR sources for various applications, this project aims at testing the feasibility of an adaptively shaped MIR femtosecond source for various applications such as coherent control, surface sum frequency spectroscopy, etc. We employ an indirect pulse shaping technique to achieve transfer of pulse shape from the NIR pump to the MIR idler via parametric frequency conversion of an optical parametric oscillator (OPO). OPOs offer broad and continuous tunability from one source making them very attractive for various applications [52]. In

addition, with the use of a pulse shaper controlled by an evolutionary algorithm in the set-up, closed-loop adaptive control of the idler can be achieved, optimising the pulse shape for these applications. As a result, this instrument will render adaptively shaped femtosecond pulses in the NIR and the MIR waveband.

The content of the thesis is thus organised as follows. The general background theory and technology involved in the processes of pulse generation, propagation and manipulation are discussed in chapter 2. Chapter 3 then details the various pulse characterisation techniques used in the experiments along with an experimental comparison between two MIR characterisation techniques. Experimental investigation of adaptive phase control of the input pulse of a high pulse energy ($65\,\mu$J) CPA system is presented in chapter 4. This is followed in chapter 5 by a detailed description and characterisation of a fibre-based CPA system with adaptive phase and amplitude shaping, which is then tested for its average power scalability while maintaining very high quality pulses of $\sim$300 fs duration. In chapter 6 the versatility of this system is tested by changing the repetition rate and hence the pulse energy to see the range of nonlinearity that the adaptive shaping can compensate for.

The aim of the final experiment presented in chapter 7 is to achieve control over the pulse shape and high fidelity spectral transfer from the pump to the idler by investigating the effects of various parameters on the fidelity of shape transfer. In the second part of this chapter, the fibre system described in the previous chapters is used as the pump source for the OPO for future coherent control experiments. This then leads to the concluding chapter, chapter 8, which summarises the results obtained thus far and proposes possible experiments for the future.

References

[1] N. Bloembergen and A. H. Zewail, "Energy redistribution in isolated molecules and the question of mode-selective laser chemistry revisited," *Journal of Physical Chemistry* **88**(23), pp. 5459–5465, 1984.

[2] R. S. Judson and H. Rabitz, "Teaching lasers to control molecules," *Physical Review Letters* **68**(10), pp. 1500–1503, 1992.

[3] R. N. Zare, "Laser control of chemical reactions," *Science* **279**(5358), pp. 1875–1879, 1998.

[4] A. P. Peirce, M. A. Dahleh, and H. Rabitz, "Optimal-control of quantum-mechanical systems - existence, numerical approximation, and applications," *Physical Review A* **37**(12), pp. 4950–4964, 1988.

[5] R. J. Levis, G. M. Menkir, and H. Rabitz, "Selective bond dissociation and rearrangement with optimally tailored, strong-field laser pulses," *Science* **292**(5517), pp. 709–713, 2001.

[6] J. M. Dela Cruz, I. Pastirk, M. Comstock, V. V. Lozovoy, and M. Dantus, "Use of coherent control methods through scattering biological tissue to achieve functional imaging," *PNAS* **101**, pp. 16996–17001, 2004.

[7] P. Brumer and M. Shapiro, "Control of unimolecular reactions using coherent light," *Chemical Physics Letters* **126**(6), p. 541, 1986.

[8] D. J. Tannor and S. A. Rice, "Control of selectivity of chemical reaction via control of wave packet evolution," *The Journal of Chemical Physics* **83**(10), pp. 5013–5018, 1985.

[9] D. J. Tannor, R. Kosloff, and S. A. Rice, "Coherent pulse sequence induced control of selectivity of reactions: Exact quantum mechanical calculations," *The Journal of Chemical Physics* **85**(10), pp. 5805–5820, 1986.

[10] S. Shi, A. Woody, and H. Rabitz, "Optimal control of selective vibrational excitation in harmonic linear chain molecules," *The Journal of Chemical Physics* **88**(11), pp. 6870–6883, 1988.

[11] C. J. Bardeen, V. V. Yakovlev, K. R. Wilson, S. D. Carpenter, P. M. Weber, and W. S. Warren, "Feedback quantum control of molecular electronic population transfer," *Chemical Physics Letters* **280**(1-2), pp. 151–158, 1997.

[12] A. Assion, T. Baumert, M. Bergt, T. Brixner, B. Kiefer, V. Seyfried, M. Strehle, and G. Gerber, "Control of chemical reactions by feedback-optimized phase- shaped femtosecond laser pulses," *Science* **282**(5390), pp. 919–922, 1998.

[13] M. Bergt, T. Brixner, B. Kiefer, M. Strehle, and G. Gerber, "Controlling the femto-chemistry of $Fe(CO)_5$," *Journal of Physical Chemistry A* **103**(49), pp. 10381–10387, 1999.

[14] B. J. Pearson, J. L. White, T. C. Weinacht, and P. H. Bucksbaum, "Coherent control using adaptive learning algorithms," *Physical Review A* **6306**(6), pp. 063412–(1–12), 2001.

[15] T. Brixner, N. H. Damrauer, P. Niklaus, and G. Gerber, "Photoselective adaptive femtosecond quantum control in the liquid phase," *Nature* **414**(6859), pp. 57–60, 2001.

[16] J. L. Herek, W. Wohlleben, R. J. Cogdell, D. Zeidler, and M. Motzkus, "Quantum control of energy flow in light harvesting," *Nature* **417**(6888), pp. 533–535, 2002.

[17] E. Zeek, K. Maginnis, S. Backus, U. Russek, M. Murnane, G. Mourou, H. Kapteyn, and G. Vdovin, "Pulse compression by use of deformable mirrors," *Optics Letters* **24**(7), pp. 493–495, 1999.

[18] M. Roth, M. Mehendale, A. Bartelt, and H. Rabitz, "Acousto-optical shaping of ultraviolet femtosecond pulses," *Applied Physics B-Lasers and Optics* **80**(4-5), pp. 441–444, 2005.

[19] P. Nuernberger, G. Vogt, R. Selle, S. Fechner, T. Brixner, and G. Gerber, "Generation of shaped ultraviolet pulses at the third harmonic of titanium-sapphire femtosecond laser radiation," *Applied Physics B: Lasers and Optics* **88**(4), pp. 519–526, 2007.

[20] G. Knippels, A. v. d. Meer, R. Mols, P. v. Amersfoort, R. Vrijen, D. Maas, and N. L.D., "Generation of frequency-chirped pulses in the far-infrared by means of a sub-picosecond free-electron laser and an external pulse shaper," *Optics Communications* **118**, pp. 546–550, 1995.

[21] L. Windhorn, T. Witte, J. S. Yeston, D. Proch, M. Motzkus, K. L. Kompa, and W. Fuss, "Molecular dissociation by mid-IR femtosecond pulses," *Chemical Physics Letters* **357**(1-2), pp. 85–90, 2002.

[22] D. J. Maas, D. I. Duncan, R. B. Vrijen, W. J. van der Zande, and L. D. Noordam, "Vibrational ladder climbing in NO by (sub)picosecond frequency-chirped infrared laser pulses," *Chemical Physics Letters* **290**(1-3), pp. 75–80, 1998.

[23] V. D. Kleiman, S. M. Arrivo, J. S. Melinger, and E. J. Heilweil, "Controlling condensed-phase vibrational excitation with tailored infrared pulses," *Chemical Physics* **233**(2-3), pp. 207–216, 1998.

[24] L. Windhorn, J. S. Yeston, T. Witte, W. Fuss, M. Motzkus, D. Proch, K. L. Kompa, and C. B. Moore, "Getting ahead of ivr: A demonstration of mid-infrared induced molecular dissociation on a sub-statistical time scale," *Journal of Chemical Physics* **119**(2), pp. 641–645, 2003.

[25] N. Belabas, J. P. Likforman, L. Canioni, B. Bousquet, and M. Joffre, "Coherent broadband pulse shaping in the mid infrared," *Optics Letters* **26**(10), pp. 743–745, 2001.

[26] T. Witte, K. L. Kompa, and M. Motzkus, "Femtosecond pulse shaping in the mid infrared by difference-frequency mixing," *Applied Physics B-Lasers and Optics* **76**(4), pp. 467–471, 2003.

[27] H. S. Tan and W. S. Warren, "Mid infrared pulse shaping by optical parametric amplification and its application to optical free induction decay measurement," *Optics Express* **11**(9), pp. 1021–1028, 2003.

[28] H. S. Tan, E. Schreiber, and W. S. Warren, "High-resolution indirect pulse shaping by parametric transfer," *Optics Letters* **27**(6), pp. 439–441, 2002.

[29] S. H. Shim, D. B. Strasfeld, E. C. Fulmer, and M. T. Zanni, "Femtosecond pulse shaping directly in the mid-IR using acousto-optic modulation," *Optics Letters* **31**(6), pp. 838–840, 2006.

[30] S. H. Shim, D. B. Strasfeld, and M. T. Zanni, "Generation and characterization of phase and amplitude shaped femtosecond mid-IR pulses," *Optics Express* **14**(26), pp. 13120–13130, 2006.

[31] N. A. Naz, H. S. S. Hung, M. V. O'Connor, D. C. Hanna, and D. P. Shepherd, "Adaptively shaped mid-infrared pulses from a synchronously pumped optical parametric oscillator," *Optics Express* **13**(21), pp. 8400–8405, 2005.

[32] H. S. S. Hung, N. A. Naz, J. Prawiharjo, D. C. Hanna, and D. P. Shepherd, "Parametric transfer in a synchronously pumped optical parametric oscillator," *Conference on Lasers and Electro-optics, USA (Optical Society of America)* **CtuZ6**, 2006.

[33] J. Prawiharjo, H. S. S. Hung, D. C. Hanna, and D. P. Shepherd, "Theoretical and numerical investigations of parametric transfer via difference-frequency generation for indirect mid-infrared pulse shaping," *Journal of the Optical Society of America B-Optical Physics* **24**(4), pp. 895–905, 2007.

[34] J. Prawiharjo, *Frequency-resolved optical gating in periodically-poled lithium niobate waveguide devices.* PhD thesis, University of Southampton, 2005.

[35] N. Ji, V. Ostroverkhov, C. S. Tian, and Y. R. Shen, "Characterization of vibrational resonances of water-vapor interfaces by phase-sensitive sum-frequency spectroscopy," *Physical Review Letters* **100**(9), p. 096102, 2008.

[36] C. M. Johnson, A. B. Sugiharto, and S. Roke, "Surface and bulk structure of poly-(lactic acid) films studied by vibrational sum frequency generation spectroscopy," *Chemical Physics Letters* **449**(1-3), pp. 191–195, 2007.

[37] C. M. Johnson, E. Tyrode, S. Baldelli, M. W. Rutland, and C. Leygraf, "A vibrational sum frequency spectroscopy study of the liquid-gas interface of acetic acid-water mixtures: 1. surface speciation," *Journal of Physical Chemistry B* **109**(1), pp. 321–328, 2005.

[38] D. Yelin, D. Meshulach, and Y. Silberberg, "Adaptive femtosecond pulse compression," *Optics Letters* **22**(23), pp. 1793–1795, 1997.

[39] A. M. Weiner, J. P. Heritage, and E. M. Kirschner, "High-resolution femtosecond pulse shaping," *Journal of the Optical Society of America B-Optical Physics* **5**(8), pp. 1563–1572, 1988.

[40] A. Efimov and D. H. Reitze, "Programmable dispersion compensation and pulse shaping in a 26-fs chirped-pulse amplifier," *Optics Letters* **23**(20), pp. 1612–1614, 1998.

[41] A. Efimov, M. D. Moores, B. Mei, J. L. Krause, C. W. Siders, and D. H. Reitze, "Minimization of dispersion in an ultrafast chirped pulse amplifier using adaptive learning," *Applied Physics B-Lasers and Optics* **70**, pp. S133–S141, 2000.

[42] D. Strickland and G. Mourou, "Compression of amplified chirped optical pulses," *Optics Communications* **56**(3), pp. 219–221, 1985.

[43] F. Roser, D. Schimpf, O. Schmidt, B. Ortac, K. Rademaker, J. Limpert, and A. Tünnermann, "90 w average power 100 µj energy femtosecond fiber chirped-pulse amplification system," *Optics Letters* **32**(15), pp. 2230–2232, 2007.

[44] F. Roser, J. Rothhard, B. Ortac, A. Liem, O. Schmidt, T. Schreiber, J. Limpert, and A. Tünnermann, "131 w 220 fs fiber laser system," *Optics Letters* **30**(20), pp. 2754–2756, 2005.

[45] F. Roser, T. Eidam, J. Rothhardt, O. Schmidt, D. N. Schimpf, J. Limpert, and A. Tünnermann, "Millijoule pulse energy high repetition rate femtosecond fiber chirped-pulse amplification system," *Optics Letters* **32**(24), pp. 3495–3497, 2007.

[46] A. M. Weiner, "Femtosecond pulse shaping using spatial light modulators," *Review of Scientific Instruments* **71**(5), pp. 1929–1960, 2000.

[47] K. Ohno, T. Tanabe, and F. Kannari, "Adaptive pulse shaping of amplified femtosecond pulse laser in phase and amplitude by directly referring to frequency resolved optical gating traces," *Ultrafast Phenomena* XIII **71**, pp. 232–234, 2003.

[48] F. G. Omenetto, D. H. Reitze, B. P. Luce, M. D. Moores, and A. J. Taylor, "Adaptive control methods for ultrafast pulse propagation in optical fibers," *IEEE Journal of Selected Topics in Quantum Electronics* **8**(3), pp. 690–698, 2002.

[49] D. N. Schimpf, J. Limpert, and A. Tünnermann, "Controlling the influence of spm in fiber-based chirped-pulse amplification systems by using an actively shaped parabolic spectrum," *Optics Express* **15**(25), pp. 16945–16953, 2007.

[50] M. A. Dugan, J. X. Tull, and W. S. Warren, "High-resolution acousto-optic shaping of unamplified and amplified femtosecond laser pulses," *Journal of the Optical Society of America B-Optical Physics* **14**(9), pp. 2348–2358, 1997.

[51] F. He, H. S. S. Hung, J. H. V. Price, N. K. Daga, N. Naz, J. Prawiharjo, D. C. Hanna, D. P. Shepherd, D. J. Richardson, J. W. Dawson, C. W. Siders, and C. P. J. Barty, "High energy femtosecond fiber chirped pulse amplification system with adaptive phase control," *Optics Express* **16**(8), pp. 5813–5821, 2008.

[52] G. Warmbier, "Crystal technology aids development of OPOs," *http://optics.org/cws/article/research/23766* , 2005.

Chapter 2

Theoretical Overview

This chapter outlines the basic theoretical background needed for a better understanding of the results presented in the experimental chapters that follow. Much of these principles presented here have already been well discussed in various books and papers [1, 2]. For the sake of brevity, only those concepts that are most directly related to the experimental results presented in this thesis are outlined here.

This chapter deals with the earlier processes of pulse generation including optical parametric processes and pulse manipulation detailed in sections 2.1 and 2.2 respectively whereas the next chapter is dedicated to pulse characterisation techniques.

2.1 Nonlinear Optics and Pulse Generation

For an electric field $\mathbf{E}$ applied to a medium, $\mathbf{P}$ is the induced dipole polarisation per unit volume reflecting the response of the medium to it. Polarisation can be expressed mathematically as a series expansion as indicated in equation 2.1.

$$P = \varepsilon_0[\chi E + \chi^{(2)}E^2 + \chi^{(3)}E^3 + ...] \tag{2.1}$$

here, ε_0 is the electric permittivity in vacuum. The first term on the right-hand-side (RHS) of the equation is a linear component whereas the higher order terms arise from the *nonlinear* response of the material. The physical origin of the nonlinear terms is due to the nonlinear deformation of the outer, loosely bound, electrons of an atomic system when subjected to a high intensity. The quantities P and E here are taken to be scalar quantities for ease of calculations. When they are considered as vectors, $\chi^{(n)}$ becomes the nth order tensor with rank n+1. The second order nonlinear susceptibility, $\chi^{(2)}$,

gives rise to processes like second harmonic generation (SHG) and difference frequency generation (DFG), which is used in the OPO for frequency conversion. The third order nonlinear optical susceptibility ($\chi^{(3)}$) interactions on the other hand, lead to SPM which is important in the fibre CPA systems.

2.1.1 Optical Parametric Processes

An important component of our experimental set-up is the OPO, which performs the crucial frequency conversion using an optical parametric process. This is a process involving second order nonlinear susceptibility, $\chi^{(2)}$, which is present only in a non-centrosymmetric crystalline medium. The SPOPO used in the set-up employs the DFG process which is detailed in the following paragraphs.

Difference Frequency Generation

Consider pump, signal and idler photons denoted by subscripts p, s and i respectively. When a photon (pump) is split into two lesser energy photons (signal and idler), energy conservation requires equation 2.2 to be satisfied. This process is illustrated in figure 2.1.
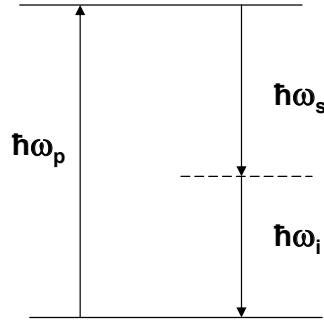
FIGURE 2.1: Pump generating signal and idler.

$$\hbar\omega_p = \hbar\omega_s + \hbar\omega_i \tag{2.2}$$

Here $\hbar$ is Planck's constant, h, divided by 2π and $\omega_{(p,s,i)}$ is the angular frequency. This process is called difference frequency generation and it is at the heart of the OPO operation. The pump field interacts with the signal field, diminishing as it passes through a nonlinear medium, generating idler and more signal in the process. As a result, we get signal amplification which provides the optical gain required to sustain the oscillation

within the OPO resonator. The initial signal photon needed to start the process within an OPO arises from spontaneous parametric fluorescence.

It is important to have constructive addition of the fields generated along the entire length of the nonlinear crystal, driven by the nonlinear polarisation. That is, the field generated at any given point, after travelling to another location, must be in phase with the emission from the source at that point. In the case that the fields are not in phase, the generated intensity begins to decrease due to destructive interference. This gives rise to the need for phase matching. Phase matching is achieved by satisfying the momentum conservation equation 2.3 where $\mathbf{k}$ is the momentum wavevector.

$$\mathbf{k}_p = \mathbf{k}_s + \mathbf{k}_i \tag{2.3}$$

It is important to note here that $\mathbf{k}$ is a function of n which in turn is a function of the wavelength λ. Equation 2.3 is not satisfied automatically due to chromatic dispersion in the crystal as the pulse propagates through it. This requires manipulation of the above equation to achieve momentum conservation and leads to the equation 2.4.

$$\Delta\mathbf{k} = \mathbf{k}_p - \mathbf{k}_s - \mathbf{k}_i \tag{2.4}$$

When there is a momentum mismatch, the length over which the accumulated phase difference between the interacting waves is π is defined as the coherence length L_c. Mathematically,

$$\Delta\mathbf{k} = \frac{\pi}{L_c} \tag{2.5}$$

$$L_c = \frac{\pi}{k_p - k_s - k_i} = \frac{1}{2(\frac{n_p}{\lambda_p} - \frac{n_s}{\lambda_s} - \frac{n_i}{\lambda_i})} \tag{2.6}$$

where λ is the wavelength, $k = \frac{2\pi n}{\lambda}$ is the magnitude of the wave vector $\mathbf{k}$, and n is the index of refraction. One of the deliberate methods of phase matching, used in our system, is quasi phase matching (QPM), which is discussed in detail in the next subsection.

2.1.2   Quasi Phase Matching

In a non-phase-matched nonlinear interaction, we can get parametric gain up to a point where the generated field intensity reaches a maximum in one coherence length after which it begins to die out and then rise again after another distance equal to L_c and so on (see figure 2.2). There is a phase difference of π accumulated for each coherence length that the wave travels. Reversal of the phase to $-\pi$ after each L_c would then compensate for this phase difference. This change is brought about by reversing the sign of the nonlinear susceptibility every coherence length. This is easily achieved in ferroelectric materials, such as $LiNbO_3$, by reversal of the ferroelectric domain polarity with a period, Λ, equal to twice the coherence length. With $\mathbf{k}_G$ as the reciprocal wave-vector describing the periodicity of the grating, there is a corresponding extra term added in the modified equation 2.3. The phase mismatch is now given by equation 2.7.
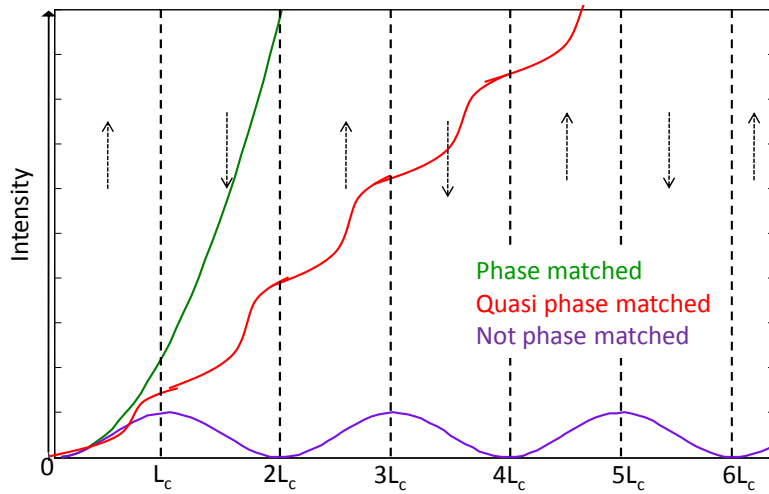
FIGURE 2.2: Parametric gain for non-phase-matched, perfectly phase-matched and quasi-phase-matched conditions.

$$\Delta\mathbf{k} = \mathbf{k}_p - \mathbf{k}_s - \mathbf{k}_i - \mathbf{k}_G \qquad (2.7)$$

This kind of periodic poling is achieved in $LiNbO_3$ by application of a spatially patterned electric field to reverse the domains. It allows collinear phase matched propagation, generation across the entire transparency range, and exploitation of the largest nonlinear coefficient. A microscopic image of one of the periodically poled lithium niobate (PPLN) crystals used for the experiments is shown in figure 2.3. The poled regions can be distinctly seen.
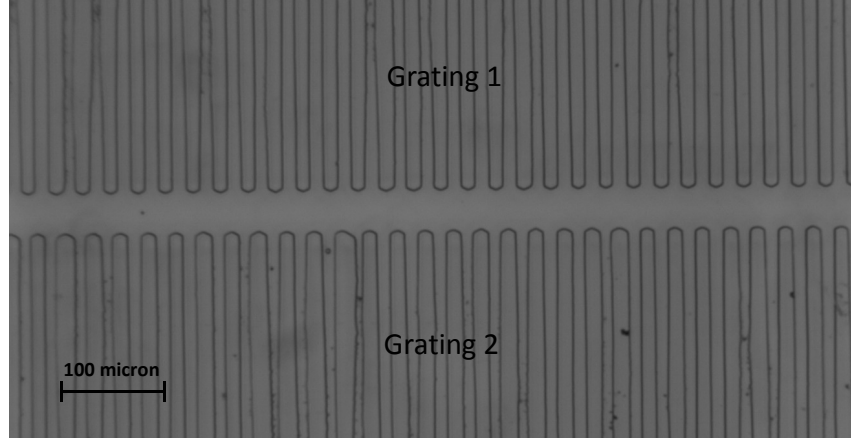
FIGURE 2.3: Microscopic image of a part of a periodically poled lithium niobate crystal. Two gratings of slightly different periodicity are shown. The crystal for these experiments was provided by Corin Gawith. The scale is indicated on the figure.

2.1.3 Parametric Gain and bandwidth

From the well-known Maxwell's wave equations, the coupled-wave equations can be derived [3]. This set of equations describe the interaction of the pump, signal and idler fields and assuming collinear pulse propagation along z direction in a bulk crystal, are expressed as,

$$\frac{\partial A_p}{\partial z} + \frac{1}{u_p}\frac{\partial A_p}{\partial t} + i\frac{b_p}{2}\frac{\partial^2 A_p}{\partial t^2} = 2i\alpha_p A_i A_s \exp[-i\Delta kz] \,, \tag{2.8}$$

$$\frac{\partial A_s}{\partial z} + \frac{1}{u_s}\frac{\partial A_s}{\partial t} + i\frac{b_s}{2}\frac{\partial^2 A_s}{\partial t^2} = 2i\alpha_s A_i^* A_p \exp[+i\Delta kz] \,, \tag{2.9}$$

$$\frac{\partial A_i}{\partial z} + \frac{1}{u_i}\frac{\partial A_i}{\partial t} + i\frac{b_i}{2}\frac{\partial^2 A_i}{\partial t^2} = 2i\alpha_i A_s^* A_p \exp[+i\Delta kz] \,, \tag{2.10}$$

where u_j is the group velocity and b_j is the group velocity dispersion (GVD) and the slowly varying envelope, $A_j = A_j(z,t)$, is defined by,

$$E_j(z,t) = A_j(z,t)\exp[i(k_j z - \omega_j t)] + \ c.c. \tag{2.11}$$

Assuming, CW operation, and no pump depletion, it can be shown that [2],

$$A_s(z) \propto \sinh(gL) \,, \tag{2.12}$$

$$A_p(z) \propto \cosh(gL) \,, \tag{2.13}$$

where L is the crystal length and g is,

$$g = \left[\Gamma^2 - \left(\frac{\Delta k}{2} \right)^2 \right]^{1/2} , \tag{2.14}$$

where Δk is the phase mismatch and Γ^2 is the parametric gain coefficient defined as,

$$\Gamma^2 = \frac{2\omega_i \omega_s |d_{eff}|^2 I_p}{n_i n_s n_p \epsilon_0 c^3} , \tag{2.15}$$

where, I_p is the instantaneous pump intensity, d_{eff} is the effective nonlinear coefficient and $n_{p,s,i}$ is the refractive index at frequency $\omega_{p,s,i}$ respectively.

While designing an OPO, it is also important to calculate the bandwidth limits of the nonlinear crystal. From eqn. 2.12 one can derive the single-pass incremental signal gain, where $\Gamma^2 > (\Delta k/2)^2$ [4, 5],

$$G_s(L) = \frac{|A_s(L)|^2}{|A_s(0)|^2} - 1 \tag{2.16}$$

$$= \Gamma^2 L^2 \frac{\sinh^2(gL)}{(gL)^2} , \tag{2.17}$$

In the limit of low gain, where $\Gamma^2 < (\Delta k/2)^2$, the gain $G_s(L)$ changes to,

$$G_s(L) = \Gamma^2 L^2 \frac{\sin^2(\overline{g}'L)}{(\overline{g}'L)^2} = \Gamma^2 L^2 \mathrm{sinc}^2(\overline{g}'L) , \tag{2.18}$$

where $\overline{g}' = ig$,

$$\overline{g}' = \left[\left(\frac{\Delta k}{2} \right)^2 - \Gamma^2 \right]^{1/2} , \tag{2.19}$$

The gain bandwidth is now defined at the first minimum of the sinc function where $G_s(L) = 0$ from eqn. 2.18. That is, when $\overline{g}'L = \pi$. If $\Gamma^2 L^2 \ll \pi^2$, then the gain function can be approximated to a $\mathrm{sinc}^2(\Delta k L/2)$ relationship for which the full width at half maximum (FWHM) signal gain bandwidth, is given by,

$$\Delta \Omega_s \simeq \left| \frac{5.56}{\delta v_{si} L} \right| , \tag{2.20}$$

where, $\delta v_{si} = 1/v_s - 1/v_i$ is the group velocity mismatch (GVM) between the signal and idler. From eqn. 2.20, it can be seen that the value of $\Delta \Omega_s$ can be improved by reducing the crystal length or reducing the GVM between signal and idler. This is

possible when signal and idler wavelengths are identical, that is, under the condition known as degeneracy.

Similarly, the pump acceptance bandwidth can be calculated. This is simply given by replacing δv_{si} in eqn. 2.20 with δv_{pi}, which is the pump-idler GVM.

So far a plane wave analysis has been assumed. The condition of tight focussing along with synchronous pumping was first analysed by Guha [6] and McCarthy [7], which was later combined and simplified by Hanna et.al [8] to arrive at the following expression for the threshold peak pump power,

$$P_{p,th} = \frac{n_p\, n_i\, \lambda_i^2\, \lambda_s\, c\, \epsilon_0}{128\,\pi^2 d_{eff}^2\, l_{eff}} \frac{\epsilon_s}{g_t\, \xi_s\, \mathrm{Re}\,(h_2)}\ , \tag{2.21}$$

where ϵ_s is the fractional power loss per round trip, and $g_t = [\tau_p^2/(\tau_p^2+\tau_s^2)]^{1/2}$ for which τ_j is the pulse duration. The confocal parameter ξ_s is defined as a ratio between the crystal length, L and the confocal length b_s, and l_{eff} is the effective interaction length defined by McCarthy [7] as a function of crystal length and the GVM between the interacting pulses.

While designing an OPO, another factor that comes into play is the intra-cavity losses. In order to measure this loss, a calculation method based on the well-known Findlay-Clay analysis [9] technique was employed. For this, the reflectivity of one of the mirrors in the OPO cavity was changed and the subsequent change in the operating threshold was noted and from this the intra-cavity losses could be approximated. For a plane wave analysis, the expression for multiplicative gain is considered which is similar to eqn. 2.17 ($G_{inc} = G_{mult} - 1$).

$$G_{mult}(L) = \frac{|A_s(L)|^2}{|A_s(0)|^2} \tag{2.22}$$

$$= \cosh^2(\Gamma L)\ , \tag{2.23}$$

Let R_M and R_L indicate the output coupler reflectivity and the effective reflectivity for all other losses in the cavity, respectively. An expression at the operating threshold then can be written as,

$$R_L R_M \cosh^2(\Gamma L) = 1\ , \tag{2.24}$$

In the limit of low loss, that is, R_M and R_L are high, eqn. 2.24 implies that $\Gamma L \ll 1$, and the equation can be approximated to,

$$\ln[\cosh^2(\Gamma L)] = -\ln R_L - \ln R_M \tag{2.25}$$

$$\Gamma^2 L^2 \simeq -\ln R_L - \ln R_M . \tag{2.26}$$

From eqn. 2.15, $\Gamma^2 \propto P_{th}$, where P_{th} is the average power at threshold, eqn. 2.26 can be rewritten as,

$$KP_{th} = -\ln R_L - \ln R_M , \tag{2.27}$$

where K is a proportionality constant. Thus, by measuring the oscillating threshold, P_{th}, for different values of output coupler reflectivities, R_M, it is possible to obtain the value R_L, the intra-cavity losses. Typical values of resonator losses in the range of 13-17% were obtained for our set-ups.

2.1.4 Parametric Transfer

An important part of the work undertaken is the pulse shape transfer from the NIR pump to the MIR idler [see chapter 7]. An analysis of how the interacting pulses affect the transfer of the pulse shape from the pump to the idler is carried out in brief in this section based on the previous work by Prawiharjo et al [10, 11]. To begin with, the Fourier transform of Maxwell's wave equation, is given by equation 2.28 [1] where $\sim$ over a symbol indicates that it is a Fourier transform.

$$\frac{\partial^2 \widetilde{E}(z,\omega)}{\partial z^2} + k(\omega)^2 \widetilde{E}(z,\omega) = -\mu_0 \omega^2 \widetilde{P}^{NL}(z,\omega) , \tag{2.28}$$

The second order nonlinear polarisation for DFG, and the electric field envelope are given by eqns. 2.29 and 2.30, respectively, where $\Omega_j = \omega - \omega_j$ is the frequency detuning from the central frequency, ω_j.

$$\widetilde{P}_i^{NL}(z,\Omega_i) = 2d\epsilon_0 \int_{-\infty}^{+\infty} \widetilde{E}_p(z,\Omega_s + \Omega_p)\widetilde{E}_s^*(z,\Omega_s)\, d\Omega_s , \tag{2.29}$$

$$\widetilde{E}_j(z,\Omega_j) = \widetilde{A}_j(z,\Omega_j)exp\left[ik(\omega_j + \Omega_j)\right]z . \tag{2.30}$$

The idler frequency-domain spatial envelope, $\widetilde{A}_i(L,\Omega_i)$, can be derived by using the above mentioned equations 2.28 to 2.30 and the slowly-varying envelope approximation.

Assuming plane wave interactions in the entire length, L, of an isotropic medium, with no pump depletion ($dE_p/dz = 0$), no signal amplification and z as the direction of propagation, we get,

$$\widetilde{A}_i(L, \Omega_i) = \int_{-\infty}^{+\infty} \int_0^L i\alpha_i \widetilde{A}_p(\Omega_s + \Omega_i)\widetilde{A}_s^*(\Omega_s)\exp[i\Delta k_{DFG}(\Omega_s, \Omega_i)z]\, dz\, d\Omega_s$$

$$= \int_{-\infty}^{+\infty} i\alpha_i \widetilde{A}_p(\Omega_s + \Omega_i)\widetilde{A}_s^*(\Omega_s)L\operatorname{sinc}\left[\Delta k_{DFG}(\Omega_s, \Omega_i)\frac{L}{2}\right]$$

$$\times \exp\left[i\Delta k_{DFG}(\Omega_s, \Omega_i)\frac{L}{2}\right] d\Omega_s\,, \qquad (2.31)$$

where, subscripts p, s and i indicate pump, signal and idler respectively. For further simplification, if the interaction length of the crystal is small enough such that the group velocity mismatch (GVM) between the interacting pulses can be neglected, eqn. 2.31 reduces to a simple convolution,

$$\widetilde{A}_i(L, \Omega_i) \propto \widetilde{A}_p(\Omega_p) \otimes \widetilde{A}_s^*(\Omega_p - \Omega_i)\,. \qquad (2.32)$$

Here, $A_{p,s,i}$ depicts the slowly varying complex envelope as defined by eqn. 2.11. It is important to note here that this equation is derived for the simplest case assuming dispersionless material, undepleted pump and unamplified signal under perfectly phase matched conditions.

Moreover, eqn. 2.32 suggests that a complete transfer of the pump pulse envelope characteristics to the idler pulse envelope can occur when the signal is a delta function, that is, $\widetilde{A}_s^*(\Omega_p - \Omega_i)$ is a delta function. Therefore, high fidelity transfer of the pump requires a very narrow signal spectrum. This along with other factors are discussed in detail in chapter 7.

2.2 Pulse Manipulation

The pulse, after generation, is then manipulated to have the desired spectral phase and amplitude profile. The two most common pulse-shaping techniques are based on spatial light modulators (SLM) and acousto-optic modulators. The principle behind pulse shaping using SLMs is detailed in the following section, as this is the method employed in the experiments reported here. For this we use a 4-f configuration shaper with a SLM at its Fourier plane. This SLM is controlled by an adaptive optimisation algorithm.

2.2.1 Principle

The mathematical description of the pulse shaping method is outlined here. The process is based on the linear, time-invariant filtering [12] and employs Fourier transform techniques. In time domain, an impulse response function often referred to as a Green function, $H(t)$ defines a linear filter. The output waveform $E_{out}(t)$ is given by the convolution of the input pulse $E_{in}(t)$ and $H(t)$:

$$E_{out}(t) = E_{in}(t) \otimes H(t) \,. \tag{2.33}$$

In the frequency domain, the linear filter is defined by $\widetilde{H}(\omega)$ and the output $\widetilde{E}_{out}(\omega)$, is given by the product of the input signal $\widetilde{E}_{in}(\omega)$, and $\widetilde{H}(\omega)$.

$$\widetilde{E}_{out}(\omega) = \widetilde{E}_{in}(\omega)\widetilde{H}(\omega) \,, \tag{2.34}$$

In eqn. 2.34, $\widetilde{E}_{out}(\omega)$, $\widetilde{E}_{in}(\omega)$ and $\widetilde{H}(\omega)$ are Fourier transforms of $E_{out}(t)$, $E_{in}(t)$, and $H(t)$, respectively.

2.2.2 Pulse shaper set-up

The pulse shaper used in the set-up consists of two diffraction gratings, two lenses and one mask, each separated by the focal length distance f, making it a 4-f configuration or a zero dispersion pulse compressor. This ensures that when no mask is present, the output pulse from the shaper remains unchanged. The first diffraction grating spreads out the input pulse such that the different frequencies are mapped at different angles. The lens then focusses each frequency component onto the Fourier plane. The mask placed at this focal plane can shape the input pulse by altering the amplitude, phase or both the parameters of each individual spectral component. The second lens and diffraction grating then recombine the frequency components into one single collimated beam.

For ultrashort pulses, a LC-SLM is the most widely used instrument for pulse shaping. We use the 4-f pulse shaper configuration LC-SLM, as shown in fig. 2.4 for modifying the pump spectral phase profile. This method was introduced by Froehly [13] and later improved upon by Weiner [14]. Using the LC-SLM in this set-up enables programmable control over the pulse profiles.
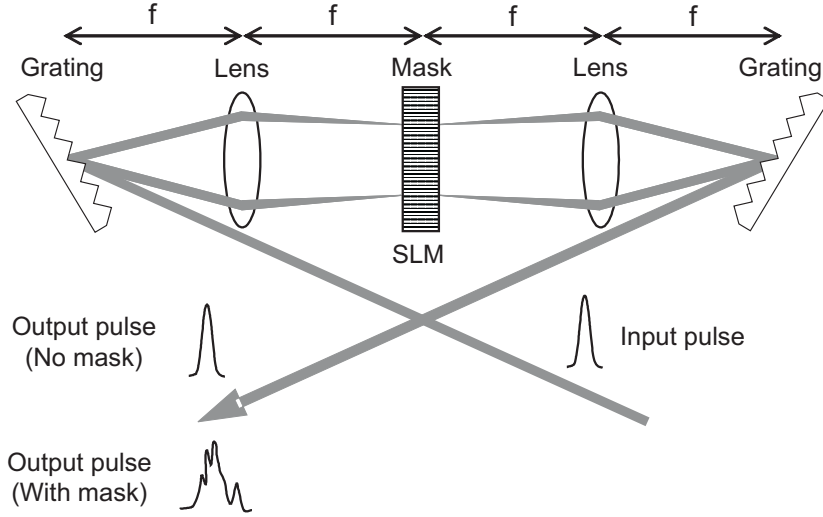
FIGURE 2.4: Pulse shaper in the 4-f configuration.

The design parameters for a pulse shaper set-up need to be chosen such that sufficient spatial dispersion and resolution can be achieved with the given set of optics. At the input of the pulse shaper, the beam is dispersed by the first grating in the set-up. With λ, m and d as the central wavelength, grating order and grating period respectively, and θ_{in} as the input and θ_d as the diffracted angles of the grating, we have

$$\sin\theta_d = \frac{m\lambda}{d} - \sin\theta_{in} \,, \tag{2.35}$$

By differentiating eqn. 2.35, the angular dispersion D of a grating is obtained as:

$$D = \frac{d\theta_d}{d\lambda} = \frac{m}{d\cos\theta_d} \,. \tag{2.36}$$

The size of the beam at the Fourier plane for a pulse with bandwidth $\Delta\lambda$ can then be calculated using eqn. 2.36 and the dispersion angle, $\Delta\theta_d$ is given by:

$$\Delta\theta_d = D\,\Delta\lambda \,. \tag{2.37}$$

For small values of $\Delta\theta_d$, and the diffraction order, m, set to 1, the spatial extent of the beam at the Fourier plane, y, can be approximated to,

$$y \;=\; f\Delta\theta_d$$

$$=\; \frac{f\Delta\lambda}{d\cos\theta_d} \,. \tag{2.38}$$

Here f is the focal length. We can then derive the spatial dispersion, α, from eqn. 2.38

$$\alpha = \frac{y}{\Delta\omega} = \frac{f\lambda^2}{2\pi cd\cos\theta_d} ,\qquad(2.39)$$

where $\Delta\omega$ is the pulse bandwidth in units of rad/s and c is the speed of light. Therefore, for a given wavelength and fixed grating period, d, variation of the spatial dispersion depends on the focal length and grating angle. The pulse shaper apparatus must be designed to ensure sufficient grating efficiency and large enough angles between the incident and diffracted beams to account for the physical limitations imposed by the dimensions of the lens and the mask.

Weiner [12] shows that to obtain a quantitative description of the output waveform $\widetilde{E}_{out}(\omega)$, it is important to relate the linear filtering function $\widetilde{H}(\omega)$ to the actual masking function, $\widetilde{M}(x)$. This function describes the spatial distribution of the amplitude and phase transmission of the mask. The electric field, with a Gaussian spatial distribution, immediately after the mask, $\widetilde{E}_m(x,\omega)$ is given by,

$$\widetilde{E}_m(x,\omega) \sim \widetilde{E}_{in}(\omega)exp\left[-\frac{(x-\alpha\omega)^2}{\mathrm{w}_0^2}\right]\widetilde{M}(x) ,\qquad(2.40)$$

where w_0 is the $1/\mathrm{e}^2$-intensity half-width of each individual frequency component at the Fourier plane. This radius of the beam focussed at the masking plane for a single spectral component is given by equation 2.41 and is matched to the pixel-size in the LC-SLM.

$$\mathrm{w}_0 = \frac{cos\,\theta_{in}}{cos\,\theta_d}\left(\frac{f\lambda}{\pi\mathrm{w}_{in}}\right) ,\qquad(2.41)$$

where w_{in} is the input beam radius before the first grating, f is the focal length of the lens, λ is the wavelength, θ_{in} and θ_d are the input and diffracted angles from the first grating respectively. Equation 2.40 describes the field as an inseparable function of both space (x) and frequency (ω). Due to the finite size of each individual frequency at the mask, it is possible for different spatial parts of the single frequency component to see different optical retardation and/or transmittance. This could lead to spatial diffraction where the single frequency components are incident over inter-pixel gaps or pixel edges, and result in an output field which may be a coupled function of space and time. Full analysis of the space-time coupling has been studied by Wefers and Nelson [15] who find that the effect of the mask is to introduce a time-dependent spatial shift. This shift, Δx is given by,

$$\frac{\Delta x}{\Delta t} = -\frac{cd\cos\theta_{in}}{\lambda} .\qquad(2.42)$$

In order to obtain an output field which is spatially uniform with a single temporal profile, that is, a field which is a function of frequency(or time) alone, an appropriate spatial filtering operation is required. For negligible pulse front tilts, eqn. 2.40 can be simplified to neglect the space-time coupling by rewriting the equation as a superposition of Hermite-Gaussian modes for which the fundamental Gaussian mode is not space-time coupled [16] and assuming that all of the spatial modes except for the fundamental Gaussian mode are eliminated by the spatial filtering. In practice, these modes can be eliminated for example, by focussing the beam into a fibre. The shaped field is then described by the lowest order Hermite-Gaussian mode and the filter function, $\widetilde{H}(\omega)$, is defined by its coefficient and the following expression is obtained [12, 17],

$$\widetilde{H}(\omega) = \left(\frac{2}{\pi w_0^2}\right)^{1/2} \int_{-\infty}^{\infty} \widetilde{M}(x) \exp\left[-\frac{2(x - \alpha\omega)^2}{w_0^2}\right] dx \,. \tag{2.43}$$

This equation shows that the filter function is simply the masking function, $\widetilde{M}(x)$ convolved with a Gaussian beam profile which has an effective $1/e$ spot size of $w_0/\sqrt{2}$. The convolution results in limiting the FWHM spectral resolution, $\delta\omega$, of the pulse shaper to,

$$\delta\omega = (\ln 2)^{1/2} \frac{w_0}{\alpha} \,. \tag{2.44}$$

Using eqns. 2.39, 2.41 and 2.44, one can determine the complexity, η, of the pulse shaper. It is important in the design parameters to achieve the maximum possible complexity to be at least as complex as the mask in terms of the number of pixels. The complexity is defined by,

$$\eta = \frac{\Delta\omega}{\delta\omega} = \frac{\Delta\lambda}{\lambda} \frac{\pi}{\sqrt{\ln 2}} \frac{w_i}{d\cos\theta_{in}} \,. \tag{2.45}$$

As can be seen from eqn. 2.45, the complexity can be most conveniently improved by increasing the input spot size on the grating.

Referring back to eqn. 2.43, writing the convolution relation in terms of the inverse Fourier Transform, the impulse response, $H(t)$, is given by the product,

$$H(t) = M(t)G(t) \,, \tag{2.46}$$

where $M(t)$ is the inverse Fourier transform of $\widetilde{M}(\alpha\omega)$ and $G(t)$ is given by,

$$G(t) = \exp\left(-\frac{w_0^2 t^2}{8\alpha^2}\right) \,, \tag{2.47}$$

Equation 2.47 describes a Gaussian envelope [12], FWHM of which is given by,

$$T = \frac{4\alpha\sqrt{\ln 2}}{w_0} = \frac{2\sqrt{\ln 2}\, w_i n\lambda}{cd\cos\alpha} \,, \tag{2.48}$$

The maximum temporal window T is the time window in which the tailored output pulse can accurately reflect the response of the infinite resolution mask [12]. This is related to the resolution in eqn. 2.44 by the Fourier limit. Mathematically, $T\delta f \cong 0.44$, where $\delta\omega = 2\pi\delta f$. δf is also defined as the finest achievable spectral feature.

On the other hand, the shortest temporal feature that can be produced, δt, is related to the total bandwidth B, $B\delta t \cong 0.44$. The complexity, η, which describes the number of distinct spectral features that may be placed into the available bandwidth B, can be expressed as,

$$\eta = \frac{\Delta\omega}{\delta\omega} = \frac{B}{\delta f} = \frac{T}{\delta t} \, . \tag{2.49}$$

2.2.3 Spatial Light Modulators

In experiments where adaptive control is required, the shaping mask needs to be variable. There are various programmable SLMs available in the market using liquid crystals, AOM or deformable mirrors. Deformable mirrors are efficient SLMs, but can only render phase modulation. AOMs, even though they permit phase and amplitude modulation, are restricted to low repetition rates. LC-SLMs, on the other hand allow for phase and amplitude modulation at high repetition rates. As LC-SLM were used for adaptive control in the work presented in this thesis, they are discussed in detail in the following paragraphs.

Liquid crystal spatial light modulators

The SLM optics use liquid crystal material to manipulate the phase and/or amplitude of the individual frequency components of the spatially dispersed input beam. The basic principle is that the liquid crystal (LC) material provides an electrically variable refractive index for the light polarised along its extraordinary axis. Commercially available LCM arrays are configured for use as a phase only or phase and amplitude modulators. There are various configurations possible and only those that were employed in the experiments performed are outlined here.

For phase only operation, the incident light must be polarised parallel to the extraordinary axis (i.e. parallel to the axis of the molecules) of the LC array as depicted in fig. 2.5.

As indicated in fig. 2.5, the procedure for single layer, phase only modulation using LC-SLM is listed as follows:
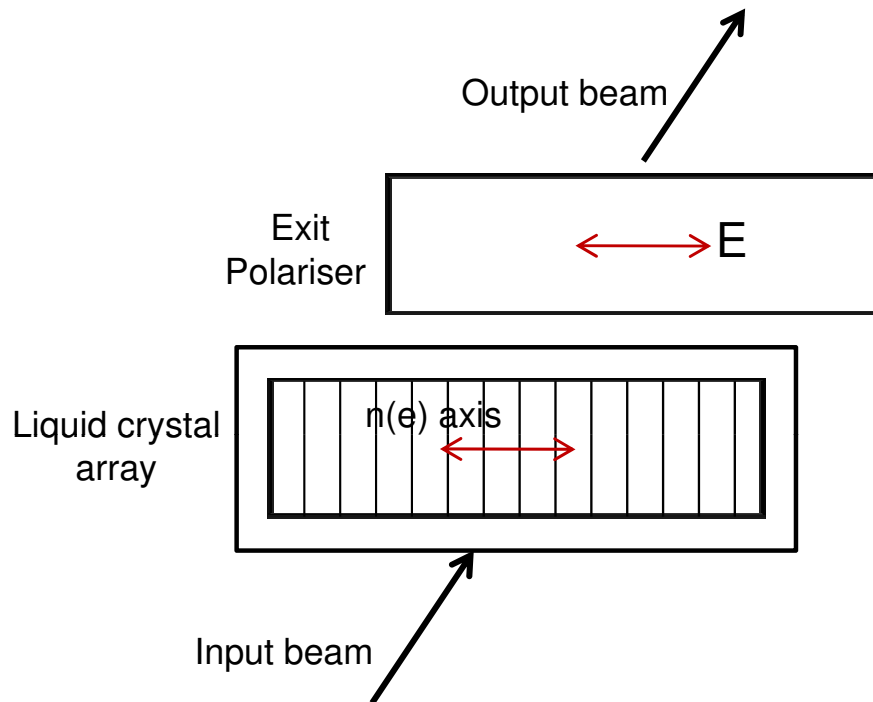
FIGURE 2.5: Phase-only modulation using single layer LC-SLM in transmissive mode.

1. Input beam is horizontally polarised.

2. Index n at each pixel is varied to modulate the phase of the incident beam.

3. Exit polariser removes any residual vertically polarised light to ensure that the device works as a pure phase only modulator.

4. Output beam is phase modulated.

In amplitude modulation, the intensity at each pixel is modulated by introducing horizontally polarised light into a LC cell whose crystal axis is at 45°. This LC array then acts as an electrically variable waveplate, to modify the polarisation state of light. The procedure for single layer, amplitude only modulation using LC-SLM is listed as follows:

1. Input beam is horizontally polarised.

2. Retardance varies polarisation state according to the applied voltage.

3. Exit polariser selects only horizontal polarisation.

4. Output beam is amplitude modulated.

In dual mode, or phase and amplitude modulation models, a pair of LC elements are bonded together. The orientation of the LC arrays is orthogonal to one another and

45° to the input polarised light. To the extent that the two arrays vary together, phase is modulated and the extent to which they differ (generating a differential signal), the polarisation is modified which in turn can be used to modulate the amplitude. As the phase and amplitude pulse shaping apparatus was set-up in reflective mode during the experiments, the procedure for that mode is listed here and described by the help of fig. 2.6.
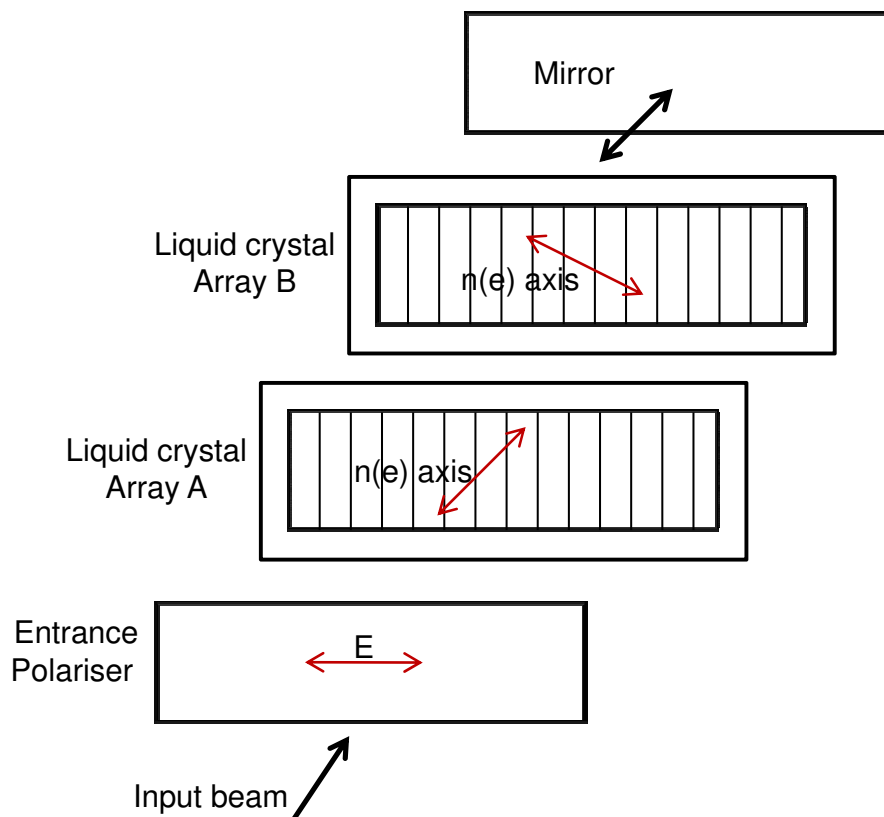
FIGURE 2.6: Phase and amplitude modulation using dual layer LC-SLM in reflective mode.

1. Input beam is horizontally polarised at entrance polariser.

2. Differential retardance (A-B) alters the polarisation state.

3. Average retardance (A+B)/2 modulates the phase.

4. Mirror reflects the beam back towards LC cells.

5. Retardance is doubled during the second pass through the cells.

6. Entrance polariser acts as the output polariser and selects horizontally polarised component.

This set-up can easily be used as a phase only modulator when arbitrarily polarised light is incident on the pair of arrays and both liquid crystal elements are driven by an identical voltage pattern and the input polariser is removed.

2.3   Summary

This chapter was a brief introduction to the principles behind pulse generation and manipulation. In the first half of the chapter, the processes of difference frequency generation and quasi phase matching were introduced. In addition, the principles behind parametric gain and bandwidth and parametric transfer, which are at the heart of an OPO operation, were discussed. In the second half of the chapter, the principle and set-up of a pulse shaper were outlined along with a brief insight into how the LC-SLM acts as a phase or phase and amplitude shaper.

Once the pulses are generated and manipulated, another important part of the experimental process is to characterise them. This leads on to the next chapter where the different pulse characterisation techniques along with some experimental results are discussed in more depth.

References

[1] G. P. Agrawal, *Nonlinear Fibre Optics*, Academic Press, third ed., 2001.

[2] R. W. Boyd, *Nonlinear Optics*, Academic Press, 2nd ed., 2000.

[3] J. C. Diels and W. Rudolph, *Ultrashort laser pulse phenomena*, Academic Press, 2nd ed.

[4] R. L. Byer, "Parametric oscillators and nonlinear materials," in *Nonlinear Optics*, P. G. Harper and B. S. Wherrett, eds., Academic Press, New York, 1977.

[5] M. A. Watson, *Agile tuning and long-wavelength tuning of synchronously pumped optical parametric oscillators*. PhD thesis, University of Southampton, 2003.

[6] S. Guha, "Focusing dependence of the efficiency of a singly resonant optical parametric oscillator," *Appl. Phys. B* **66**, pp. 663–675, 1998.

[7] M. J. McCarthy and D. C. Hanna, "All-solid-state synchronously pumped optical parametric oscillator," *J. Opt. Soc. Am. B* **10**, p. 2180, 1993.

[8] D. C. Hanna, M. V. O'Connor, M. A. Watson, and D. P. Shepherd, "Synchronously pumped optical parametric oscillator with diffraction-grating tuning," *J. Phys. D* **34**, pp. 2440–2454, 2001.

[9] S. D. Butterworth, S. Girard, and D. C. Hanna, "High-power, broadly tunable all-solid-state synchronously pumped lithium triborate optical parametric oscillator," *Journal of the Optical Society of America B-Optical Physics* **12**(11), pp. 2158–2167, 1995.

[10] J. Prawiharjo, *Frequency-resolved optical gating in periodically-poled lithium niobate waveguide devices*. PhD thesis, University of Southampton, 2005.

[11] J. Prawiharjo, H. S. S. Hung, D. C. Hanna, and D. P. Shepherd, "Theoretical and numerical investigations of parametric transfer via difference-frequency generation for indirect mid-infrared pulse shaping," *Journal of the Optical Society of America B-Optical Physics* **24**(4), pp. 895–905, 2007.

[12] A. M. Weiner, "Femtosecond pulse shaping using spatial light modulators," *Review of Scientific Instruments* **71**(5), pp. 1929–1960, 2000.

[13] C. Froehly, B. Colombeau, and M. Vampouille, "Shaping and analysis of picosecond light-pulses," *Progress in Optics* **20**, pp. 65–153, 1983.

[14] A. M. Weiner, "Femtosecond optical pulse shaping and processing," *Progress in Quantum Electronics* **19**(3), pp. 161–237, 1995.

[15] M. M. Wefers and K. A. Nelson, "Programmable phase and amplitude femtosecond pulse shaping," *Opt. Lett.* **18**(23), pp. 2032–2034, 1993.

[16] P. Malara, P. Maddaloni, G. Mincuzzi, S. De Nicola, and P. De Natale, "Non-collinear quasi phase matching and annularprofiles in difference frequency generation withfocused gaussian beams," *Opt. Express* **16**(11), pp. 8056–8066, 2008.

[17] R. N. Thurston, J. P. Heritage, A. M. Weiner, and W. J. Tomlinson, "Analysis of picosecond pulse shape synthesis by spectral masking in a grating pulse compressor," *IEEE J. Quantum Electron.* **22**, pp. 682–696, 1986.

Chapter 3

Ultrashort pulse characterisation techniques

3.1 Introduction

As discussed in the previous chapters, with the development of ultrashort pulse laser systems, pulse shaping has become an important experimental tool with widespread applications including coherent control of molecules. Adaptive coherent control has also been used in biomedical imaging applications, for multiphoton microscopy techniques [1–3] and coherent anti-Stokes Raman scattering (CARS) microscopy [4, 5], to name a few. In such experiments, additional details of the pulse's structure plays a crucial role in determining the outcome of the experiment. On the other hand, characterising the output pulse can help us understand the molecular chemistry better. To add to this, as the fibre laser pump source used in the experiments was home built, it was important to characterise the pulses emitted from the laser to verify the performance of the system. Precise knowledge of the pulse characteristics is also required to understand the limitations of the system as well as to possibly improve the output. The pump for the laser system was in the near-infrared wavelength regime whereas the idler output from the optical parametric oscillator was in the mid-infrared regime, thus, making pulse characterisation techniques in both these regimes relevant.

For a reasonable characterisation of a pulse, it is sufficient to measure its intensity and phase in either the time or the frequency domain. For longer pulses with nanosecond (ns)

or several ps durations, the temporal intensity can be measured by using a photodiode and the spectrum can be measured using readily available spectrometers. But different methods are required for pulses in the fs or shorter range, mainly because the available photo-detectors do not have a fast enough response time. This necessitates the use of something with a response time as brief as the pulse, and thus the pulse is commonly used to measure itself.

With the need for better pulse diagnostic techniques arising in the mid-1960's with the development of the mode-locked laser, much work has been undertaken by researchers on the subject. These results have been well summarised in the form of comprehensive reviews and book chapters [6–11]. For sake of brevity, only those techniques that have been employed for the work presented in this thesis are discussed in the following sections of this chapter.

The chapter starts with a brief description of the simpler pulse characterisation techniques of intensity autocorrelation (Sec. 3.2.1), the interferometric autocorrelation (Sec. 3.2.2) and the cross-correlation sonogram (CCS) (Sec. 3.2.3). The frequency-resolved optical gating (FROG) technique is detailed in section 3.2.4 followed by an experimental comparison of CCS and cross-correlation FROG (XFROG) as techniques of special interest for MIR pulse characterisation (Sec. 3.3).

3.2 Ultrashort pulse measurement
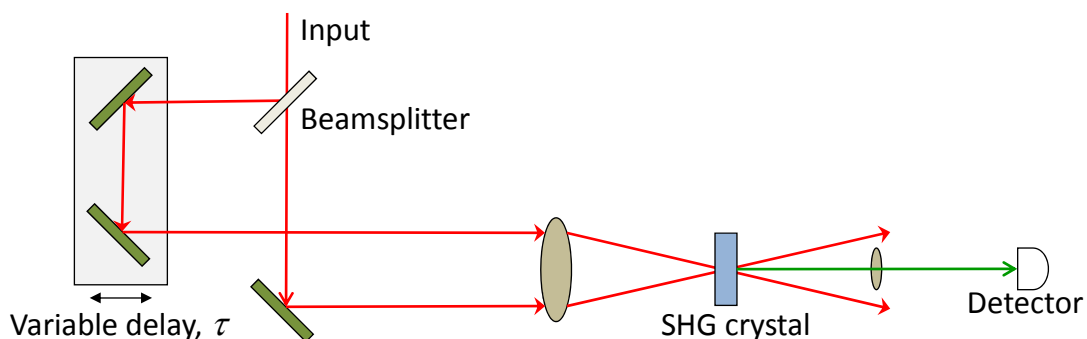
3.2.1 Intensity Autocorrelation

FIGURE 3.1: Experimental arrangement for measurement of intensity autocorrelation.

One of the early methods of ultrashort pulse characterisation was the measurement of the intensity autocorrelation (AC) of the pulse [12]. This technique is based on a Michelson interferometer arrangement with nonlinear detection. Here, the pulse can be characterised with its own self at different delays. In such an arrangement, the short length of the pulse is no longer a problem and conventional slow detectors can be used. In a standard autocorrelator, the pulse to be measured is split into two pulses and one of them has a controlled delay with respect to the other. These pulses are later spatially overlapped in a nonlinear material such as a SHG crystal (Fig. 3.1). The average power of the generated second-harmonic (SH) beam is recorded as a function of the relative delay, τ, between the two pulses. The generated SH beam has an intensity that is proportional to the product of the intensities of the input pulses. The SHG signal field is given by,

$$E_{\mathrm{SHG}}(t,\tau) \propto E(t)E(t-\tau), \tag{3.1}$$

where, $E(t)$ is the signal field at a given time t and $E(t-\tau)$ is the field at a delayed time of $t-\tau$. Correspondingly, the SHG intensity is given by,

$$I_{\mathrm{SHG}}(t,\tau) \propto I(t)I(t-\tau), \tag{3.2}$$

where E_{SHG} is the SHG electric field and I_{SHG} is the SHG intensity.

As the detectors are too slow to time resolve I_{SHG}, this measurement results in a full intensity autocorrelation profile, $I_{AC}(\tau)$, represented by equation 3.3,

$$I_{AC}(\tau) = \int_{-\infty}^{\infty} I(t)I(t-\tau)dt. \tag{3.3}$$

Equation 3.3 is an overlap integral and shows that the SHG signal generated in this way is greater when the two pulses arrive at the same time (τ=0), as opposed to when they arrive separately. Because of its simplicity, autocorrelation is by far the most common method of measuring ultrashort optical pulses. However, the autocorrelation trace by itself only provides an estimate of the pulse duration. Also, the resulting autocorrelation

is always symmetric resulting in an ambiguity in the direction of time in this technique. As a result, the AC provides only little information on the pulse shape and many different pulse shapes can have similar autocorrelation traces. Thus it is almost impossible to determine the original pulse shape in terms of its intensity and phase from its AC without any prior knowledge.

Relying on a stable continuous train of pulses, the intensity AC technique is a quick and easy method of measuring widths of simple pulses. However, the resolution of the AC is ultimately limited by the pulse itself, so any detail in the pulse intensity is washed out. Moreover, the AC technique is unable to detect the presence of chirp without independent measurement of the pulse spectrum to infer the time-bandwidth product (TBP). The AC technique is most commonly used to estimate the duration of an ultrashort pulse by assuming a pulse shape, say Gaussian or sech^2, and using the known ratio between the FWHM of the autocorrelation and the pulse to approximate its pulse duration.

3.2.2 Interferometric Autocorrelation

Fringe resolved autocorrelation (FRAC) or interferometric autocorrelation is a technique, developed by Diels et al. [13], that combines quantities related to the autocorrelation and the spectrum. The experimental configuration uses a Michelson interferometer arrangement with a nonlinear medium, such as the SHG crystal, at the output. This is similar to the AC described above, except for that the input beams are collinear in this arrangement. The SH beam thus generated by the interaction of the two beams combines coherently with the SH created by each of the beams individually. As a result, interference fringes are created. For intensity autocorrelations, these fringes are usually averaged out with a slow detector or completely avoided with a non-collinear arrangement (as in fig. 3.1). The FRAC technique can be used to determine the presence of chirp by simple interpretation of the FRAC profile, unlike the intensity AC. The experimental set-up of the FRAC that was used for the work presented in this thesis is shown in figure 3.2. The nonlinear optical process used here is TPA and occurs within the photodiode detector, although a SHG crystal, as with the previous AC setup, can
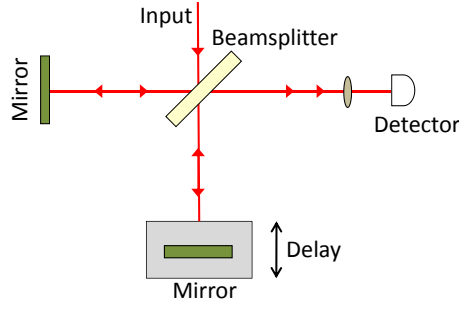
FIGURE 3.2: Experimental layout for the fringe-resolved autocorrelation.

be used. The detectors used in TPA autocorrelators can be the standard commercially available devices [14–16] and are therefore a cheap alternative to SHG crystals especially for measuring broadband sources where the crystal would have to be very thin to accommodate the bandwidth. It is also relatively easy to cover various wavelength regimes, including MIR, with this set-up.

A fringe-resolved autocorrelator set-up, similar to the collinear arrangement depicted in Fig. 3.2 was employed to obtain some of the experimental results discussed in this thesis. The only difference being that the variable delay arm has a corner cube reflector mounted to a loudspeaker. A loudspeaker was used as it was readily available and provided convenient measurement suitable for continuous monitoring of sub-ps pulses. A silicon wafer was used as a Fresnel reflection 75:25 beam splitter and the output was focussed with a 12.7 mm CaF_2 lens on to an extended InGaAs detector. This set-up is generally suitable for MIR sources discussed in chapter 7, but can also be used in NIR by suitably replacing the detector and the beamsplitter.

The interference of the two beams in the set-up is recorded as a function of the variable delay, τ [13]. The expression for the FRAC trace is given by equation 3.4.

$$
\begin{aligned}
I_{\text{FRAC}}(\tau) \;=\; & \int_{-\infty}^{\infty} \left\{ I(t)^2 + I(t-\tau)^2 \right\} dt \\
& + \int_{-\infty}^{\infty} \left\{ I(t) + I(t-\tau) \right\} Re\left\{ E(t)E^*(t-\tau) \right\} dt \\
& + \int_{-\infty}^{\infty} Re\left\{ E(t)^2 E^*(t-\tau)^2 \right\} dt \\
& + \int_{-\infty}^{\infty} I(t)I(t-\tau)dt.
\end{aligned}
\tag{3.4}
$$

The eqn. 3.4 contains the first term which is a background measurement and therefore a constant. This term can be a guide to the validity of the measurement as the peak-to-background ratio in a FRAC trace should be 8:1. The second term is the modified interferogram of E(t) (except for the $I(t) + I(t - \tau)$ term). The third term is the interferogram of the two-photon signal of E(t) resulting in the fringes. Finally, the last term is just the intensity autocorrelation as defined in eqn. 3.1.

If a slow detector is used in this set-up an intensity AC can be obtained, as the time averaged result of eqn. 3.4 reduces to just the first and last term. As mentioned earlier, for all FRACs, the contrast ratio of the peak-to-background level is 8:1 and the contrast ratio for intensity ACs is 3:1. These are indicated in figures 3.3(a) and 3.4 for a theoretical bandwidth-limited femtosecond pulse. As can be seen from fig. 3.3(b), for a theoretical chirped pulse, we can get an indication of whether the pulses are bandwidth limited from the degree to which the fringes fill out the FRAC trace, but it still fails to give absolute pulse shapes.

3.2.3 Sonogram

The inability of the techniques discussed so far to give a complete map of the pulse, led to the concept of using not just the individual time or frequency domain but a hybrid time-frequency domain. Among the most successful of these techniques was the spectrogram or the sonogram, consisting of a time-frequency map that plotted the instantaneous frequency of the pulse. The spectrogram measures the spectrum of sequential time slices of the test pulse while the sonogram, does just the reverse and measures the time dependence of adjacent spectral slices. The very first measurement of a sonogram was reported by Treacy [17] for a ps pulse but it took more than a decade for the potential of the technique for complete characterisation of a fs pulse to be realised [18].

Spectrograms and sonograms are now widely used in ultrafast optics. The most common approach to this measurement is to perform a sequential gating in the time and frequency domains by using a time non-stationary (or equivalently frequency stationary) and a time stationary filter. Time stationary filters are those whose outputs do not depend on the arrival time of the pulse, e.g. mirrors, gratings, etc. On the contrary, time non-stationary

(a) For bandwidth-limited unchirped pulse
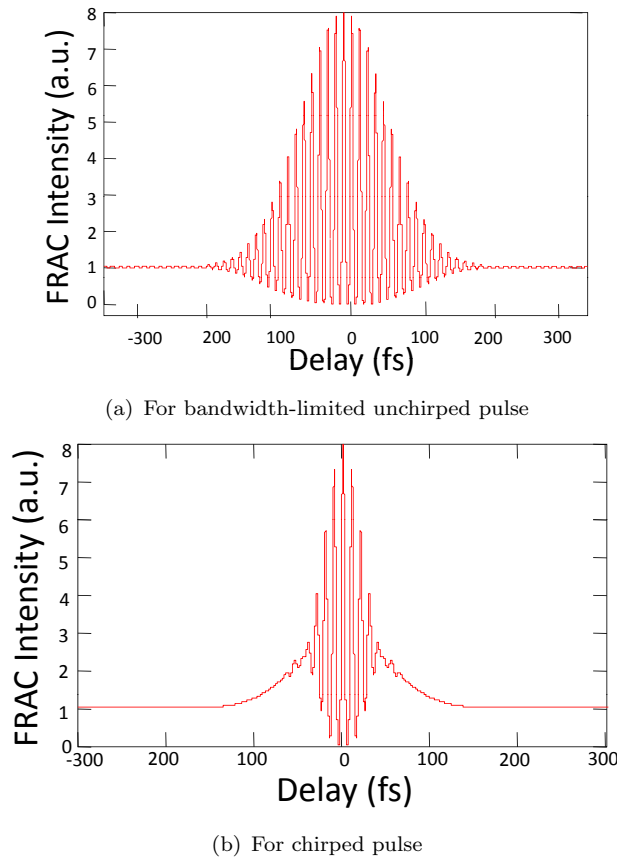

(b) For chirped pulse

FIGURE 3.3: Theoretical intensity autocorrelation for an 87 femtosecond bandwidth-limited pulse showing the contrast ratio for (a) fringe-resolved AC; and (b) chirped 87 femtosecond pulse which has fewer fringes and thus revealing the intensity AC component at its wings where there are no fringes. The chirp parameter was set at $a = 8$ with the ratio of maximum of lower envelope to maximum upper envelope equal to 2.5:8

filters are those that produce outputs which do not change with spectral shifts in the input, eg. shutters. The time non-stationary filter can be delayed in time by a quantity τ with respect to the test pulse, and the transfer function of the frequency non-stationary (time stationary) filter can be tuned along the optical frequency axis by an amount Ω. The final measured quantity is therefore a function of these two variables, which have to be varied to cover completely the phase-space occupied by the pulse. Furthermore, if the two filters are in sequence, and the second has a very high resolution (i.e., is either a fast shutter or a narrow band spectral filter), this approach can be considered to make a simultaneous measurement of the time and frequency of the pulse [10].

Fig. 3.5 illustrates the principle behind the two measurements discussed here: the spectrogram (3.5(a))and the sonogram (3.5(b)) for a better understanding. The spectrogram is measured by first gating the pulse with a time non-stationary filter and measuring
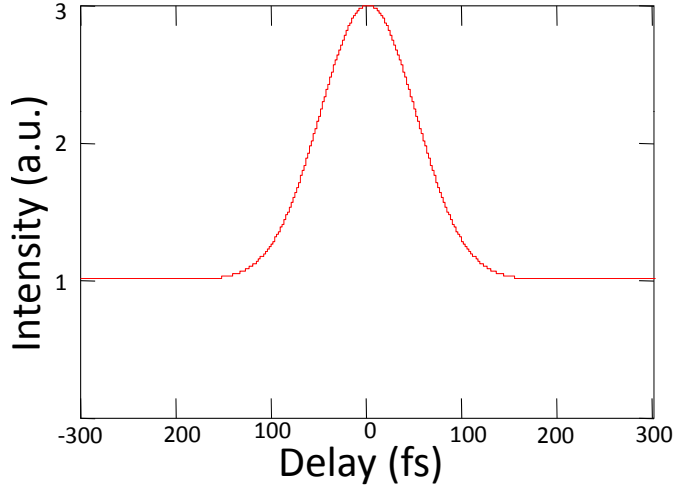
FIGURE 3.4: Theoretical intensity autocorrelation for an 87 femtosecond bandwidth-limited pulse showing the contrast ratio for the AC. The AC remains the same even for a chirped pulse.

the optical spectrum as a function of the optical frequency and relative delay between the pulse and the gate. Conversely, the sonogram is measured by first filtering the pulse with a time-stationary filter and measuring the temporal intensity as a function of time and the position of the spectral filter.

(a) Spectrogram
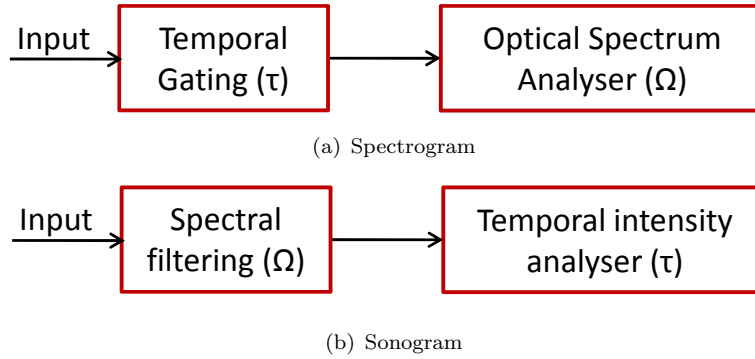
(b) Sonogram

FIGURE 3.5: Principle behind the measurement techniques of the (a)Spectrogram and the (b) Sonogram.

The sonogram technique [19] is a method of pulse characterisation that relies on frequency gating rather than temporal gating which is used in FROG techniques described in detail in the next section. The sonogram records a two-dimensional trace of the form given by eqn. 3.5 [20],

$$I_{sono}(t, \Omega) = \left| \int_{-\infty}^{\infty} \widetilde{E}(\omega)\widetilde{G}(\omega - \Omega)\exp(-i\omega t)d\omega \right|^2, \tag{3.5}$$

where $\widetilde{E}(\omega)$ describes the original pulse, $\widetilde{G}(\omega - \Omega)$ describes the frequency filter, and Ω is the frequency detuning.

The experimental set-up of the sonogram used for measurements is shown later in fig. 3.8 and the set-up is described in detail in sec. 3.3. In principle, this configuration involves frequency gating using a diffraction grating and a movable mask (slit) in a folded 4-f pulse shaper arrangement (see chapters 4 and 5) such that, for each frequency, a cross-correlation is measured and compiled to retrieve information. The resulting sonogram traces are highly intuitive and have no ambiguity in the direction of time so that one can distinguish between positive and negative chirp. Moreover, the sonogram setup can be easily modified for use in different wavelength regions as it only requires the detector to be changed accordingly. In this cross-correlation sonogram (CCS) arrangement, eqn. 3.5 describes only the spectral filtering part of the measurement process. Due to the self-referencing nature of this method, the CCS measures a modified sonogram that can be accurately described by an intensity cross-correlation between the filtered replica and the original pulse intensity [20, 21],

$$I_{\mathrm{x}sono}(t, \Omega) = I(t) \otimes I_{sono}(t, \Omega), \qquad (3.6)$$

where I(t) is the intensity profile of the input pulse and $\otimes$ is the convolution operator. $I(t)$ can be approximated to a delta function such that $I_{\mathrm{x}sono}(t, \Omega) \simeq I_{sono}(t, \Omega)$ for narrow slit widths where the filtered pulse width is temporally much longer than the original pulse. Pulses that are highly chirped cannot satisfy this approximation, in which case retrieval of the pulse requires an initial deconvolution step.

The CCS algorithm developed by Reid [19, 20] is based on the principal component generalised projections (PCGP) method used for FROG [22] described later in sec. 3.2.4. Reconstruction of the sonogram from the two guess pulse vectors uses the same procedure as the FROG but it is in the frequency domain rather than the time domain. Retrieval of the CCS trace has an added step to deconvolve it with the intensity profile from the most recent guess to reveal the true sonogram. The intensity of the true sonogram would then replace the intensity of the current guess of the sonogram before applying the PCGP step to the pseudo-outer product matrix.

3.2.4 Frequency Resolved Optical Gating

In the beginning of the previous section, the spectrogram as a time-frequency domain measurement technique was introduced. The mathematical expression for the spectrogram, $\Sigma_g^E(\omega, \tau)$ is given by eqn. 3.7 [11],

$$\Sigma_g^E(\omega, \tau) = \left| \int_{-\infty}^{\infty} E(t) g(t - \tau) \exp(-i\omega t) dt \right|^2 , \qquad (3.7)$$

where $g(t - \tau)$ is the variable-delay gate function, τ is the time delay and $E(t)$ is the time domain electric field of the pulse. A well-known device for measuring spectrograms is the FROG [23, 24] for which the gate function is related to $E(t)$ so that the method is self-referencing, like the autocorrelator. Eqn. 3.7 can be modified to eqn. 3.8 to give a more general form for the measured FROG trace, $I_{FROG}(\omega, \tau)$.

$$I_{FROG}(\omega, \tau) = \left| \int_{-\infty}^{\infty} E_{sig}(t, \tau) \exp(-i\omega t) dt \right|^2 , \qquad (3.8)$$

Here $E_{sig}(t, \tau)$ is given by eqn. 3.9,

$$E_{sig}(t, \tau) = E(t) \, g(t - \tau). \qquad (3.9)$$

The most simple experimental FROG arrangement is the same as a background free intensity autocorrelator as shown in fig. 3.1 except that the linear detector is replaced by a spectrometer. This arrangement is known as the SHG FROG and is shown in fig. 3.6. The spectrometer measures the spectrum of the SHG autocorrelation signal for each increment of the delay τ. The result is a spectrogram, or FROG trace, mapping out frequency vs. delay, from which one can retrieve the spectral phase and intensity profiles.

Due to its relatively simple geometry and its sensitivity, the SHG FROG is one of the most popular techniques for fs pulse characterisation. However, there are several limitations such as an ambiguity to the direction of time due to the symmetry of the trace and also the unintuitive trace. Other more intuitive FROG traces can be achieved
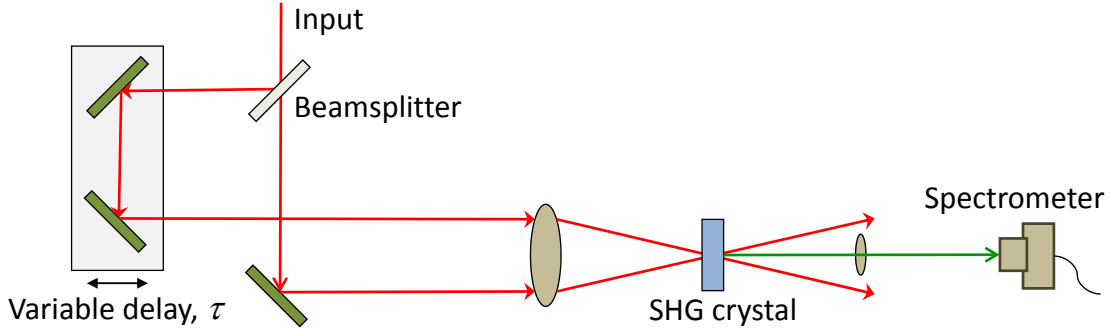
FIGURE 3.6: Schematic of the SHG FROG set-up.

with third order nonlinear arrangements such as PG (polarization gate) FROG and SD (self diffracting) FROG [11] but are not discussed here as they were not employed for the experimental measurements presented in this thesis.

Once the pulse has been measured using the FROG, the next task is to obtain quantitative information about the measured pulse from the FROG trace, such as the intensity and phase vs. time or frequency. The pulse can be retrieved from the trace by solving what is known as the two-dimensional (2D) phase-retrieval problem [24] which yields an essentially unique solution for $E(t)$. Most FROG algorithms are based on the iterative-Fourier-transform algorithm which is schematically shown in fig. 3.7 and the procedure is also later detailed step-wise. The most basic FROG retrieval algorithm uses the following procedure [11],

1. Begin with an initial guess for $E(t)$.

2. Generate the signal field $E_{sig}(t, \tau)$ and perform a Fourier transform with respect to t for $\widetilde{E}_{sig}(\omega, \tau)$ in the frequency domain.

3. The magnitude of the current guess $\widetilde{E}_{sig}(\omega, \tau)$ is replaced by the square root of the measured FROG trace intensity, $I_{FROG}(\omega, \tau)$,

$$\widetilde{E}_{sig}^{k}(\omega, \tau) = \frac{\widetilde{E}_{sig}(\omega, \tau)}{\left|\widetilde{E}_{sig}(\omega, \tau)\right|} \sqrt{I_{FROG}(\omega, \tau)}. \tag{3.10}$$

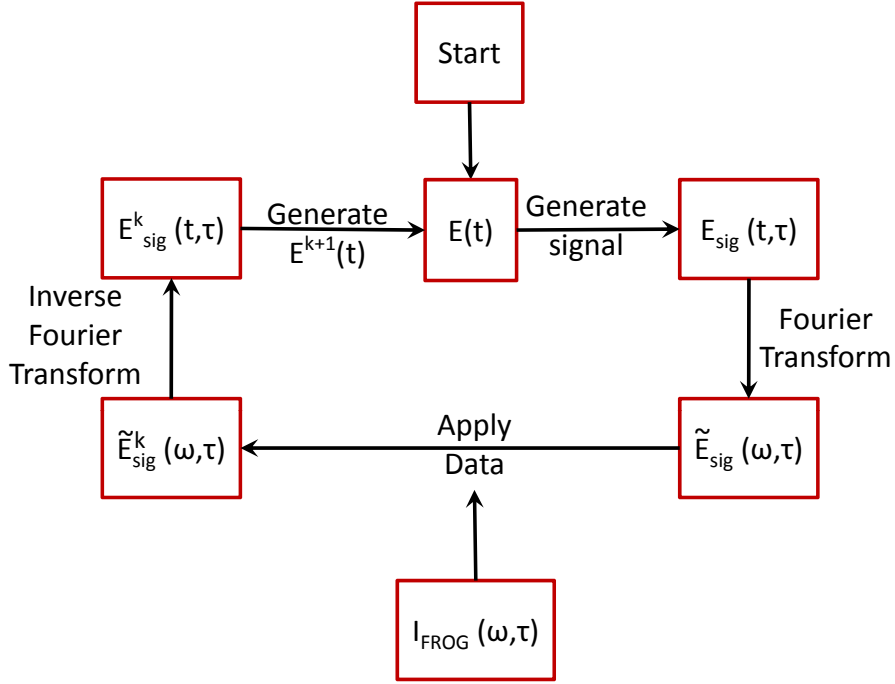4. Perform an inverse Fourier transform for $E_{sig}^{k}(t, \tau)$.

FIGURE 3.7: Schematic of a generic FROG retrieval algorithm.

5. Generate a new guess for the field $E^{k+1}(t)$ using $E_{sig}^k(t, \tau)$ according to,

$$E^{k+1}(t) = \int_{-\infty}^{\infty} E_{sig}^k(t, \tau) \, d\tau \ .$$
(3.11)

6. Iterate steps 2 to 6 until convergence.

In order to proceed with the algorithm described above, eqn. 3.8 has to be rewritten in a 2D form.

$$I_{FROG}(\omega, \tau) = \left| \int_{-\infty}^{\infty} \int_{-\infty}^{\infty} \widetilde{E}_{sig}(t, \Omega) \exp(-i\omega t - i\Omega \tau) \, dt \, d\Omega \right|^2 ,$$
(3.12)

where $\widetilde{E}_{sig}(t, \Omega)$ is the Fourier transform, with respect to τ, of $E_{sig}(t, \tau)$. Equation 3.12 can now be solved according to the 2D phase retrieval problem to find $\widetilde{E}_{sig}(t, \Omega)$ from which $E(t)$ can be easily derived.

When dealing with pulse retrieval, the Fast Fourier transform (FFT) is a convenient way of switching between the time and frequency domains. Due to the use of FFT in FROG algorithms, the data must initially be interpolated to a N×N grid, known as the Fourier

grid. This effectively couples the time and frequency domains and so it is important to ensure that the data is sufficiently sampled in both axes.

Convergence of the algorithm is usually measured by calculating the root mean square (RMS) error or FROG error, $G^{(k)}$ for each iteration k, and is defined as [11],

$$G^{(k)} = \sqrt{\frac{1}{N^2} \sum_{p,r=1}^{N} \left| I_{FROG}(\omega_p, \tau_r) - \mu I_{FROG}^{(k)}(\omega_p, \tau_r) \right|^2}, \qquad (3.13)$$

where $I_{FROG}(\omega_p, \tau_r)$ is the measured FROG trace, $I_{FROG}^{(k)}(\omega_p, \tau_r)$ is the kth iteration of the retrieved FROG data and μ is the normalisation constant that minimises the RMS error. This is used as a measure of convergence for most FROG retrieval algorithms, also for the work presented in this thesis.

However, the algorithm does not always converge, particularly in the presence of noise or for complex pulse intensities. A more reliable and faster type of algorithm is based on a concept known as generalized-projections (GP) which involves making *projections* or guesses for $E_{sig}(t, \tau)$ that satisfy either eqn. 3.9 or eqn. 3.8 on each iteration until eventually both constraints are satisfied. Satisfying eqn. 3.8 can be achieved simply by replacing the magnitude of the current guess with the measured trace, as in eqn. 3.10 from the iterative Fourier transform algorithm. Conforming to eqn. 3.9, however, requires a minimisation procedure to limit the functional distance between the previous guess calculated from $I_{FROG}(\omega, \tau)$ and the new guess calculated from eqn. 3.10. Although the GP procedure is faster than the basic FROG algorithm, the convergence is still slow when compared to an even faster method, that does not require this minimisation step, called principle component generalized projections (PCGP) [25]. This is discussed in detail in ref.[11, Chap. 21].

3.3 Comparison of Sonogram and XFROG for MIR Pulse Characterisation

As mentioned earlier, bond selective manipulation of matter with light has been a study of great interest to physicists, chemists and biologists. With ultrafast optical pulses,

the bond excitation occurs faster than the rapid redistribution of the energy away from the specific bond making it possible to drive a chemical reaction towards a desired product or even away from an undesired one [26]. Although many experiments have already achieved coherent control in the visible and near infrared (NIR) wavelength regimes, the most common molecular vibrational modes are in the mid infrared (MIR) region. Therefore, shaped femtosecond pulses in this fingerprint regime become important. These shaped pulses find various applications in driving conformational changes in proteins, spectroscopy, coherent control and imaging [1, 27–30].

Characterising pulses in the MIR is more difficult than for the visible or the NIR regions because commercially available devices like the SHG FROG are not readily available at these longer wavelengths. Adapting the available set-ups to the MIR is not straight forward because aspects such as the low energy of MIR pulses mean that standard charge-coupled device (CCD) detectors cannot be used directly with MIR light. Also, as in the set-up used for the experiments described in this thesis a MIR pulse is often accompanied by visible and NIR pulses as a result of the nonlinear conversions used to produce MIR. Usually, the type of pulses available dictate the most appropriate characterisation method. Self-referencing methods described earlier on in this chapter can also be used for the MIR pulses and one such method: the sonogram is tested experimentally against the XFROG technique where the availability of the pump pulse is used to its advantage.

In the experiments detailed in chapter 7, the idler pulse is characterised using either a sonogram or XFROG. In this section, the XFROG and CCS methods are compared as techniques for ultrashort MIR pulse characterisation. The sensitivity of each method is experimentally determined and the practical limitations of each technique are discussed and summarised in the last part of this section. Two sets of experiments were conducted to study their performances depending on the input power to the set-ups. In the first experiment, the input idler power to the sonogram/XFROG was varied using appropriate filters, keeping the pump power constant for the XFROG. In the second experiment, both the pump and the idler were varied by the same percentage as inputs to the XFROG. The main purpose of this study was to note the minimum idler power needed for idler characterisation and to test the performance of the XFROG set-up.

3.3.1 Experimental set-ups

The experimental set-up consists of a pump source, SPOPO and a sonogram or the XFROG. The pump source is a Nd:YLF laser and amplifier with pulse repetition rate of 120 MHz, typical peak power of 15 kW, and average pump power of up to 7 W, with 4 ps pulse-width at a wavelength of 1047 nm. The pump is directed through a telescopic arrangement so as to efficiently launch into the core of a polarisation maintaining (PM) single mode fibre which has an endcap of a coreless fibre to avoid fibre end damage. The average input power is reduced to a maximum of 3.5 W to be below the LC-SLM damage threshold as specified by the manufacturer. The MIR source ($\lambda_i = 3440$ nm) used for these sets of experiments is a periodically poled lithium niobate (PPLN) SPOPO pumped with the NIR pump source described above. This set-up is further detailed in chapter 7.

Independent measurements of the spectral intensity were acquired using a Czerny-Turner monochromator (Bentham M300) with a nitrogen-cooled InSb detector. The ACs were measured using the CCS arrangement with no spectral filtering.

3.3.1.1 Cross-Correlation Sonogram

The experimental arrangement for the CCS is shown in fig. 3.8. The input beam enters the sonogram setup and is split with a 50/50 pellicle beam splitter. This type of beam splitter virtually eliminates the multiple reflections commonly associated with a glass beam splitter and being made of a 2 μm thick nitrocellulose membrane, it also has minimal dispersion.

One part of the input beam was incident on a grating and a lens resulting in frequency-space mapping at the Fourier plane where a variable slit was placed. The slit was used for spectral filtering before the beam was retro-reflected. The other arm sets a variable temporal delay. The cross-correlations of the input pulse with the frequency-gated version of the pulse were then measured. The nonlinear process used was TPA, for which an extended InGaAs detector was used. Due to the collinearity of the experimental

set-up, interferometric cross-correlations were measured but the implementation of lock-in detection allowed for the interferometric frequencies to be filtered out as well as significantly increasing the sensitivity of the sonogram. A full sonogram trace comprised of 80 intensity cross-correlations, each at a different frequency. The complete trace was acquired in less than 7 minutes.
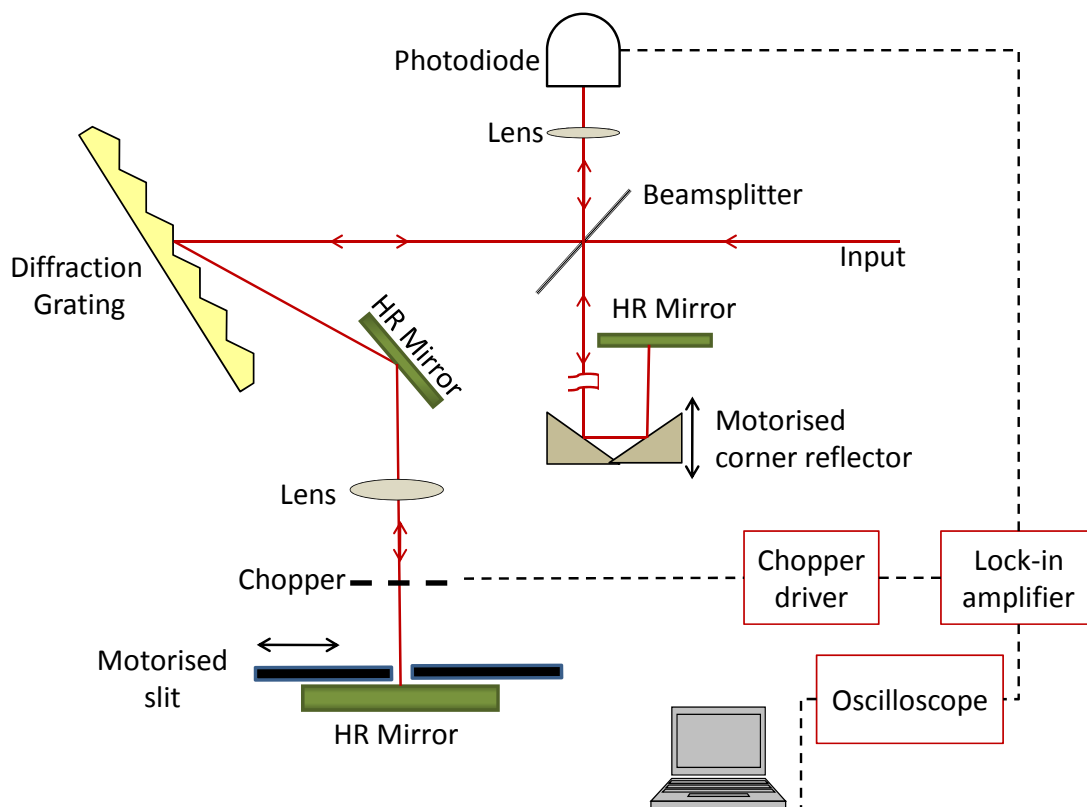

FIGURE 3.8: Schematic of the experimental CCS arrangement. The path lengths of the two arms are not drawn to scale (indicated in the figure).

The resolution of the CCS arrangement was controlled by the slit-width of the spectral gating arm. Narrowing the slit corresponded to higher spectral resolution but resulted in a temporally broadened gate pulse so care was taken to ensure that the motorised stage of the temporal delay arm had enough travel to measure the entire cross-correlation. Calibration of the temporal domain depended on the speed of the motorised corner reflector and the frequency calibration was calculated using the grating equation for the frequency-space mapping at the Fourier plane. For this particular setup, the frequency to space mapping was 10nm/mm and the slit width was 0.4 mm corresponding to ~1/10th of the total bandwidth.

A retrieval algorithm, as described in sections 3.2.3 and 3.2.4 was used following noise filtering of the data and interpolation to a 128×128 Fourier grid. The quality of the retrieval was assessed by comparison of the retrieved data to the measured spectral intensity and autocorrelation traces.

3.3.1.2 Cross-Correlation Frequency Resolved Optical Gating

Experimental configuration of the XFROG is shown in fig. 3.9. The idler and depleted pump beams from the SPOPO are both synchronous and collinear, making them convenient for use in this arrangement. The pump beam was reflected by a coated CaF_2 chromatic beam-splitter that was highly reflecting at the pump wavelength but transmissive at the idler wavelength (indicated by B/S in the figure). A telescope (not shown) then resized the pump beam to a spot size of ~ 2 mm before a temporal delay was imposed using two mirrors on a motorised stage. The idler beam passed through a long wave pass (LWP) filter to remove any residual wavelengths from the SPOPO while travelling on a fixed path length. The idler beam had a spot size of ~ 3 mm. The two beams were then recombined with another CaF_2 chromatic beam-splitter before being focussed with a 50 mm focal length CaF_2 lens into a 1 mm PPLN crystal to host the DFG process. The initial spot sizes of the pump and idler were chosen carefully such that near confocal focussing could be achieved in the crystal. The grating period used in the PPLN was the same as that used in the SPOPO, generating a signal beam at $\lambda_s = 1505$ nm. The signal was detected using a fibre-coupled optical spectrum analyser (OSA) (Ando AQ-6310C) that was set at its minimum resolution of 0.1 nm and maximum sensitivity of -49 dBm. A typical XFROG trace composed of 100 spectra acquired in ~ 3 minutes.

Two sets of experiments were conducted to study their performances depending on the input power to the set-ups. In the first experiment, the input idler power to the sonogram/XFROG was varied using appropriate neutral density (ND) filters, keeping the pump power constant for the XFROG. For the sonogram the ND filters were placed before the idler entered the set-up, whereas for the XFROG the idler was attenuated after the pump and the idler beams had been separated in the set-up. In the second experiment, both the pump and the idler were varied by the same percentage as inputs
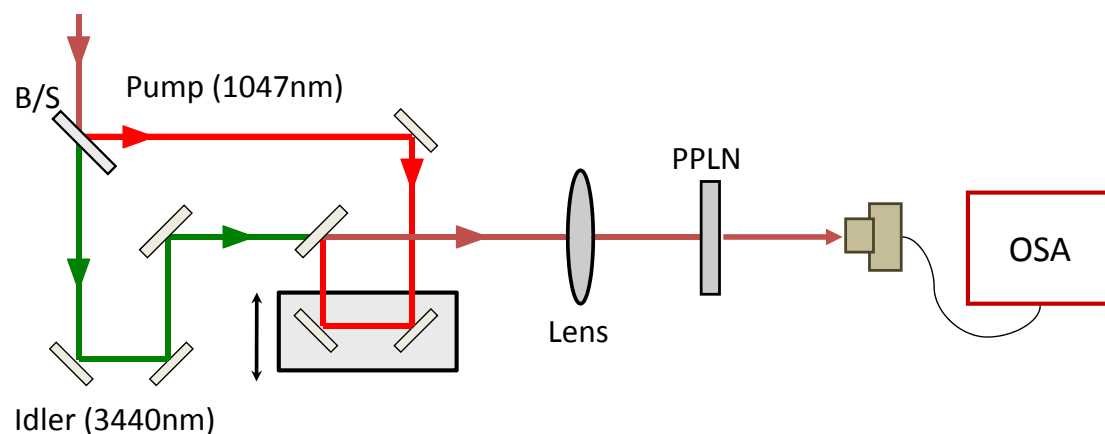
FIGURE 3.9: Schematic of experimental XFROG arrangement. B/S: beam splitter.

to the XFROG. For this, the pump was also attenuated in the same way as the idler. The main purpose of this study was to note the minimum idler power needed for idler characterisation and to test the overall performance of the XFROG and CCS set-ups.
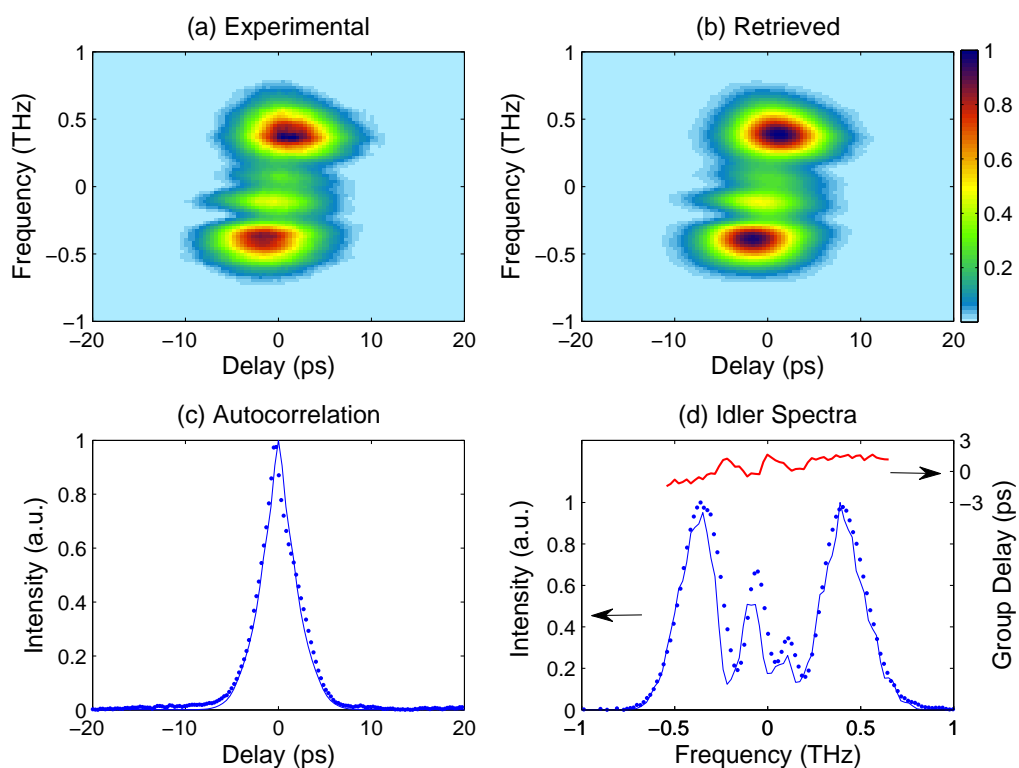

FIGURE 3.10: (a) Experimental and (b) retrieved sonogram data for high idler input power of 30 mW. Measured(dotted) and retrieved (solid lines) (c) autocorrelation and (d) idler spectra are also shown.
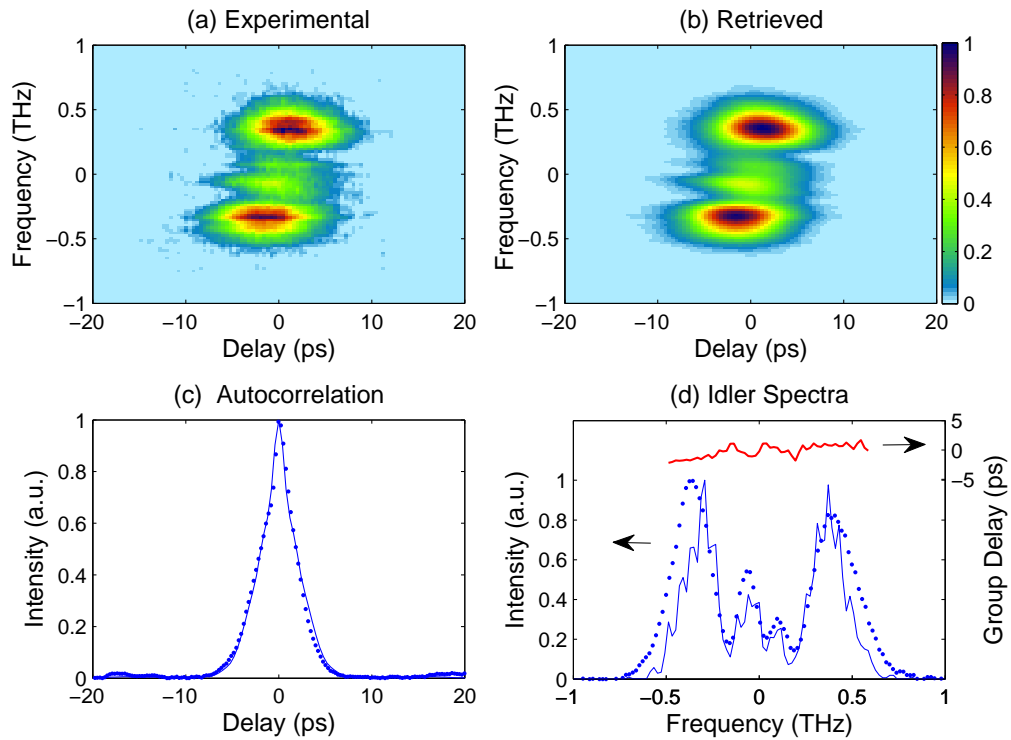
FIGURE 3.11: (a) Experimental and (b) retrieved sonogram data for low idler input power of 13 mW. Measured(dotted) and retrieved (solid lines) (c) autocorrelation and (d) idler spectra are also shown.

3.3.2 Results and analysis

In these experiments, the idler beam from the SPOPO at a wavelength of 3440 nm was first characterised with the cross correlation sonogram and then using a XFROG set-up. The SPOPO was operated under the standard conditions for high fidelity transfer of pulse shape from the NIR to the MIR, as described later in chapter 7. The OPO was pumped with chirped pulses, thus delivering chirped ider pulses to test the char-acterisation capabilities of both the set-ups. The pulse profile was retrieved from the sonogram/XFROG data using appropriate Matlab programs written by J. Prawiharjo.

Varying idler

The idler output from the SPOPO was collimated using a one-to-one telescope and di-rected to the sonogram. Different sets of data were obtained as the input idler power level was varied by using appropriate ND filters. Full idler power was measured to be 35 mW
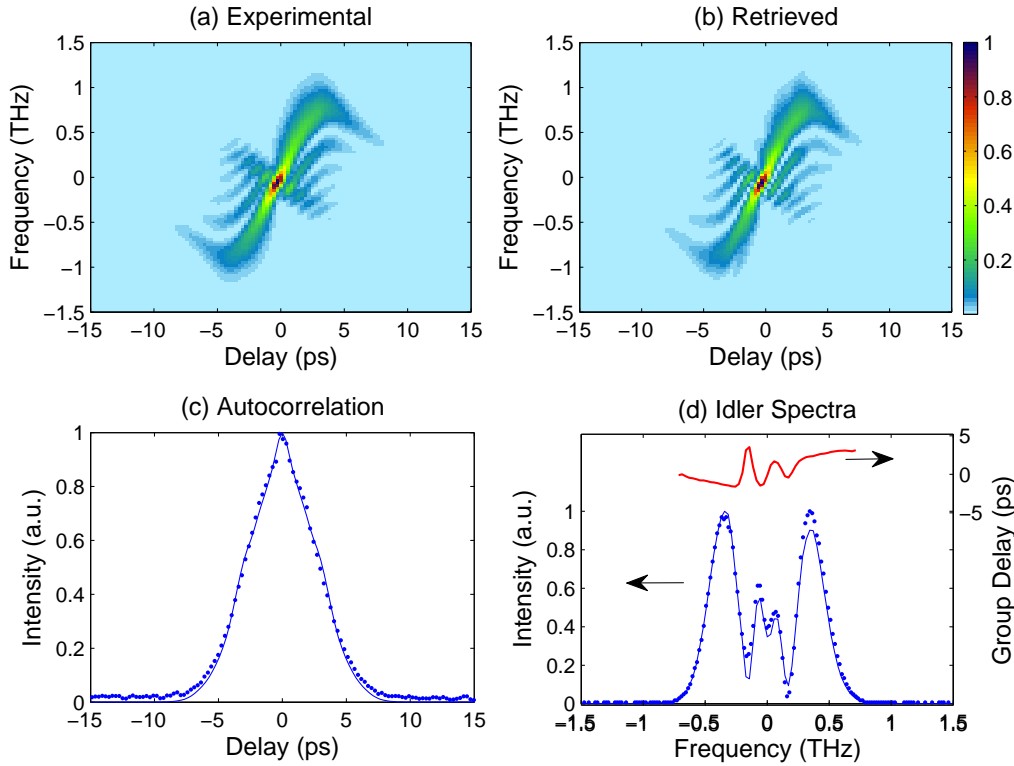
FIGURE 3.12: (a) Experimental and (b) retrieved XFROG data for high pump (115 mW) and high idler (70 mW) input power. Measured(dotted) and retrieved (solid lines) (c) autocorrelation and (d) idler spectra are also shown.

which reduced to 30 mW with the two lenses in place for the telescopic arrangement. The sonogram trace obtained in this case is shown in figure 3.10.

Retrievable sonogram traces are obtained for idler power as low as 13 mW, with the result indicated in figure 3.11. We can see that the retrieved trace begins to deviate from the measured as the input idler power begins to decrease. Other data sets for idler powers between 30 mW and 13 mW were also obtained but only those for the full and the minimum idler powers are shown here to highlight the operation range of the device. Measurements for power levels below 13 mW were also taken but the program could not retrieve at lower powers.

In a similar experiment, the input idler power to the XFROG was varied using filters, keeping the pump constant at 115 mW. The idler was varied from a full power of 70 mW to as low as 1 mW using appropriate filters. Figure 3.12 shows the experimental and the retrieved traces along with the autocorrelation and the idler spectra for input pump
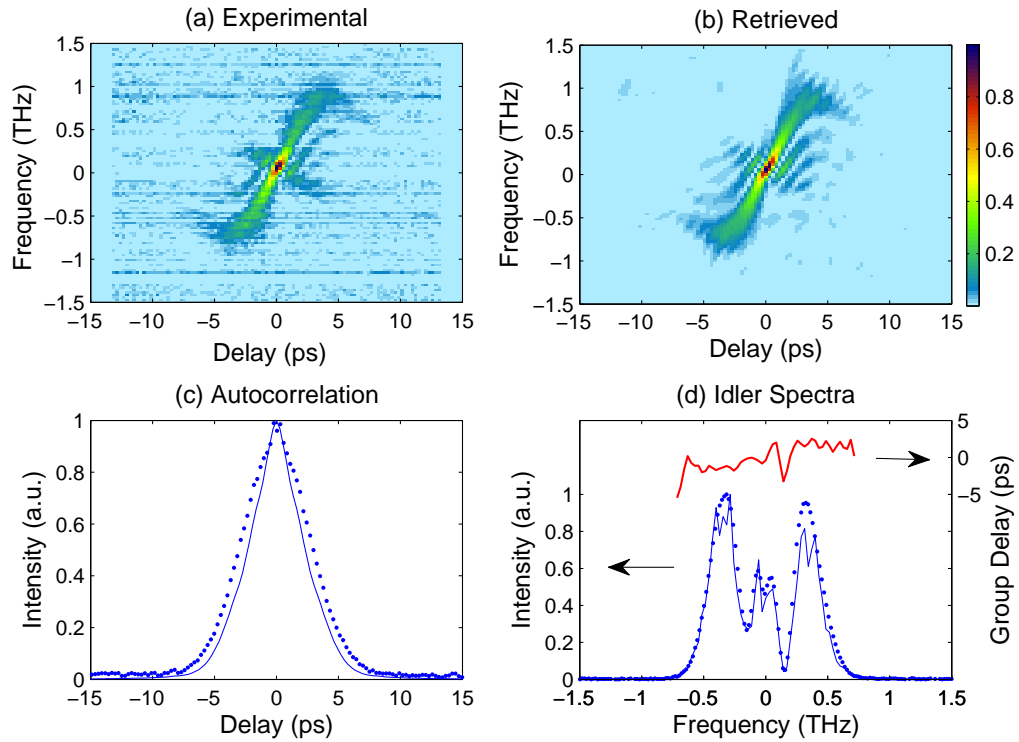
FIGURE 3.13: (a) Experimental and (b) retrieved XFROG data for high pump (115 mW) and low idler (1 mW) input power. Measured(dotted) and retrieved (solid lines) (c) autocorrelation and (d) idler spectra are also shown.

power of 115 mW and the idler power of 70 mW. We see that the measured and the retrieved data match well in this case.

In the other case with the pump power maintained at 115 mW but with the idler power down to as low as 1 mW, the data is still retrievable but begins to differ from the measured set. With idler power lower than this value, the data was no longer retrievable, setting a lower limit for the operation of the XFROG set-up.

As we can see from the data plots for the sonogram and the XFROG, the sonogram trace is more intuitive but the XFROG is able to retrieve data for a much lower value of the idler power. This is so because it utilises pump that will always be present in the OPO set-up. Also, unlike in the sonogram, the idler power in XFROG set-up is not filtered before the nonlinear process.

Varying pump and idler

The XFROG involves two inputs; the pump as the reference pulse and the idler (the pulse to be characterised). To complete the characterisation by varying the input power levels, in the following experiment, both the pump and the idler powers to the XFROG were varied by the same percentage of the full power levels. The full input pump and idler powers were 163 mW and 47 mW respectively. Figure 3.14 indicates the trace for high pump and idler inputs.
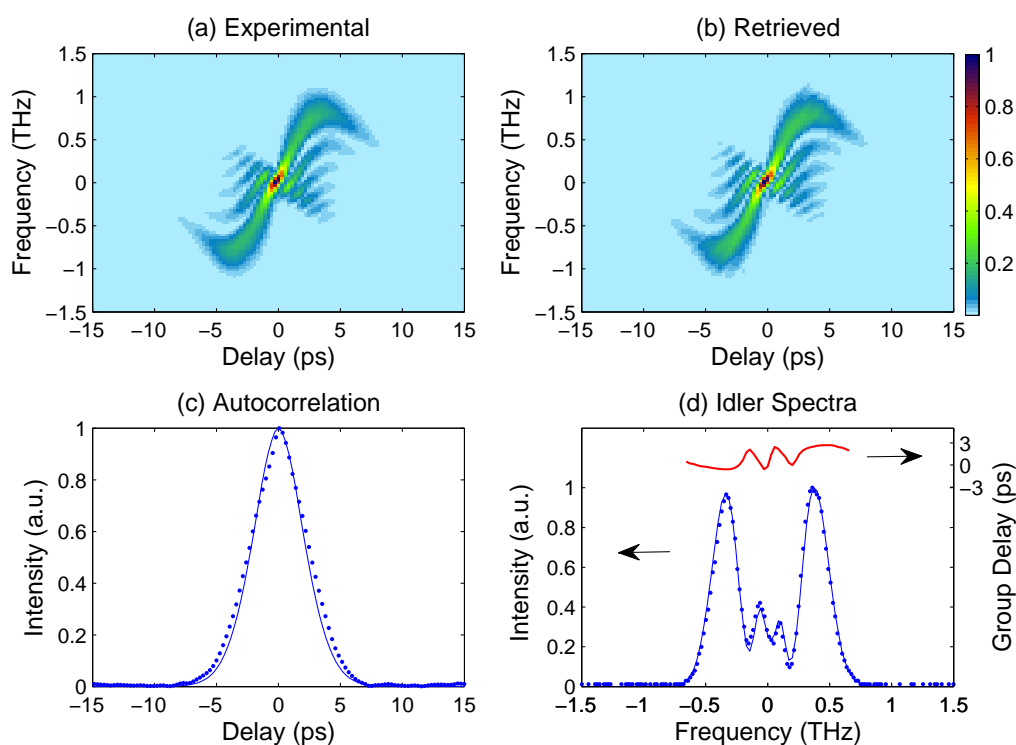

FIGURE 3.14: (a) Experimental and (b) retrieved XFROG data for high pump (115 mW) and idler (70 mW) input powers. Measured(dotted) and retrieved (solid lines) (c) autocorrelation and (d) idler spectra are also shown.

The figure 3.15 shows the data set obtained when the input powers were 6.5% of the maximum available powers. That is, for pump power of 10.6 mW and the idler power of 3.1 mW.

With the available filters, the next data set was obtained for 2.25% of the initial power levels but the data was not retrievable. Thus, the minimum operation point for the
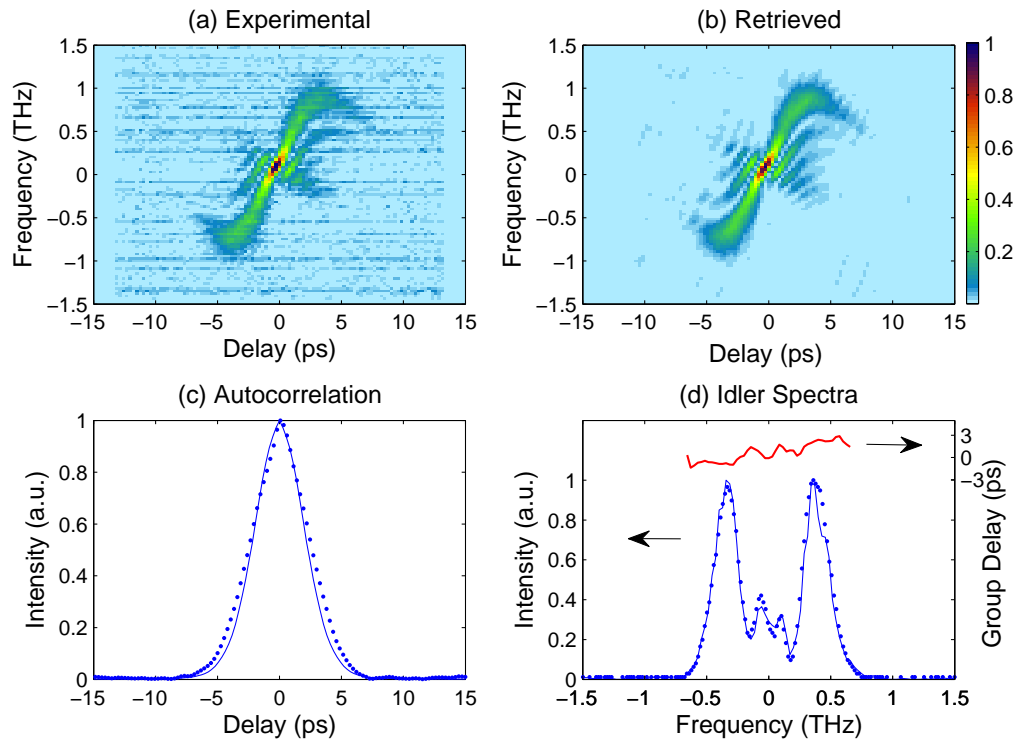
FIGURE 3.15: (a) Experimental and (b) retrieved XFROG data for low pump (10.6 mW) and idler (3 mW) input powers. Measured(dotted) and retrieved (solid lines) (c) autocorrelation and (d) idler spectra are also shown.

XFROG in this case is for powers somewhere between 6.5% and 2.25% of the initial full value.

Analysis

The results from the pulse characterisation technique comparisons show that the XFROG is convincingly more sensitive than the sonogram even when phase sensitive detection was used with sonogram and not XFROG. Retrievable traces for the sonogram could be achieved for the minimum idler input power of 13 mW, whereas the XFROG could characterise pulses with idler powers as low as 1 mW with 115 mW pump and 3 mW idler power with 10.6 mW of pump power.

The reason for this difference in sensitivity is related to losses in the two set-ups owing to the optical elements used and the noise contributions. The losses in the XFROG set-up were mainly due to transmission through the CaF_2 mirrors, a 60% efficient LWP filter

for the idler beam, uncoated lenses used for focussing the beams into the PPLN crystal followed by the fibre-coupled OSA. In contrast, the sonogram set-up incurs significant loss due to the spectral filter (slit) which allows only one-tenth of the total bandwidth for better pulse resolution. Other major sources of loss are the diffraction grating and the 50/50 beam splitter used in the set-up. In terms of the noise contributions, the sonogram set-up was quite prone to mechanical noise from the optical chopper and the time-delay motor. The XFROG, on the contrary, had no mechanical movement during data acquisition and thus free from noise.

3.4   Summary

There are various methods available for characterising femtosecond pulses. A choice for the measuring technique can be made depending on the method that best suits the experiment in hand as well as the properties of the laser source including the wavelength, repetition rate and the availability of additional pulses to act as reference pulse, etc. Cost of the set-up, robustness, sensitivity, easy access to the optics required are also some other factors that play an important role.

For the particular experiment where XFROG and sonogram are employed as pulse characterisation techniques, both have the advantage of being simple, relatively inexpensive arrangements. The advantages and disadvantages of each are summarised in table 3.1. However, in this case, because of a higher sensitivity to idler power, the XFROG has now replaced the sonogram as our short pulse characterisation method of choice for MIR OPOs.

Criteria	Sonogram	XFROG
Trace	Intuitive trace	Non-intuitive trace
Retrieval	Requires deconvolution step presenting instabilities in the retrieval.	No deconvolution step needed.
Sensitivity	Power reduction before nonlinear process. Phase sensitive detection needed.	DFG process is sensitive. Standard OSA needed for signal detection.
Calibration	Calculated from speed of motor for time and angle of diffraction grating for frequency calibration.	No calibration required.
Cost	Cheap TPA detector needed.	PPLN and OSA are costly. Readily available in the lab.
Noise	Motors and chopper cause mechanical noise.	No moving parts during data acquisition.
Alignment	Very sensitive due to small detector head.	Use of large area Ge detector makes initial alignment relatively simpler.
AC measurement	Can be performed with same set-up.	Separate apparatus needed.
Spectrum	Needs another device.	Needs another device.
Wavelength tuning	Tuned by rotating grating. Gives good range.	Good range achieved by PPLN grating and temperature tuning.
Resolution	Slit width needs to be reduced for better spectral resolution which leads to low signal level which in turn affects the temporal resolution.	Spectral resolution can be high and fixed at 0.1nm. Temporal resolution is measured by number of steps. Both are independent.

TABLE 3.1: Pros (green) and Cons (red) of Sonogram and XFROG as methods of MIR pulse characterisation.

References

[1] J. M. Dela Cruz, I. Pastirk, M. Comstock, V. V. Lozovoy, and M. Dantus, "Use of coherent control methods through scattering biological tissue to achieve functional imaging," *PNAS* **101**, pp. 16996–17001, 2004.

[2] M. C. Chen, J. Y. Huang, and L. J. Chen, "Coherent control multiphoton processes in semiconductor saturable bragg reflector with freezing phase algorithm," *Appl. Phys. B* **80**, pp. 333–340, 2005.

[3] J. M. Dela Cruz, I. Pastirk, V. V. Lozovoy, K. A. Walowicz, and M. Dantus, "Multiphoton intrapulse interference 3: Probing microscopic chemical environments," *J. Phys. Chem. A.* **108**, pp. 53–58, 2004.

[4] N. Dudovich, D. Oron, and Y. Silberberg, "Single-pulse coherently controlled nonlinear raman spectroscopy and microscopy," *Nature* **418**, pp. 512–514, 2002.

[5] N. Dudovich, D. Oron, and Y. Silberberg, "Single-pulse coherent anti-stokes raman spectroscopy in the fingerprint spectral region," *J.Chem.Phys.* **118**, pp. 9208–9215, 2003.

[6] D. J. Bradley and G. H. C. New, "Ultrashort pulse measurements," *Proceedings of the IEEE* **62**(3), pp. 313–345, 1974.

[7] C. Froehly, B. Colombeau, and M. Vampouille, "Shaping and analysis of picosecond light-pulses," *Progress in Optics* **20**, pp. 65–153, 1983.

[8] A. Laubereau, "Optical nonlinearities with ultrashort pulses," *Topics in Applied Physics* **60**, pp. 35–112, 1988.

[9] I. A. Walmsley and C. Dorrer, "Characterization of ultrashort electromagnetic pulses," *Adv. Opt. Photon.* **1**(2), pp. 308–437, 2009.

[10] J.-C. Diels and W. Rudolph, *Ultrashort Laser Pulse Phenomena- Fundamentals, Techniques, and Applications on a Femtosecond Time Scale*, Academic Press, second ed., 2006.

[11] R. Trebino, *Frequency-Resolved Optical Gating: The Measurement of Ultrashort Laser Pulses*, Kluwer Academic Publishers, 2000.

[12] H. P. Weber, "Method for pulsewidth measurement of ultrashort light pulses generated by phase-locked lasers using nonlinear optics," *Journal of Applied Physics* **38**(5), pp. 2231–2234, 1967.

[13] J. C. M. Diels, J. J. Fontaine, I. C. McMichael, and F. Simoni, "Control and measurement of ultrashort pulse shapes (in amplitude and phase) with femtosecond accuracy," *Applied Optics* **24**(9), pp. 1270–1282, 1985.

[14] D. T. Reid, W. Sibbett, J. M. Dudley, L. P. Barry, B. Thomsen, and J. D. Harvey, "Commercial semiconductor devices for two photon absorption autocorrelation of ultrashort light pulses," *Applied Optics* **37**(34), pp. 8142–8144, 1998.

[15] J. K. Ranka, A. L. Gaeta, A. Baltuska, M. S. Pshenichnikov, and D. A. Wiersma, "Autocorrelation measurement of 6-fs pulses based on the two-photon-induced photocurrent in a gaasp photodiode," *Optics Letters* **22**(17), pp. 1344–1346, 1997.

[16] K. A. Briggman, L. J. Richter, and J. C. Stephenson, "Imaging and autocorrelation of ultrafast infrared laser pulses in the 3-11μ mrange with silicon ccd cameras and photodiodes," *Optics Letters* **26**(4), pp. 238–240, 2001.

[17] E. B. Treacy, "Measurement and interpretation of dynamic spectrograms of picosecond light pulses," *Journal of Applied Physics* **42**(10), pp. 3848–3858, 1971.

[18] J. L. A. Chilla and O. E. Martinez, "Analysis of a method of phase measurement of ultrashort pulses in the frequency-domain," *IEEE Journal of Quantum Electronics* **27**(5), pp. 1228–1235, 1991.

[19] D. T. Reid, "Algorithm for complete and rapid retrieval of ultrashort pulse amplitude and phase from a sonogram," *IEEE Journal of Quantum Electronics* **35**(11), pp. 1584–1589, 1999.

[20] D. T. Reid and J. Garduno-Mejia, "General ultrafast pulse measurement using the cross-correlation single-shot sonogram technique," *Optics Letters* **29**(6), pp. 644–646, 2004.

[21] V. Wong and I. A. Walmsley, "Ultrashort-pulse characterization from dynamic spectrograms by iterative phase retrieval," *J. Opt. Soc. Am. B* **14**(4), pp. 944–949, 1997.

[22] P. Nuernberger, G. Vogt, T. Brixner, and G. Gerber, "Femtosecond quantum control of molecular dynamics in the condensed phase," *Physical Chemistry Chemical Physics* **9**(20), pp. 2470–2497, 2007.

[23] N. A. Naz, M. V. O'Connor, D. P. Shepherd, and D. C. Hanna, "An intelligent, synchronously pumped optical parametric oscillator using adaptive pulse-shaping techniques," *2005 Conference on Lasers and Electro-Optics (CLEO), Vols 1-3* , pp. 1841–1843, 2005.

[24] R. C. Eckardt, C. D. Nabors, W. J. Kozlovsky, and R. L. Byer, "Optical parametric oscillator frequency tuning and control," *Journal of the Optical Society of America B-Optical Physics* **8**(3), pp. 646–667, 1991.

[25] D. J. Kane, "Principal components generalized projections: A review [invited]," *J. Opt. Soc. Am. B* **25**(6), pp. A120–A132, 2008.

[26] N. Bloembergen and A. H. Zewail, "Energy redistribution in isolated molecules and the question of mode-selective laser chemistry revisited," *Journal of Physical Chemistry* **88**(23), pp. 5459–5465, 1984.

[27] R. S. Judson and H. Rabitz, "Teaching lasers to control molecules," *Physical Review Letters* **68**(10), pp. 1500–1503, 1992.

[28] R. N. Zare, "Laser control of chemical reactions," *Science* **279**(5358), pp. 1875–1879, 1998.

[29] A. P. Peirce, M. A. Dahleh, and H. Rabitz, "Optimal-control of quantum-mechanical systems - existence, numerical approximation, and applications," *Physical Review A* **37**(12), pp. 4950–4964, 1988.

[30] R. J. Levis, G. M. Menkir, and H. Rabitz, "Selective bond dissociation and rearrangement with optimally tailored, strong-field laser pulses," *Science* **292**(5517), pp. 709–713, 2001.

Chapter 4

Adaptive phase shaping in a femtosecond Yb-fibre chirped pulse amplification system

4.1 Introduction

High energy femtosecond pulses are required for a wide range of industrial and scientific applications such as ultrafast spectroscopy, pumping parametric devices, material processing and plasma-based x-ray generation. High energy femtosecond pulses can be generated using the CPA technique where the initially low-energy pulse is temporally stretched before amplification to avoid the nonlinear effects that can occur when high-intensity pulses propagate in an optical fibre. The high energy pulses are then recompressed in free space using bulk diffraction gratings [1]. Compared to the traditional bulk crystal and glass laser sources, Yb-fibre based systems can be directly diode-pumped, have high gain and suffer less from thermo-optical problems, making them attractive high-power laser sources [2]. However, due to long device lengths of up to several metres and a highly confined mode area, ultrafast fibre CPAs can still suffer from nonlinear effects such as SPM. These nonlinear effects can degrade the pulse quality, limiting the maximum available power from the femtosecond source.

One of the methods to overcome these pulse distortions is to incorporate an adaptive pulse shaper [3] in the set-up. This technique has been used with Ti:Sapphire-based

bulk CPA systems to overcome SPM, as well as the induced distortions due to any residual strecther/compressor dispersion mismatch [4–7]. Recently, adaptive shaping technology was used for the very first time in a fibre-based CPA system [8]. In this report, Schimpf et al. [8] describe pre-shaping the spectral amplitude of the pulse and show high quality pre-compensation of pulses at B-integrals as high as 16. The selected computer-controlled feedback parameter was a pre-defined target spectral shape and it was shown that imposing a parabolic shape was superior to a Gaussian shape for pulse energies up to 20 nJ and pulse durations of 300 fs at average powers of 1.5 W. Thus, although the reported B-integral in this report was high, the pulse energy is orders of magnitude lower compared to the pulse energy reported in the work presented in this chapter.

The B-integral here is defined as the total nonlinear phase shift accumulated in a passage through the device along the optical axis and is mathematically given by,

$$B = \frac{2\pi}{\lambda} \int n_2 I(z) dz \tag{4.1}$$

where $I(z)$ is the optical intensity along the beam axis, z is the position along the propagation direction, and n_2 is the nonlinear refractive index.

This chapter presents an Yb-fibre CPA system with an adaptive phase-only pulse shaper incorporated in the set-up for improved output pulse quality [9]. The approach used here was to pre-compensate for the SPM and higher order dispersion by spectral phase shaping the pulse. This produced high-quality 800 fs, 65 μJ pulses. The system described in this chapter used large-mode-area (LMA) PCF amplifiers and a dielectric grating compressor. Two alternative stretchers, bulk and fibre, were employed and their use is compared later. The bulk stretcher used here was set so that its dispersive characteristics were matched to that of the compressor. In the other variant, a 5 km fibre stretcher was used which resulted in substantially mismatched third order dispersion after the compressor.

A LC-SLM was used as the pre-compensating pulse shaper and placed before the stretcher in either case. The shaper was placed before the amplifiers to avoid any damage resulting

from high pulse energy or high average power. In the situation where the pulse propagates through a dispersive stretcher for a long distance, such that the temporal intensity profile becomes proportional to the spectral intensity, that is I(t)$\sim$ I(ω), then SPM in the amplifier section merely introduces a frequency dependent phase with negligible effect on the spectral bandwidth of the pulse [10, 11]. Such a frequency-dependent phase could be readily pre-compensated by a phase-only pulse shaper. Sato et al, [12], have reported numerical modelling of adaptively shaping femtosecond pulse propagation in a fibre, showing that phase-only shaping can pre-compensate for group delay dispersion (GDD) and SPM. However, they also report that this pre-compensation is only successful up to 100 kW power for a 0.114 m length of single-mode fibre. Similarly, Braun et al, [10], reported numerical modelling of phase-only pre-compensation in a fibre CPA system showing promising results for nonlinear phase of up to 3 rad. Schreiber et al, [13], in another study report numerical modelling of spectral amplitude pre-compensation in a fibre CPA system with large amounts of SPM, confirming the experimental results described in [14].

In this experiment, we shape the spectral phase of the input pulses using a liquid-crystal phase-only pulse shaper to produce the optimum output pulses for operating with significant variation in the cumulative SPM in the system arising due to variable repetition rates. Establishing the appropriate pre-shaped phase is challenging because of the overall system complexity and we implemented an adaptive learning loop to maximise the output autocorrelation peak, which avoids the uncertainties of complex nonlinear simulations. Two slightly different set-ups were used as the stretcher in the system. First, a bulk stretcher which had second and third order dispersion matched to the compressor was incorporated. After this, a 5 km fibre as the pulse-stretcher was used.

Both, simulated annealing [15] and genetic algorithms [16] have been used for CPA system optimisations before. A generalised simulated annealing (GSA) [17] control algorithm was used for this set of experiments. The control algorithm optimised a reduced set of Taylor coefficients for the shaper phase profile to optimise the magnitude of the autocorrelation peak. 2.9 times improvement was obtained for the bulk stretcher arrangement leading to close to transform-limited output pulse durations of 800 fs at 65 μJ

at the corresponding B-integral of $\sim$8. With the fibre stretcher in the set-up for the same pulse energy, 3.4 times improvement in the autocorrelation peak compared to the un-shaped pulses was observed, although it was further away from the transform-limited pulse duration as compared to the result obtained for the bulk grating stretcher.

The chapter is organised as follows. In section 4.2, the experimental techniques along with the implementation of the adaptive control are detailed. The optimisation results are presented in section 4.3 and the chapter then concludes in section 4.4. The fibre CPA system had previously been constructed by members in the group of Prof. D.J. Richardson at the ORC. The experimental work presented in this chapter was carried out in collaboration with Fei He and Hazel Hung. The optimisation algorithm used here was written by Naveed Naz.

4.2   Experimental Set-up

Fibre CPA system

The schematic of the phase controlled Yb-fibre CPA system is shown in figure 4.1. The seed laser pulses ($\sim$500 fs, λ_0=1053 nm, $\Delta\lambda$ $\sim$3 nm) were first phase-shaped then stretched in duration with either a pair of bulk gratings or a 5 km length of Corning SMF28e fibre. Although the fibre stretcher is simple and convenient to use, high order dispersion from the stretcher cannot be matched by the grating compressor later as it can with the bulk grating pair stretcher. With no phase applied, the pulse duration at the output of the stretcher was measured to be 1 ns for the dielectric grating stretcher and 0.8 ns for the fibre stretcher. For the high energy results, an electro-optic modulator (EOM) reduced the repetition rate from 80 MHz to 100 kHz before amplification to 0.1 W using core-pumped Yb-fibre pre-amplifiers. Following this two AOMs are used to reduce the repetition rate further to 16.67 kHz. Two cladding pumped amplifiers were then used to achieve high pulse energies and average powers. The cladding pumped amplifiers comprised 2 m lengths of double-clad Yb-doped photonic crystal fibres pumped at 975 nm. For experiments with either of the two stretcher set-ups, the launched pump power is estimated to be 3 W into the final amplifier. The launched energy at the input
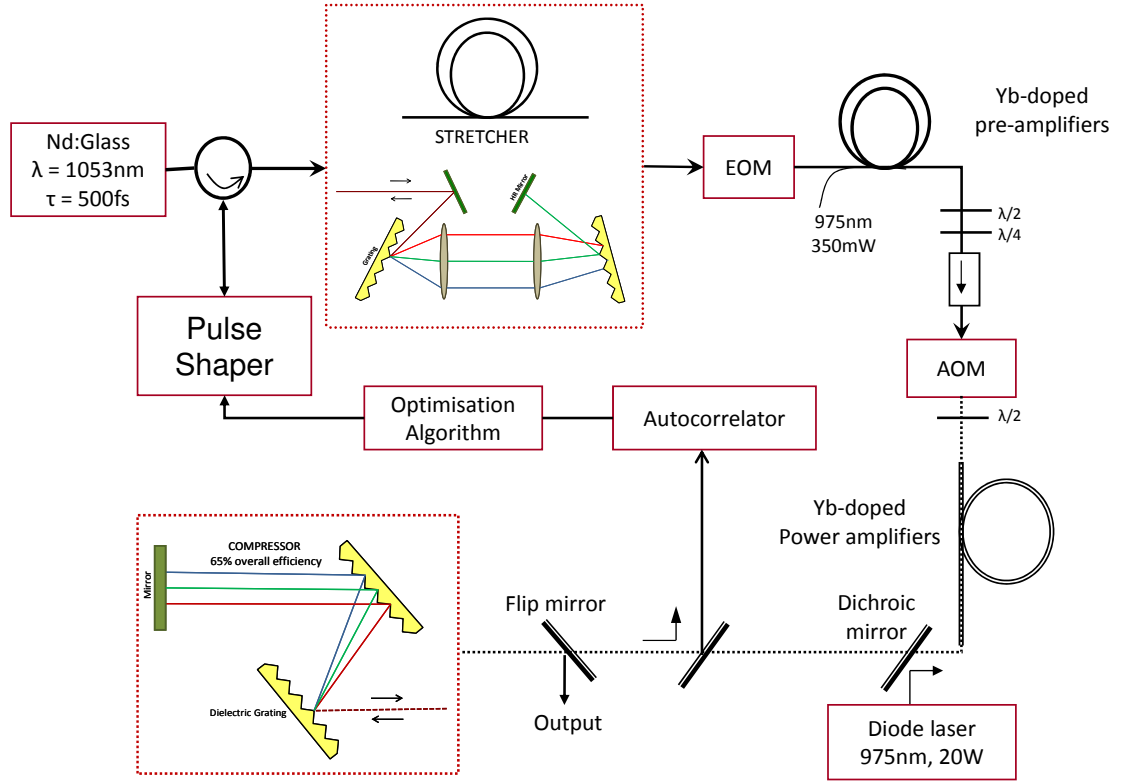
FIGURE 4.1: Schematic of the fibre CPA system.

and output of the final amplifier stage is calculated to be $2\,\mu$J and $100\,\mu$J respectively. A dielectric grating compressor with 65% overall transmission efficiency recompressed the pulses in the final stage.

Pulse shaper and control loop

The pulse shaper used in the set-up included a telescope (f=12 mm and 200 mm) to expand the input beam-waist to be less than 15 mm in diameter, as shown in figure 4.2. A beam diameter of 12 mm was achieved so that the FWHM beam spot size of the individual frequency components [3] on the LC-SLM was $\sim$50 μm. The diffraction grating with a groove density of 1100 lines/mm was oriented at $\sim$10 degree incidence angle (θ_{in}) with the diffracted angle as $\sim$80 degrees. These values are according to the equations discussed in section 2.2.2 [3]. A cylindrical lens (f=200mm) then focussed the beam, and a 12.8 mm wide, 128 pixel, phase-only LC-SLM (CRi SLM-128-MIR) was placed

Parameter	Value
Central wavelength, λ	1053 nm
Input spot size, w_{in}	6 mm
Grating groove density, d	1100 lines/mm
Incident angle on grating, θ_{in}	9.97^o
Diffracted angle, θ_d	80.03^o
Focal length, f	200 mm
Spatial dispersion, α	7.5 x 10^{-16} m/(rad/s) or 0.78 nm/mm
Radius of single frequency component, w_0	64.4 μm
Complexity, η	236.16
Spectral resolution, $\delta\lambda$	0.04 nm
Temporal resolution, δt	163 fs
Time window, T	38.5 ps

TABLE 4.1: Pulse shaper design parameters.

at the Fourier plane of the folded 4-f shaper set-up [3]. These design parameters are summarised in table 4.1.
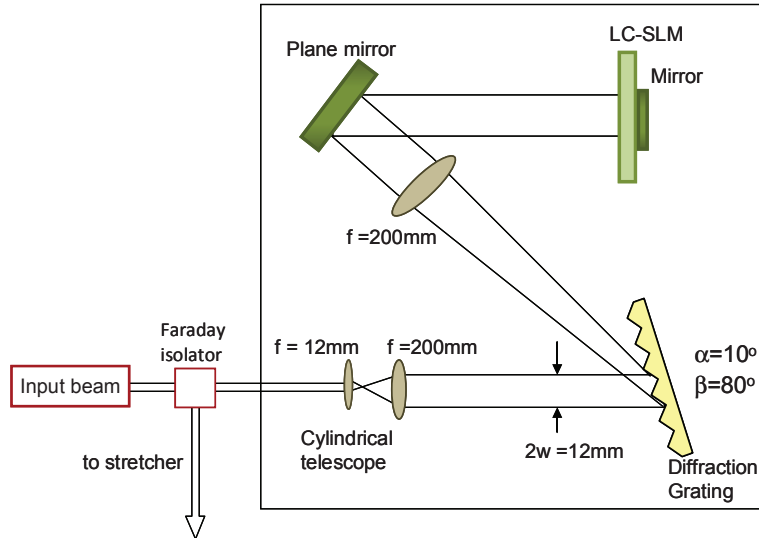
FIGURE 4.2: Folded 4-f pulse shaper set up

The parameters in table 4.1 are calculated without taking into account the pixellation of the shaper. However, the maximum complexity that can be achieved is limited by the number of pixels, that is, $\eta_{max} = 128$. Thus, the finest spectral feature that can be manipulated is 0.078 nm and the time window is 20 ps. It is worth noting that while the time window is the period over which the output pulse is affected by the mask, it can still be employed in shaping the pulses stretched to durations much longer than T, as is the case for this experiment.

The adaptive control in this situation enforces phase wrapping (that is, the phase is constrained to an interval such as $(-\pi, \pi)$) between the limits of 1 and 11 radians for 1053 nm pulse, if higher magnitude phase profiles are required. Spectral distortions were observed experimentally where these phase wrappings occur due to localised parts of the beam being diffracted out as a result of the phase discontinuity. This had little effect when the phase profiles were wrapped only near the wings of the pulse. Another consequence of the shaper pixellation is to limit the complexity of the phase profile. The sampling theorem [18], states that for a signal whose highest frequency component is ν, the sampling must be acquired at a minimum rate of 2ν called the Nyquist frequency. Therefore, for a mask of N_{pix} pixels, the maximum number of modulations that can be sampled is $N_{pix}/2$. Thus, if alternate pixels are programmed to apply a phase shift of π, the maximum phase change between pixels can be π. Thus the maximum rate of change of phase with frequency $d\phi/d\omega$ is,

$$\left.\frac{d\phi}{d\omega}\right|_{max} = \pm\frac{\pi}{\Delta\omega_{\text{pix}}} \, , \tag{4.2}$$

where $\Delta\omega_{\text{pix}}$ is the frequency span of one pixel. As discussed in the following section, the phase profile can be best described by a Taylor series expansion (eqn. 4.5). If β_n corresponds to the nth order dispersion parameters of the phase, the maximum values that can be applied before reaching the Nyquist limit [19] can be calculated for each of the dispersion parameters individually using the generalised eqn. 4.3 where $\Delta\lambda_{pix}$ is the wavelength span of one pixel [20].

$$\beta_{n_{max}} = \pm\frac{(n-1)!}{2}\frac{\lambda_0^{2n}}{(N_{pix}\pi)^{n-1}(c\Delta\lambda)^n} \, . \tag{4.3}$$

For the pulse shaper described in this chapter, the maximum $\beta_{2_{max}}$, $\beta_{3_{max}}$ and $\beta_{4_{max}}$ are calculated to be 2.80 ps^2/rad, 0.66 ps^3/rad^2, and 0.233 ps^4/rad^3 respectively.

The pulse shaper performance was tested using the grating compressor contributions as the reference. This was done by altering the grating separation in the compressor by known distances and then the phase was applied using the LC-SLM. The expected values of the dispersion coefficients were calculated for a set values provided by the

gratings manufacturer for the grating compressor design. The data was collected for high repetition rate 80 MHz and low energy ~1 nJ. The position of the grating giving the best pulse shape without any phase applied was taken as the reference compressor roof mirror position or 0 mm position. The grating was then moved in both the directions from this reference point. The second order phase parameters obtained from the shaper for these experiments agreed well with the expected change in dispersion from the compressor.

4.2.1 Learning Algorithm

A learning algorithm is used to optimise the output of the system by controlling the LC-SLM. This output is then fed back to the computer controlled algorithm completing the learning loop. There are many possible control algorithms for such processes, perhaps one of the most commonly used is the simulated annealing (SA) algorithm which is briefly discussed in this section. This algorithm is designed to find the global optimum in what may be a complicated search space with many local non-optimum minima. Other algorithms used to obtain experimental results are described in detail in the relevant chapters.

The SA is based on a principle analogous to the annealing of a metal [15]. When a metal is cooled slowly enough, large crystals are formed which later result in a single pure crystal without any defects after a long time of controlled cooling. This is the lowest energy state for the crystal. Inspired by the annealing process, an SA approaches the global optimisation problem like a bouncing ball amongst ranges of mountains and valleys. With this algorithm in the learning loop, we hope to reach the lowest valley. Initially the ball has higher energy (high temperature) and is capable of reaching over all the mountains and access all the valleys. As the 'temperature' is lowered, the ball gets trapped in a local range. It then randomly records the depth of the local valleys. It compares each value to the last saved lowest valley. If it is lower, it records the new lowest valley, and if it is higher, it either accepts it as the new 'lowest' valley or moves on to assess the next one. The SA results in convergence towards the global minimum solution.

In our set up, phase is applied to each pixel of the SLM to give the desired phase shaping result. This applied phase profile of the SLM can be efficiently represented using a Taylor series expansion [4],

$$
\begin{aligned}
\phi(\omega) &= \phi(\omega_0) + \frac{d\phi}{d\omega}\Big|_{\omega_0} (\omega - \omega_0) + \frac{1}{2!}\frac{d^2\phi}{d\omega^2}\Big|_{\omega_0} (\omega - \omega_0)^2 \\
&\quad + \frac{1}{3!}\frac{d^3\phi}{d\omega^3}\Big|_{\omega_0} (\omega - \omega_0)^3 + \frac{1}{4!}\frac{d^4\phi}{d\omega^4}\Big|_{\omega_0} (\omega - \omega_0)^4 + \ldots
\end{aligned}
\tag{4.4}
$$

$$
= \beta_0 + \beta_1(\omega - \omega_0) + \beta_2\frac{(\omega - \omega_0)^2}{2!} + \beta_3\frac{(\omega - \omega_0)^3}{3!} + \beta_4\frac{(\omega - \omega_0)^4}{4!} + \ldots,
\tag{4.5}
$$

where ϕ is the phase applied, ω is the frequency, corresponding to a certain distance along the pixels, relative to the centre frequency ω_0. The algorithm is set to find the optimum value for each of the first six coefficients of the equation 4.5. The first term is a constant offset used as a point of reference. The second term describes the overall group delay of the pulse. The third term is the quadratic phase corresponding to linear chirp and higher order terms are the higher order phase terms resulting in pulse distortion. Although the first two terms do not alter the pulse shape, they are used to reset the offset from the reference point. Thus the algorithm is used to optimise a low number of coefficients rather than each individual pixel, hugely simplifying and therefore speeding up the process.

The adaptive control loop in the system uses a GSA algorithm [17] for optimisation. Based on the principle described earlier, with initial high 'temperature' value the algorithm samples the entire parameter space to avoid being trapped in local minima, and then it narrows the search space, as the 'temperature' value is gradually decreased, to efficiently find the optimum solution. The search algorithm typically ran for 150 iterations and took ~2 minutes to optimise the AC peak.

For a faster convergence, the phase was described by a Taylor series expansion. With this, the 128 pixels of the SLM could be addressed with only few parameters. It was convenient to address only a few parameters due to the speed and time related to addressing

all pixels. The applied phase, $\Phi_{SLM}(\Omega)$, was described as:

$$\Phi_{SLM}(\Omega) = \beta_0 + \beta_1\Omega + \beta_2\frac{\Omega^2}{2!} + \beta_3\frac{\Omega^3}{3!} + \beta_4\frac{\Omega^4}{4!} + \dots , \qquad (4.6)$$

where Ω is the frequency detuning and β_n is the nth order dispersion. Results for the dielectric grating stretcher system were best obtained by modifying the $\beta_2...\beta_6$, whereas for the fibre stretcher system, it was found that optimisation of β_1 ... β_4 dispersion terms was sufficient.
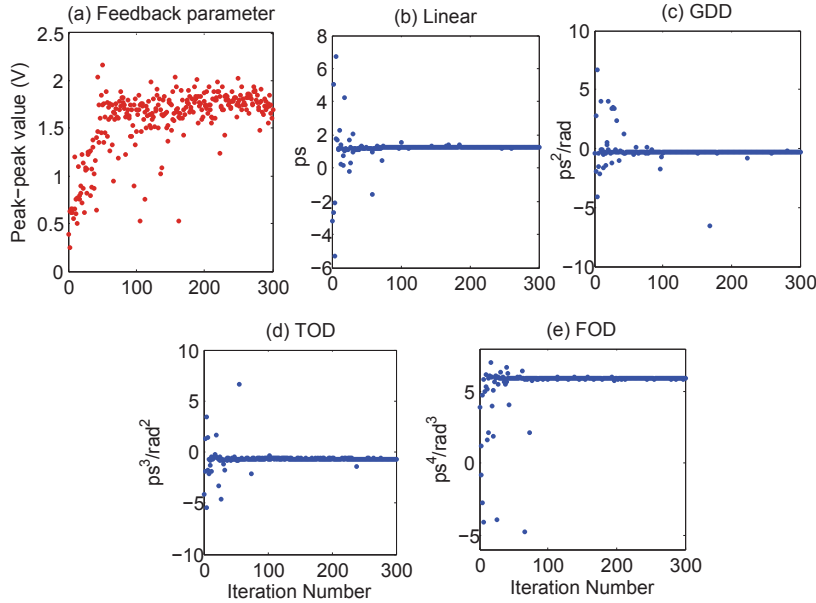
FIGURE 4.3: Convergence of feedback parameters with the number of iterations.(GDD: Group delay dispersion, TOD: Third order dispersion, FOD: Fourth order dispersion.)

For an added understanding of the working of the GSA algorithm, the convergence of the different parameters of the algorithm to the optimum solution were noted. This is highlighted in figure 4.3.

The feedback parameter is related to the peak-to-peak (difference between the maximum and minimum value) voltage level of the autocorrelation. This indicates the variation of the optimisation terms over one complete run of the algorithm. The data plotted here is the peak to peak value minus the base voltage value (constant for one run). The typical trends of convergence for the first four feedback parameters are also shown in figure 4.3.

4.3   Results

4.3.1   Dielectric Grating Stretcher

In the first set of experiments, with the bulk grating pair stretcher in the system, the pulse energy was varied from $13\,\mu$J to $100\,\mu$J (measured after the compressor). In this set-up, the second and third order dispersion from the stretcher is well-matched and of opposite sign to that of the compressor. This resulted in high-quality recompressed pulses at low energy, as shown in the autocorrelation trace (green line) in figure 4.4(a). The relative and normalised autocorrelations for other energies are also illustrated in figure 4.4 and figure 4.5 respectively. We see that the $65\,\mu$J pulses without shaping are severely distorted with an estimated B-integral of 2.5π and have an increased pedestal at the wings as a result of strong SPM which could not be compensated for by the grating compressor alone (light blue line). With the phase applied using the shaper, the pedestal is greatly reduced. For these experiments, the grating separation in the compressor was adjusted to maximise the autocorrelation peak of the unshaped pulses and then held constant while the feedback loop found the optimum shaped pulse.

For the $65\,\mu$J pulses, shaping increased the autocorrelation peak by a factor of 2.9, reduced the pedestals and decreased the autocorrelation FWHM from $1.4\,$ps to $1.1\,$ps. The output spectra before and after shaping are also shown in figure 4.6 along with the phase applied. We can see that the spectral amplitude is not significantly shaped or distorted due to shaping. The spectra at low energy, and at high energy are generally of similar shape, except for the strong ripples (modulations) on the high energy results. Recent work in the T$\ddot{u}$nnermann group [21] has shown that, for CPA systems with B-integrals $> \pi$, weak side-pulses on a seed pulse will grow due to Kerr-nonlinearity causing a transfer of energy from the main pulse. The final output spectrum is then strongly modulated effecting the pulse distortions. In the case of the experiment presented in this chapter, it is believed that due to increasing SPM with increasing energy, the shaper struggled to optimise the pulses with energies greater than $65\,\mu$J as can be seen in the autocorrelation for the 100μJ pulses in figure 4.4(d), so that for higher energies sub-optimal solutions were found.
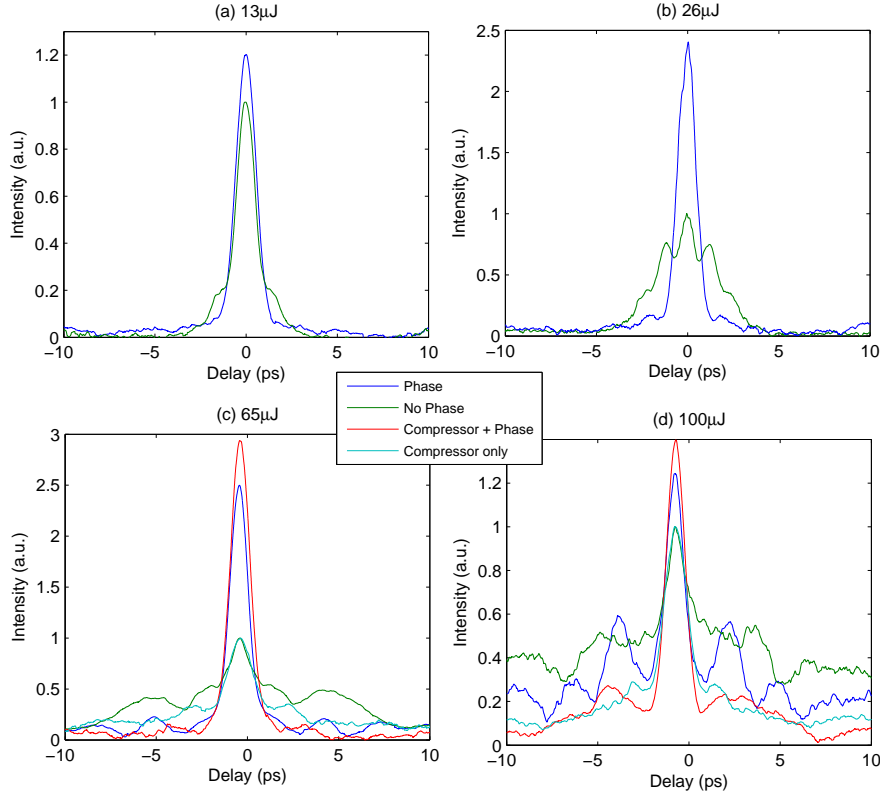
FIGURE 4.4: Relative autocorrelation traces for bulk stretcher in the system for different pulse energies. **Phase**: when phase correction was applied with the SLM; **No phase**: SLM was switched off or reset so that no phase correction was applied at 0 mm compressor position; **Compressor+Phase**: compressor is optimised first followed by phase applied; **Compressor only**: Only the compressor position was optimised and no phase correction was applied.

4.3.2 Fibre Stretcher

For the next set of experiments, the 5 km fibre stretcher replaced the bulk stretcher in the system. The third order dispersion from the fibre stretcher, adds to that of the compressor and even without any SPM this gives rise to a pedestal in the autocorrelation trace (green line) as shown in fig. 4.7(a). To add to this, strong spectral broadening is observed after the fibre stretcher due to the relatively high peak powers of the initially unstretched input pulses and the long fibre length leading to SPM. Although this could be avoided by attenuating the seed pulse energy; for high energy pulses at the output of the system, high seed pulse energy was required to minimise noise in the amplifiers. There are thus three effects that the shaper has to cope with: β_3 from the stretcher/compressor mismatch, SPM in the fibre stretcher and SPM in the amplifier stages. The experiment was therefore conducted for three cases: with low SPM in both the stretcher and the
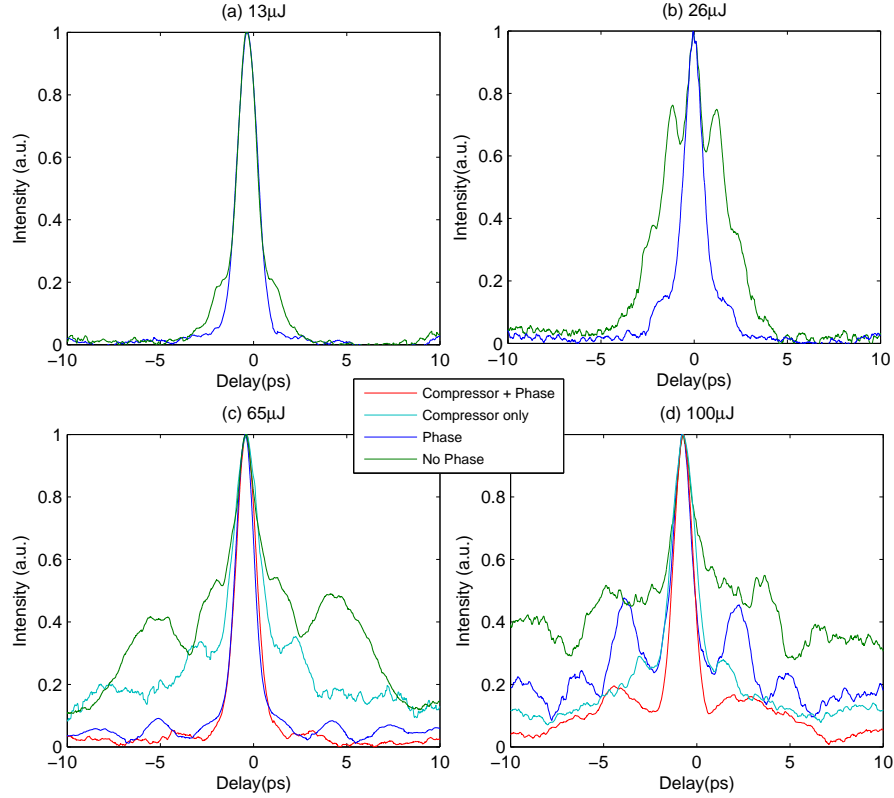
FIGURE 4.5: Normalised autocorrelations for bulk stretcher in the system for different energies. **Phase**: when phase correction was applied with the SLM; **No phase**: SLM was switched off or reset so that no phase correction was applied at $0\,\mathrm{mm}$ compressor position; **Compressor+Phase**: compressor is optimised first followed by phase applied; **Compressor only**: Only the compressor position was optimised and no phase correction was applied.

amplifier fibres; with high SPM in the stretcher fibre but low SPM in the amplifier fibres; and then for high pulse energies we operated with high SPM in both the stretcher and amplifier fibres.

In the first experiment, the autocorrelation was obtained for low SPM in both the stretcher and the fibre amplifiers. That is, with low energy, $1\,\mathrm{nJ}$ (high repetition rate) and no SPM. The grating separation in the compressor was adjusted first to optimise the pulse without any shaping. This was then fixed while the optimisation algorithm optimised the AC peak. The AC with and without applied phase along with the spectrum is indicated in figure 4.7.

In the second case, we had low energy, that is, high repetition rate but with SPM in the stretcher. The compressor grating was offset from the initial position (as in first case), by up to $\pm 2\%$. The largest improvement in the autocorrelation peak was obtained when
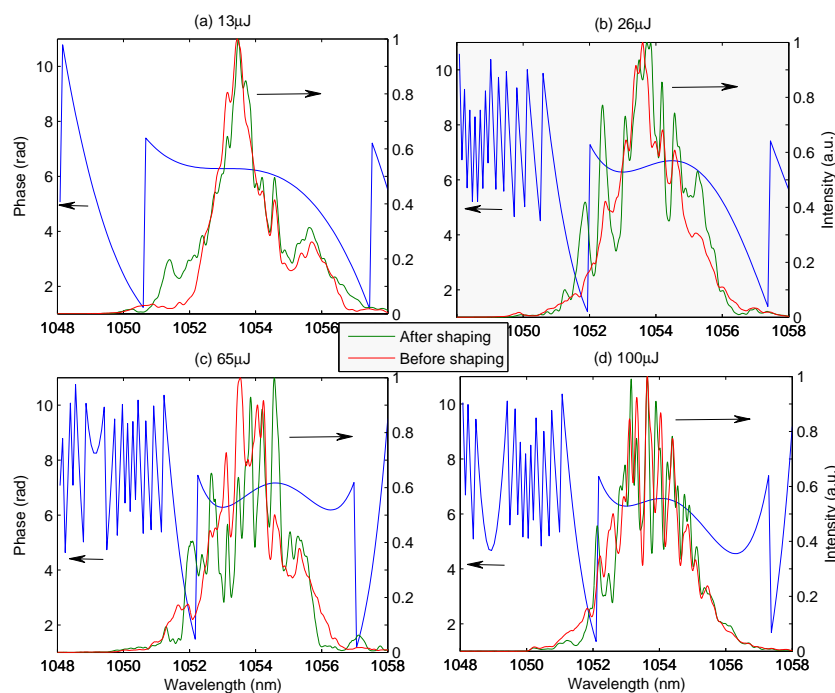
FIGURE 4.6: Output spectra and applied phase (in blue) for different input energies with bulk stretcher in the system. The spectra before (red) and after (green) shaping are shown.
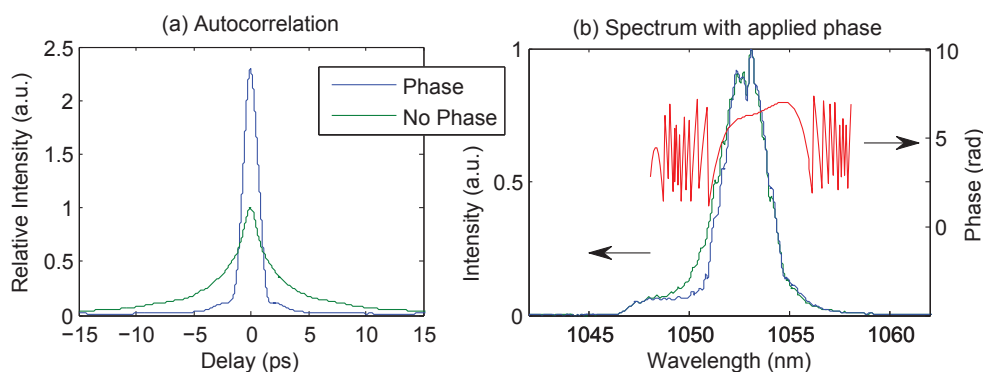

FIGURE 4.7: Autocorrelation and spectrum for low SPM and low energy in the system with no phase (green) and phase applied (blue) conditions. Applied phase is indicated in red.

the grating separation reduced by 1% (~30 mm). The AC with and without phase along with the spectrum, for this setting, is indicated in figure 4.8.

In the third case, the system was set to have high SPM in the stretcher as well as the amplifiers. The data shown in fig. 4.9 is for pulse energy of $100\,\mu$J before the compressor, that is, $65\,\mu$J after the compressor. The best pulse shape for this energy level was obtained when the grating compressor position was reduced by 0.7%(~20 mm) from the optimum for the first case. The phase applied is also shown in figure 4.9(b).
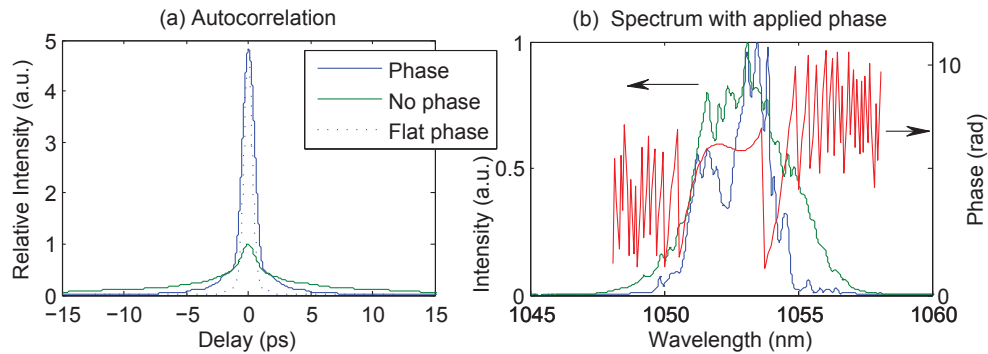
FIGURE 4.8: AC and spectrum for SPM in stretcher and low energy in the system with no phase (green) and phase applied (blue) conditions. Bandwidth limited pulse is indicated by dotted line and applied phase in red.
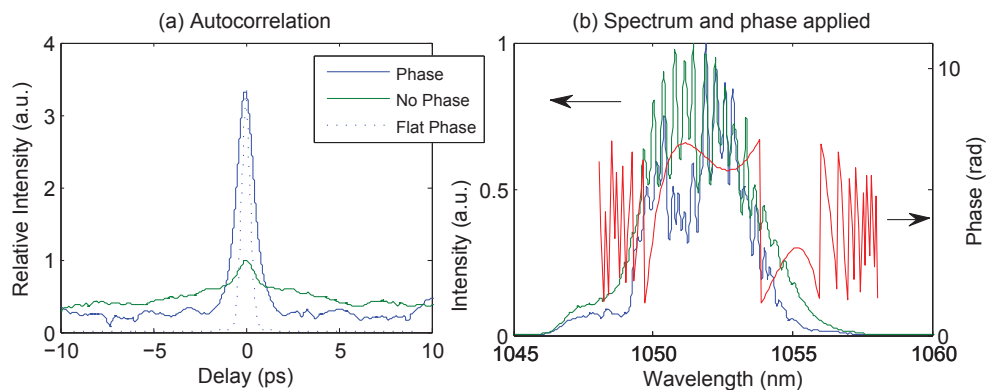

FIGURE 4.9: Autocorrelation and spectrum for high SPM at output pulse energy of $65\,\mu\text{J}$ with no phase (green) and phase applied (blue) conditions. Bandwidth limited pulse is indicated by dotted line and applied phase in red.

As we can see from the autocorrelation traces in figures 4.7, 4.8 and 4.9, phase shaping produced a significant increase in the AC peak for all the different cases discussed above. The pedestal is also significantly reduced for the low energy experiments, with or without SPM. On the other hand, the pedestal is only slightly reduced for the high energy case. Also, the Fourier transforms of the output spectra with a flat phase shows a narrower pulse compared to those obtained by shaping, even for the low energy pulse.

Evolution of the spectrum

The spectral evolution of the pulse as it propagated through the system with fibre stretcher, was also studied for different energy levels. Data sets for $65\,\mu\text{J}$ pulse (measured after compressor) are shown in figure 4.10. We can see that there is very little or no distortion after the shaper for $65\,\mu\text{J}$ pulse.
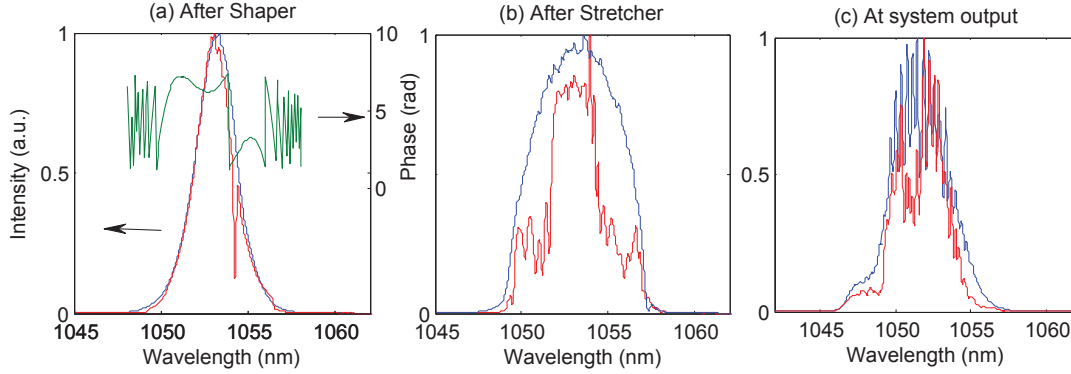
FIGURE 4.10: Spectrum for $65\,\mu$J energy pulse through the system. (Blue=unshaped, red=shaped, green=applied phase.) The dip in spectrum in fig.(a) occurs at a point of phase-wrapping.

It was observed that the spectrum is not significantly changed by preshaping when there is no SPM in the stretcher, but with SPM in the stretcher, the spectrum was modified both at the output and immediately after the fibre stretcher. With no shaping, the spectral FWHM after the stretcher is broadened by a factor of $\sim$2.5$\times$ thus increasing to $\sim$6.5 nm. In the amplifiers the spectrum acquires oscillatory structure due to SPM. The spectra of the shaped pulses are slightly modified in comparison to the unshaped spectra mainly with a reduction of the spectral amplitude at the edge of the spectrum due to phase wrapping. For the high energy ($65\,\mu$J) pulse results, the pulse energies at the input and output of the fibre stretcher were estimated to be $\sim$150 pJ and $\sim$25 pJ respectively.

4.3.3 Bulk and Fibre Stretcher Comparison

In an overview, for the same pulse energies of $65\,\mu$J, the bulk and fibre stretcher performances are compared in figure 4.11. It can be seen that for this energy level, the results for the shaper with the bulk stretcher are closer to the flat phase values but at the same time the shaping with the fibre stretcher appears to compress the pulse slightly more than the one with the grating stretcher. Adaptive shaping with the bulk stretcher in the system, however, resulted in a higher quality shaped pulse at $65\,\mu$J pulse energy.

With the fibre stretcher but with no SPM in the system, the phase shaping led to improved pulse quality but with a small pedestal and the shaped pulse is not fully compressed. The flat-phase-limit calculated from the Fourier transform of the measured
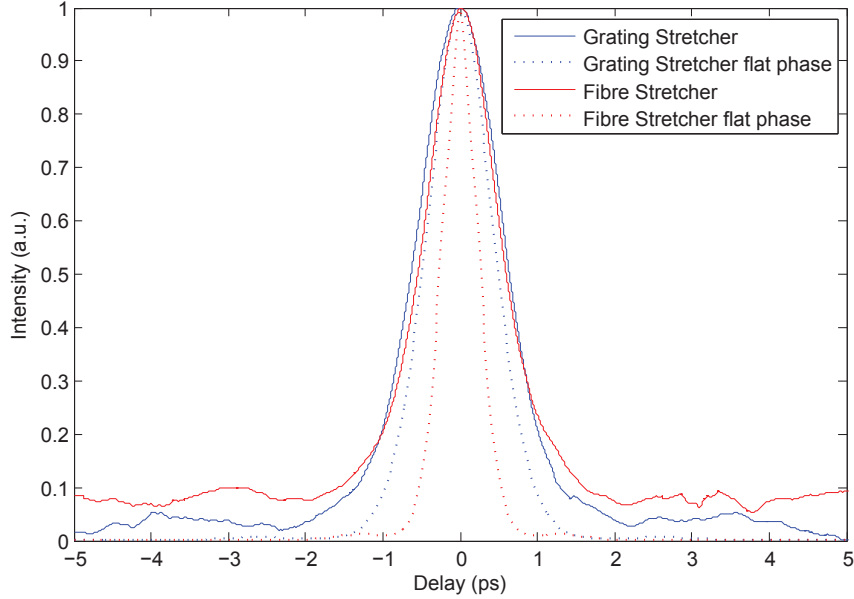
FIGURE 4.11: Bulk and fibre stretcher performance comparison for $100\,\mu$J pulse.

spectral data is almost half the width of the shaped pulse. Theoretically, at the low energies, the pulse shaper is required to compensate only for the stretcher/compressor dispersion mismatch without SPM. This should be within the shaper limits and therefore the shaper's inability to cope with it was not expected. Negligible TOD is induced for a bandwidth-limited pulse propagating in the fibre stretcher and therefore the TOD from the compressor is the dominating factor which in the case of no SPM should be within the shaper limits. For a better understanding, the TOD from the compressor is calculated to be $0.92\,\mathrm{ps}^3/\mathrm{rad}^2$ which indicates that for a folded shaper set-up, the corresponding shaper TOD is expected to be $\sim$0.46$\,\mathrm{ps}^3/\mathrm{rad}^2$. This value is within the TOD limit of $0.66\,\mathrm{ps}^3/\mathrm{rad}^2$ as expressed by eqn. 4.3 for TOD phase individually. However, for the results presented in fig. 4.7, it is found that the π per pixel limit is exceeded at the edges of the spectrum due to the combined contributions from all the dispersion terms. It therefore appears that the shaping result for the fibre stretcher set-up was not as per expectation due to the magnitude of the dispersion mismatch exceeding beyond the limits of the pulse shaper.

On the other hand, with the bulk stretcher in the set-up, experiments resulted in pulses close to the transform-limited pulses. This was due the fact that at low energy pulses, comparatively simpler phase profiles were required for optimum pulse compression. Furthermore, at higher energies, the compressor could compensate for the SPM induced

GDD making it possible to compress the pulse whilst working within the shaper limits.

The results presented thus far show that significant improvement in pulse quality can be achieved through pulse shaping but the presence of a large pedestal at high power limits the ability of the set-up to compress to the flat-phase limit even for low pulse energies with a fibre stretcher.

4.4 Conclusion

These sets of experiments have demonstrated that spectral-phase pre-shaping controlled by an adaptive feedback loop improves the pulse quality from an Yb-fibre CPA system operated with strong SPM and residual third-order dispersion from mismatched stretcher/compressor set-ups. High-quality $65\,\mu$J, $800\,$fs recompressed pulses were produced, and the autocorrelation peaks of the shaped pulses were 2.9 and 3.4 times higher compared to that of the unshaped pulses for dielectric grating pair and fibre stretcher in the system respectively.

The bulk grating pair stretcher set-up resulted in higher quality shaped pulses at $65\,\mu$J pulse energies compared to the fibre stretcher set-up. This is mainly because of dispersion mismatch between the fibre stretcher and grating compressor which required a shaper phase profile that exceeded the physical limits of the shaper set-up. Moreover, due to the pixellation of LC-SLM and phase wrapping boundaries of the shaper, only a sub-optimal solution is found within the constrained parameter space. As a result, the output pulses from the fibre stretcher set-up were not fully compressed even at comparatively low energies with negligible SPM.

However, even using the dispersion-matched bulk grating stretcher and compressor, going to pulse energies beyond $65\,\mu$J led to pulses with significant pedestals. This is believed to be due to the high nonlinearity channeling energy from the main pulse to any weak side-pulses [21] resulting in the observed highly modulated spectrum.

To the best of our knowledge, this was the first demonstration of high pulse energy CPA with adaptive pulse shaping. Further power scaling would therefore need to control the nonlinearity present in the system. The results shown have demonstrated the possibility

of power scaling ultrashort pulse fibre systems by adaptive pulse shaping. In future besides further effort to reduce nonlinearity by using greater temporal stretching or larger fibres, combined spectral amplitude and phase pre-shaping may enable improved results at even higher pulse energies, and may allow optimum operation even when there is significant SPM in the stretcher fibre. It is believed that a pixel-by-pixel optimisation algorithm may also provide better pulse compressions than with the limited number of pixels controlled using the Taylor expansion series. These possibilities are further investigated and discussed in the following chapter.

References

[1] D. Strickland and G. Mourou, "Compression of amplified chirped optical pulses," *Optics Communications* **56**(3), pp. 219–221, 1985.

[2] F. Roser, D. Schimpf, O. Schmidt, B. Ortac, K. Rademaker, J. Limpert, and A. T*ü*nnermann, "90 w average power 100 μj energy femtosecond fiber chirped-pulse amplification system," *Optics Letters* **32**(15), pp. 2230–2232, 2007.

[3] A. M. Weiner, "Femtosecond pulse shaping using spatial light modulators," *Review of Scientific Instruments* **71**(5), pp. 1929–1960, 2000.

[4] A. Efimov, M. D. Moores, B. Mei, J. L. Krause, C. W. Siders, and D. H. Reitze, "Minimization of dispersion in an ultrafast chirped pulse amplifier using adaptive learning," *Applied Physics B-Lasers and Optics* **70**, pp. S133–S141, 2000.

[5] D. Yelin, D. Meshulach, and Y. Silberberg, "Adaptive femtosecond pulse compression," *Optics Letters* **22**(23), pp. 1793–1795, 1997.

[6] A. Efimov and D. H. Reitze, "Programmable dispersion compensation and pulse shaping in a 26-fs chirped-pulse amplifier," *Optics Letters* **23**(20), pp. 1612–1614, 1998.

[7] K. Ohno, T. Tanabe, and F. Kannari, "Adaptive pulse shaping of amplified femtosecond pulse laser in phase and amplitude by directly referring to frequency resolved optical gating traces," *Ultrafast Phenomena* XIII **71**, pp. 232–234, 2003.

[8] D. N. Schimpf, J. Limpert, and A. T*ü*nnermann, "Controlling the influence of spm in fiber-based chirped-pulse amplification systems by using an actively shaped parabolic spectrum," *Optics Express* **15**(25), pp. 16945–16953, 2007.

[9] F. He, H. S. S. Hung, J. H. V. Price, N. K. Daga, N. Naz, J. Prawiharjo, D. C. Hanna, D. P. Shepherd, D. J. Richardson, J. W. Dawson, C. W. Siders, and C. P. J. Barty, "High energy femtosecond fiber chirped pulse amplification system with adaptive phase control," *Optics Express* **16**(8), pp. 5813–5821, 2008.

[10] A. Braun, S. Kane, and T. Norris, "Compensation of self-phase modulation in chirped-pulse amplification laser systems," *Optics Letters* **22**(9), pp. 615–617, 1997.

[11] M. D. Perry, T. Ditmire, and B. C. Stuart, "Self-phase modulation in chirped-pulse amplification," *Optics Letters* **19**(24), pp. 2149–2151, 1994.

[12] M. Sato, M. Suzuki, M. Shiozawa, T. Tanabe, K. Ohno, and F. Kannari, "Adaptive pulse shaping of femtosecond laser pulses in amplitude and phase through a single-mode fiber by referring to frequency-resolved optical gating patterns," *Japanese*

Journal of Applied Physics Part 1-Regular Papers Short Notes and Review Papers **41**(6A), pp. 3704–3709, 2002.

[13] T. Schreiber, D. Schimpf, D. Muller, F. Roser, J. Limpert, and A. Tünnermann, "Influence of pulse shape in self-phase-modulation-limited chirped pulse fiber amplifier systems," *Journal of the Optical Society of America B-Optical Physics* **24**, pp. 1809–1814, 2007.

[14] D. Schimpf, D. Mller, S. Hdrich, F. Roser, J. Limpert, and A. Tünnermann, "High quality fiber cpa-system at a b-integral of 16," *Conference on Lasers and Electro-Optics (Optical Society of America)* **paper CMEE6**, 2007.

[15] S. Kirkpatrick, C. D. Gelatt, and M. P. Vecchi, "Optimization by simulated annealing," *Science* **220**(4598), pp. 671–680, 1983.

[16] F. G. Omenetto, B. P. Luce, and A. J. Taylor, "Genetic algorithm pulse shaping for optimum femtosecond propagation in optical fibers," *Journal of the Optical Society of America B-Optical Physics* **16**(11), pp. 2005–2009, 1999.

[17] C. Tsallis and D. A. Stariolo, "Generalized simulated annealing," *Physica A* **233**(1-2), pp. 395–406, 1996.

[18] C. E. Shannon, "Communication in the presence of noise," *Proceedings of the IEEE* **86**, pp. 447–457, 1998.

[19] G. Stobrawa, M. Hacker, T. Feurer, D. Zeidler, M. Motzkus, and F. Reichel, "A new high-resolution femtosecond pulse shaper," *Applied Physics B: Lasers and Optics* **72**(5), pp. 627–630, 2001.

[20] H. Hung, *An Adaptive Mid-infrared Ultrashort Pulse Source for Applications in Coherent Control*. PhD thesis, University of Southampton, 2010.

[21] D. N. Schimpf, E. Seise, J. Limpert, and A. Tünnermann, "The impact of spectral modulations on the contrast of pulses of nonlinearchirped-pulse amplification systems," *Opt. Express* **16**(14), pp. 10664–10674, 2008.

Chapter 5

Adaptive amplitude and phase shaping in an ultrafast fibre laser system

5.1 Introduction

As discussed in the previous chapter, compared to the traditional bulk crystal and glass laser sources, Yb-fibre based systems can be directly diode-pumped, have high gain and suffer less from thermo-optical problems, making them attractive high power laser sources [1]. Further, coupling with CW diode pumping has allowed the realisation of compact, ultrafast laser systems with more than $100\,\mathrm{W}$ average power at various repetition rates [1, 2]. Energy levels reaching the milli-joule levels have also recently been demonstrated with the use of novel fibre designs such as the PCF [3]. However, due to long device length of up to several metres and a highly confined mode area, these devices suffer from nonlinear effects such as SPM [4]. These nonlinear effects can degrade the pulse quality, limiting the maximum peak power available from the femtosecond source. As discussed earlier, adaptive pulse shaping prior to the amplification stages has been adopted in fibre CPA systems to generate high quality pulses. Recently, amplitude only pulse shaping was demonstrated to control the nonlinear phase modulation induced by SPM at low energy [5]. However, this approach cannot compensate for higher order spectral phase due to material dispersion. Phase-only shaping in a high-energy fibre

laser system was demonstrated by our group in our previous work [6] and has already been discussed in detail in chapter 4.

In this chapter, a dual layer LC-SLM is implemented in a fibre CPA system for adaptive amplitude and phase pre-shaping, unlike in the previous chapter where only phase shaping is implemented before amplification. The dual layer LC-SLM was controlled using a differential evolution (DE) algorithm written by Jerry Prawiharjo. The fibre CPA system produced a train of pulses with an average power of 12.6 W at 50 MHz repetition rate. These were compressible to pulses of 170 fs duration.

This chapter is essentially divided into three main parts. The entire set-up is detailed in the first part of the chapter. Sections 5.2 and 5.3 describe the entire set-up which was constructed from scratch. In sec. 5.2, the fibre laser system set-up is described in detail; consisting of a self-similar oscillator (SSO), pre-amplifier stages, power amplifier and finally the compressor. The pulse shaper is then described in detail in sec. 5.3. The second part of the chapter focusses on the experimental results obtained with the system. In sec. 5.4, the experimental results for generation of high fidelity femtosecond pulses are detailed, with the results for energy-scalable femtosecond pulse generation discussed later in 6. The chapter finally concludes in the last part with a discussion in sec. 5.5.

5.2   Fibre laser system

The first component of the fibre laser system is a passively mode-locked Yb-doped fibre oscillator as the seed. The seed pulses are allowed to stretch in fibre amplifiers that follow (and not an additional stretcher) as the pulse energy is not high in this high repetition rate scheme. The oscillator is followed by a cascade of Yb-doped fibre amplifiers. A grating pair then compresses the pulses at the final stage of the system. A pulse shaper is also added in the set-up and discussed in detail in section 5.3. A schematic for the complete system is shown in fig. 5.1.
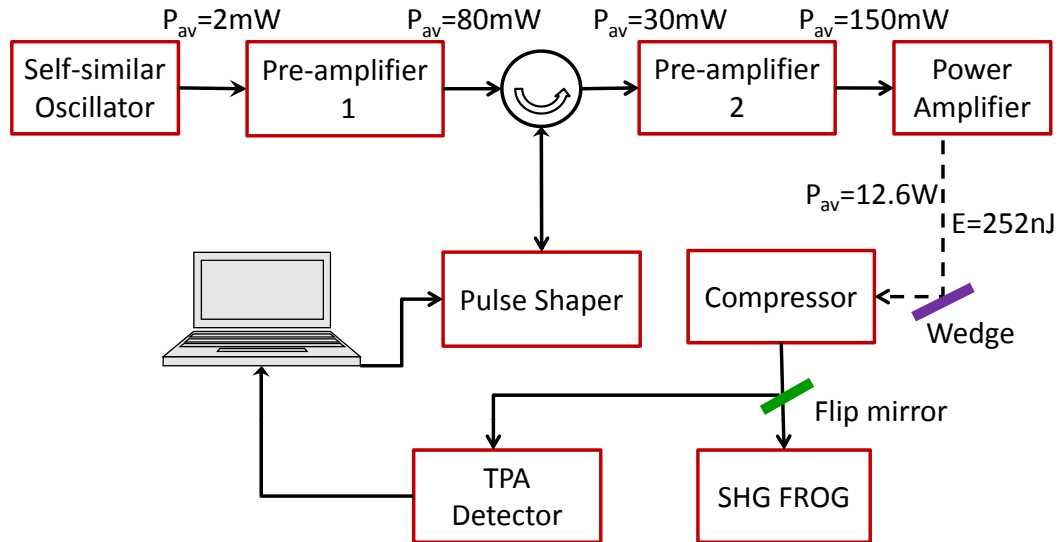
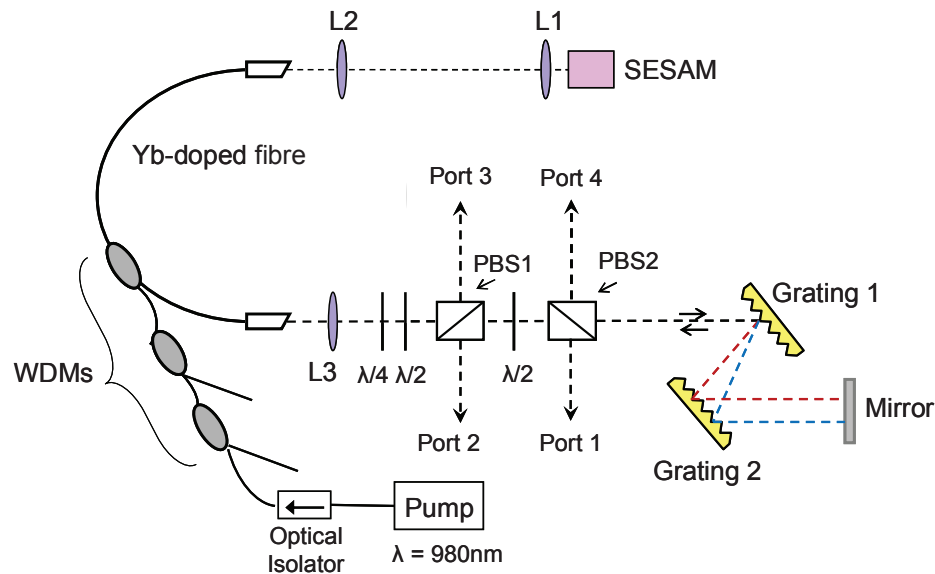FIGURE 5.1: Schematic of the system for high fidelity femtosecond pulse generation.

FIGURE 5.2: Schematic of the self-similar oscillator.

5.2.1 Self-similar oscillator

A self-similar oscillator is used as the seed laser for the CPA system described in this chapter. The design of the SSO is based on the previous work at the Optoelectronics Research Centre (ORC) [7]. In fibre-oscillators, high pulse intensities can lead to large nonlinearities due to the inherent small beam diameters of the pulse. This can lead to

wave-breaking and therefore limiting the possible maximum output energy from the set-up. A self-similar oscillator (SSO) [8] on the other hand tolerates large nonlinearities without any wave-breaking and generates pulses that propagate as similaritons. That is, their amplitude and phase may vary during propagation but their shape remains the same.

Most part of the SSO cavity comprises of a single mode fibre (SMF) which has net normal dispersion. The pulse bandwidth broadens due to a combination of nonlinear interactions as it travels through the SMF. The combination of the nonlinear phase shift and the normal dispersion of the fibre results in a nearly linear chirp imparted to the pulse. The next part of the cavity is a small segment of highly doped fibre such as the Yb-doped fibre which amplifies this broadened pulse. The length of this fibre is kept as small as possible to have negligible effects from dispersion and nonlinearity but still have enough gain so as to produce output pulses of required energy. The third part of the cavity is usually a saturable absorber which is followed by a dispersive delay line (DDL) such as a pair of gratings which as a whole has net anomalous dispersion and negligible nonlinearity. The pulses are compressed in this section of the cavity due to the linear chirp accumulated in the first part. The output of the DDL is fed back into the SMF completing the round trip. The oscillator output can be obtained from the saturable absorber section.

A schematic of the oscillator that was used for the experiments described is shown in figure 5.2. The cavity consists of a high concentration Yb-doped fibre fabricated at the ORC. The ends of the fibre are angle cleaved and polished to suppress any intra-cavity reflections. The output of a 980 nm pump diode (Bookham LC96V74-20A) is launched into the Yb-doped fibre using three 980/1060 nm wavelength division multi-plexer (WDM) couplers as shown. Two polarising beam splitter cubes (PBS1 and PBS2) along with the associated wave-plates are also included in the set-up to control the output coupling and the bias of the polarisation switch. PBS1 acts as the polarisation switch where the rejected part of the pulse appears at port 3 and is used for continuous monitoring of the oscillator spectrum with the help of an OSA. The output at port 4, as shown in figure 5.2, can also be used for monitoring the pulses from the oscillator. The

half-wave plate between PBS1 and PBS2 is used to adjust the output coupling. A suitable semiconductor saturable absorber mirror (SESAM) (BATOP SAM-1064-30-12.7s) is incorporated in the set-up for reliable self-start mode-locking. Also included in the cavity is a grating based intra-cavity dispersion compensator [9] with 600 grooves/mm gold coated gratings (Newport 53-006-520R). In figure 5.2, lenses L1 and L2 are anti-reflection (AR) coated aspheric lenses with 8 mm focal length and NA=0.5. Lens L3 is AR coated aspheric lens with focal length, f=6.24 mm and NA=0.4. All intra-cavity optics were AR coated to avoid etalon effects which could affect the self-starting operation [10]. The oscillator output could be extracted from either PBS1 or PBS2. In our set-up it is extracted at port 1 and after passing through an optical isolator (OI), it is coupled into a standard single mode (SM) fibre. The output from this fibre in turn is the input to the CPA system. The total fibre length in the cavity is $\sim$1.7 m.

For characterising the oscillator, the output power as a function of the pump power was measured at ports 1 and 2, indicated in blue and green respectively in figure 5.3. The system was unable to mode-lock for pump powers above or below the limits shown in the figure. Furthermore, autocorrelation traces along with the spectrum were measured for different values of centre-to-centre grating separation. The separation was optimised to obtain stable operation with shortest pulse durations, and this was achieved with a grating separation of 5.5 cm. The corresponding AC and spectrum traces are shown in figures 5.4 and 5.5 respectively.
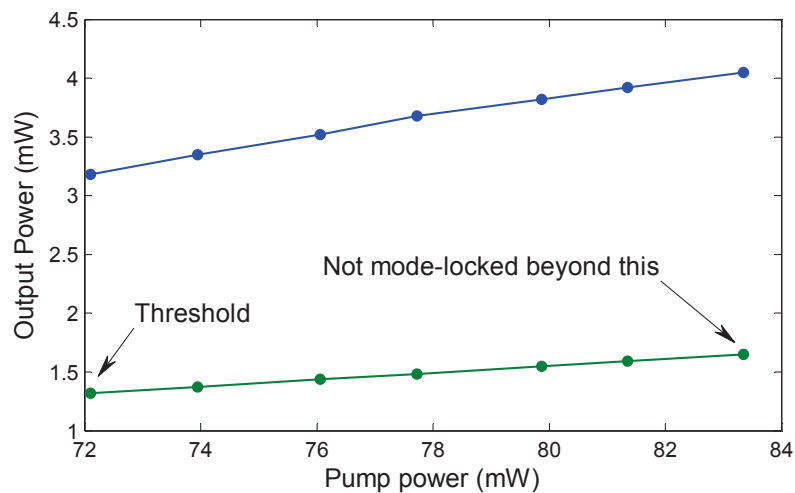

FIGURE 5.3: Output power measured at port 1 (blue) and port 2 (green), as a function of the pump power.
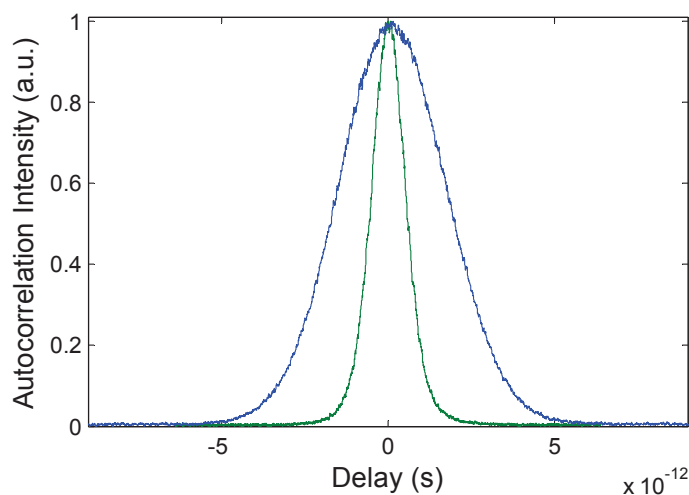
FIGURE 5.4: Autocorrelation traces for uncompressed pulses from port 1 (blue) and compressed pulses from port 2 (green), for optimised grating separation of 5.5 cm.
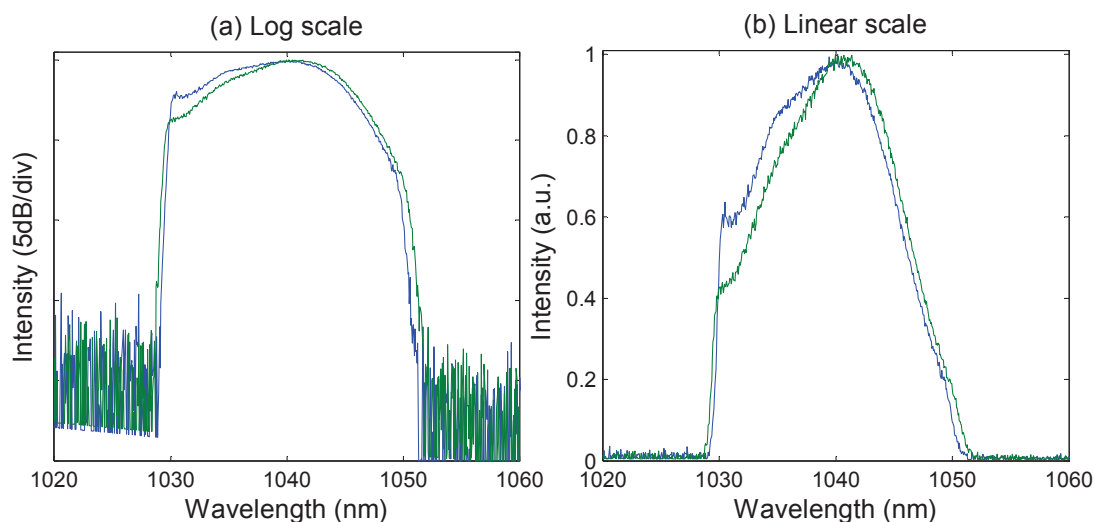

FIGURE 5.5: Measured spectra from ports 1 (blue) and 2 (green), for optimised grating separation of 5.5 cm indicated in (a) Log and (b) Linear scales.

As highlighted in figure 5.3, when pump power was increased beyond 83 mW, the pulses would stop mode-locking and this set the limit on the maximum available powers from the ports 1 and 2 with stable operation. As indicated by the autocorrelation traces in figure 5.4, the pulses from port 1 were measured to be 2.6 ps in duration (FWHM), compared to the compressed pulses from port 2 with measured pulse duration (FWHM) of 820 fs. The output spectrum from ports 1 and 2 are shown in figure 5.5. The spectrum was centred at $\lambda_0 \sim 1042$ nm and the spectral bandwidth was measured to be ~ 16 nm. At

the output, the oscillator produced an average power of 30 mW at 50 MHz repetition rate, corresponding to a pulse energy of 0.6 nJ.

It is worth noting that the output power coupling was adjusted from time-to-time to stabilise the system. The data shown in the figures are indicative of the values at the time of oscillator calibration. With time, the SESAM appeared to be damaged more quickly and thus the focal length of the lens L1 was increased from 8 mm to 11 mm to increase the beam spot size on SESAM and avoid damage.

5.2.2 Amplifiers
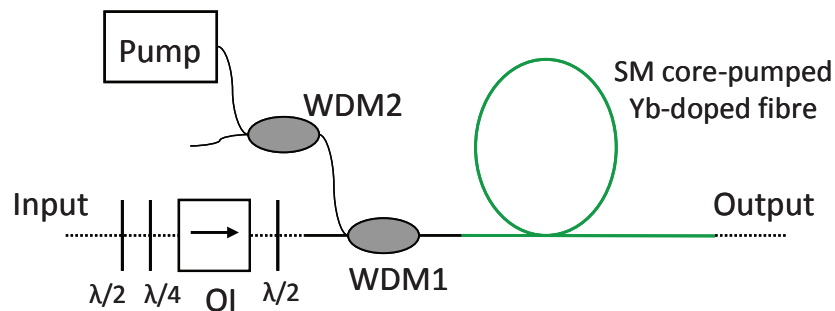
FIGURE 5.6: Schematic of the pre-amplifier stage.

Using a fibre coupler, the chirped pulses from port 1 of the SSO were used for this experiment, such that 2 mW of average power was launched into the first pre-amplifier (PA1). Both of the pre-amplifiers were pumped by SM fibre-coupled diodes at 976 nm in a co-propagating scheme, using WDMs to combine both the seed and pump into the amplifier fibres. The schematic of the pre-amplifier stage is shown in figure 5.6. Once again the fibre ends were cleaved at an angle to avoid parasitic lasing, and optical isolators were placed at appropriate places to prevent any back-propagation through the system.

A 1.7 m long SM core-pumped Yb-doped fibre was used in the first pre-amplifier to boost the average power of the seed pulses to 80 mW. The pulses were then sent into a pulse shaper, which is explained in detail in section 5.3, via a free-space optical circulator. The pulse shaper had a throughput efficiency of 40% which resulted in ∼30 mW launched into the second pre-amplifier stage, PA2. The second pre-amplifier, comprised of a 1.5 m

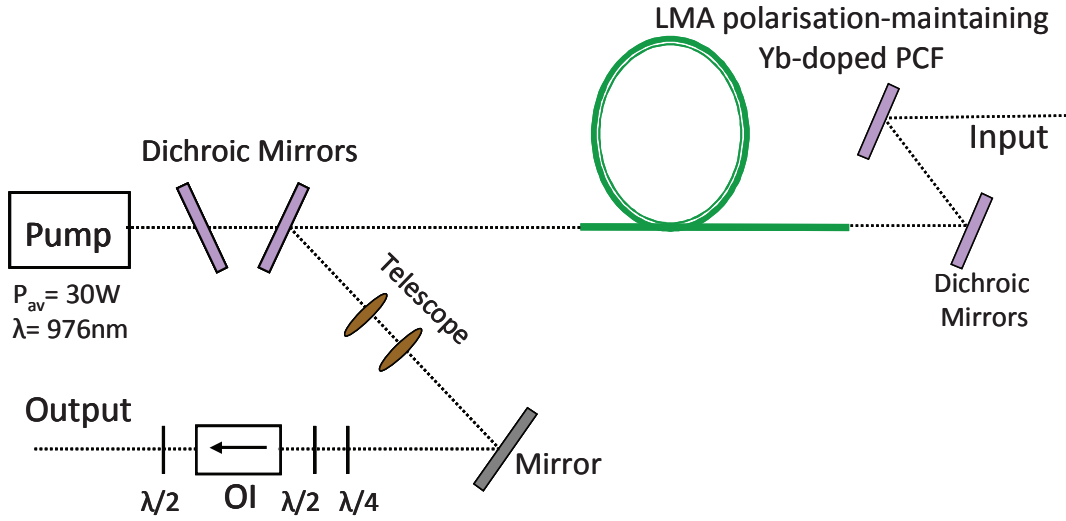long SM core-pumped Yb-doped fibre, further amplifying the pulses to give an average output power of 150 mW.

FIGURE 5.7: Schematic of the power-amplifier stage.

The pulses at the output of PA2 were then directed by dichroic mirrors (DM) (Transmission, T>95% @ 965-980 nm; reflection, R>99.5% @1028-1120 nm) before being launched into the final power amplifier (PA3). A 1.7 m long double-clad LMA polarisation-maintaining Yb-doped PCF (Crystal-Fibre DC-200/40-PZ-Yb-01), with an active core diameter of 40μm with NA=0.03 and an inner cladding diameter of 200μm and NA=0.55, was used for this final amplifier stage. A LMA PCF was used as it has a larger area implying larger saturation intensity and therefore more power in terms of the final output. Being double-clad, it allows for high power diode pumping with much less nonlinear effects compared to other fibres. The Yb-doped PCF had 10 dB/m absorption at 976 nm for light launched into the cladding, and was pumped by a multi-mode fibre-coupled pump diode generating up to 30 W power at 976 nm in a counter-propagating scheme. The input facet of the PCF was hermetically sealed (collapsing the holes), while the output facet was spliced to a very short length of coreless fibre in order to reduce the intensity at the facet. Both ends were polished at 5° angle to avoid parasitic lasing. At the output of the power amplifier, the beam was passed through a telescopic arrangement to collimate the diverging beam, and then through an optical isolator (EOT 1030-1080 nm, λ_0=1055 nm) suitable for high average powers. The telescope was chosen so that the beam diameter $w_0 \leq 8$ mm, which was the diameter of the aperture of the OI. The beam

width was chosen to be as large as possible to avoid damage of the first grating of the compressor set-up at high powers. The compressor, explained in the next section, was placed after the PA3 in the system. The train of pulses, at the output of PA3, measured after the OI, had a maximum average power of 12.6 W, corresponding to a pulse energy of 252 nJ.
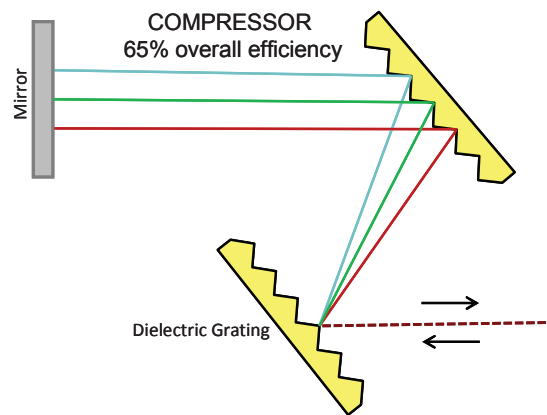
5.2.3 Compressor

FIGURE 5.8: Schematic of the grating compressor.

As explained earlier in the chapter, there is no separate stretcher component but instead the stretched pulse output of the SSO is exploited along with the small degree of stretching in the amplifier stages. This is a novel feature of this set-up allowed by high repetition rate and relatively low power operation. In this configuration, short final pulse durations can be achieved as there is no huge build-up of higher order dispersion due to a separate stretcher component.

In our set-up, the output of the power amplifier (PA3) was compressed using a pair of gold-coated 900 lines/mm holographic gratings [11]. The compressor set-up, based on the design by Treacy [11], is shown in figure 5.8. It is important to note here that the triangular grooves (indicative of mechanically ruled gratings) shown on the grating in figure 5.8, are used only for illustration. These grooves are more sinusoidal in nature for a holographic grating. For our set-up, holographic gratings were chosen over the ruled gratings as they offer the advantage that, if properly made, they can be entirely free of periodic or randomly placed groove errors found commonly in ruled gratings,

thus avoiding grating scatter. The compressor set-up had an overall efficiency of 65%. For pulse characterisation in the SHG FROG set-up, a fraction of the output pulse was taken from the Fresnel reflection of a wedge to avoid crystal damage.

5.2.4 Pulse characterisation

A home-built SHG FROG, utilising a $300\,\mu$m thick β-barium borate (BBO) crystal and a spectrometer (Ocean Optics), was employed to characterise the pulses. In addition, the pulse spectra at various points in the fibre CPA system were measured using an OSA (HP-7095-OB 600-1700nm) with a resolution as high as $0.1\,$nm.

5.3 Pulse shaper set-up

The pulse shaper was arranged in a folded 4-f configuration [12] as shown in figure 5.9. The collimated output from the first pre-amplifier with $0.9\,$mm $1/\mathrm{e}^2$ intensity half-width, was expanded by a factor of three using an anamorphic prism pair so that the diffracted beam width matched the LC window in the SLM. This beam was then sent to the shaper as the input. The beam was spectrally dispersed using a gold-coated plane-ruled $1200\,$grooves/mm grating with angle of dispersion, θ_d=38.61^o. The grating was tilted in the vertical to work under quasi-Littrow condition, meaning that the incoming light was at an angle to the plane of dispersion [13]. This configuration ensured that the tilt of the cylindrical mirror in the horizontal axis was always less than 1^0 making it our preferred configuration. The beam was focussed onto the Fourier plane using the cylindrical mirror with a focal length of $258.4\,$mm. A dual layer 128 pixel LC-SLM (CRi-SLM-128) was placed at the Fourier plane for amplitude and phase shaping the spectral components of the input pulses (see sec. 2.2.3). The pulse damage threshold was estimated to be $\simeq157\,$mW average power and $3.14\,$TW peak power for a $8\,$mm beam diameter. The input power level was always kept much lower than this limit to avoid damage. The shaper set-up efficiency was found to be $\sim40\%$. The beams into and out of the pulse shaper set-up followed identical paths and were separated by a free-space optical circulator placed at the input of the shaper set-up.
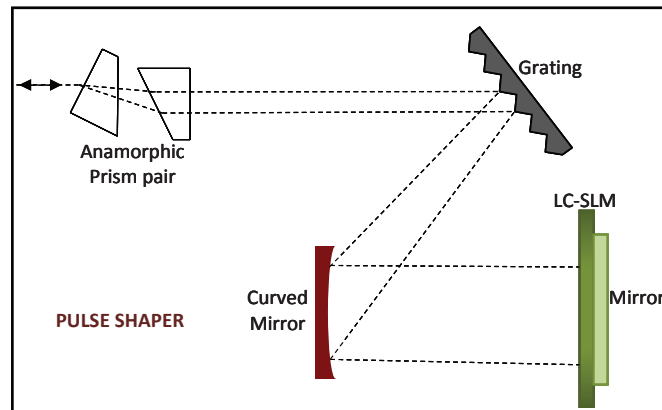
FIGURE 5.9: Schematic of the folded 4-f shaper set-up for amplitude and phase shaping.
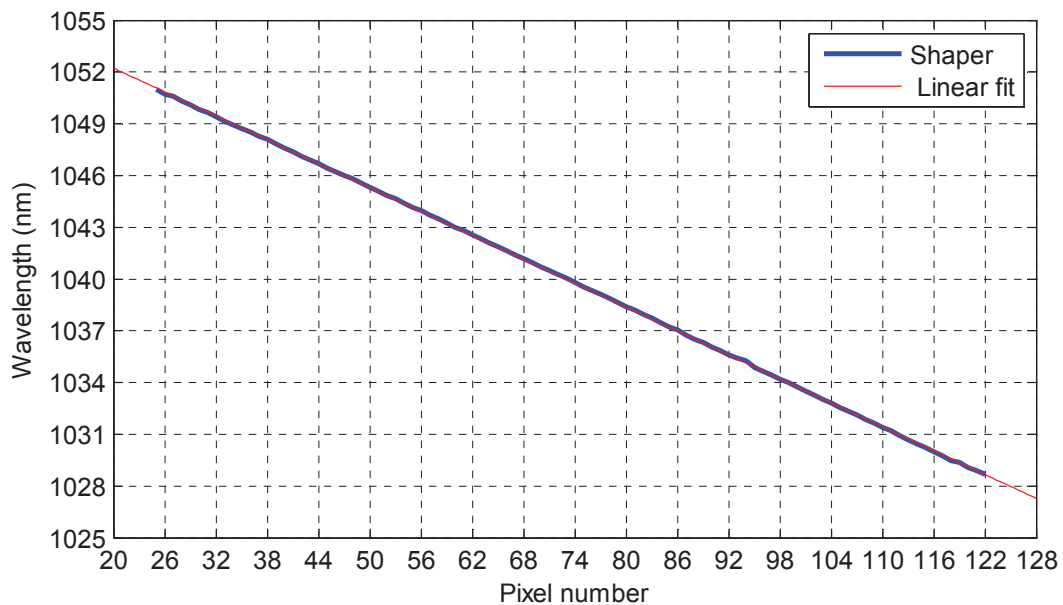
5.3.1   Pulse shaper characterisation

FIGURE 5.10: Wavelength-pixel mapping of the LC-SLM.

Both the layers of the LC-SLM had N_p=128 number of pixels each, spanning 13.1 mm physical distance. The wavelength-pixel mapping of the LC-SLM was calibrated and the result is shown in figure 5.10. The 23 nm 20 dB spectral width of the pulse occupied 97 pixels on the SLM, from the 25th to the 122nd pixel as can be seen in figure 5.10. The measured resolution from the graph thus works out to be 0.23 nm/pixel, or alternatively 2.25 nm/mm in agreement with the set spot size on the array and the measured bandwidth. The pixel array here is 5 mm high with the pixel pitch of 100$\pm$0.005 μm with 2 μm
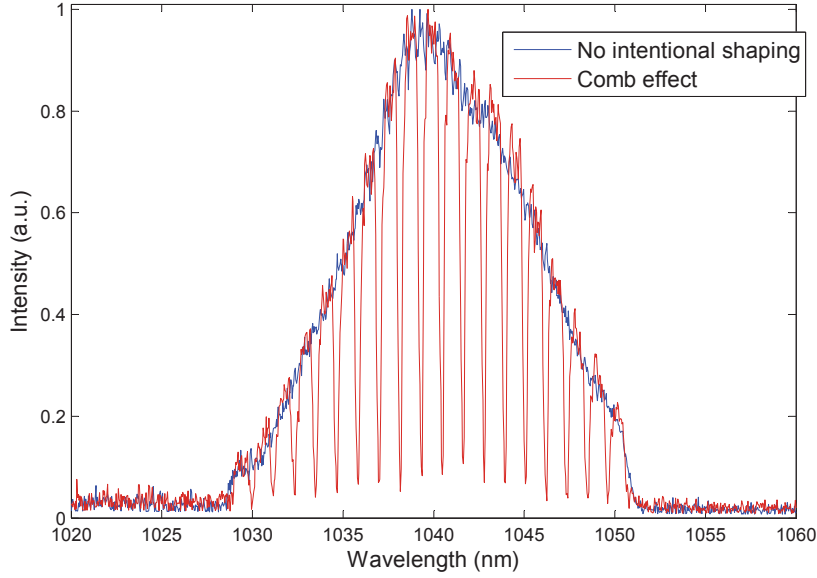
FIGURE 5.11: Linear comb effect to check the shaper alignment.

inter-pixel gap and the separation between the two masks is 1.02 mm. The time window and complexity were calculated to be 23.9 ps and η=346 respectively [sec.2.2.2] [12]. The pulse shaper was aligned to be close to zero-dispersion but no effort was made to achieve this precisely as the adaptive shaping method should be able to compensate for effects of any small offset. To optimise the position of the LC-SLM, every 10th pixel on the shaper was 'turned off' to generate a comb effect and the resultant spectrum observed on an OSA with a resolution of 0.06 nm. The SLM was then moved around until the centre of the spectrum matched with the centre pixel being controlled. An example of this is shown in figure 5.11. The electronics of the SLM provide up to V_{ref}=10 V drive voltage with 12-bit resolution, that is, 2^{12} level of digitisation. The digital drive level, D_i is thus a number from 0 to 4095 corresponding to the ith pixel element. The drive signal or voltage corresponding to that element is given by equation 5.1.

$$V_i = V_{ref} \times \frac{D_i}{4095},\qquad(5.1)$$

For SLM performance calibration, the unit was operated as an amplitude modulator as explained earlier in chapter 2 sec. 2.2.3. The transmission T is calculated by rearranging the equation ϕ=2cos$^{-1}\sqrt{T}$, where ϕ is the modulation in radians. The LC-SLM response

function was measured for the two masks, M0 and M1, independently while keeping the other mask at a constant drive level. This is illustrated in figure 5.12.
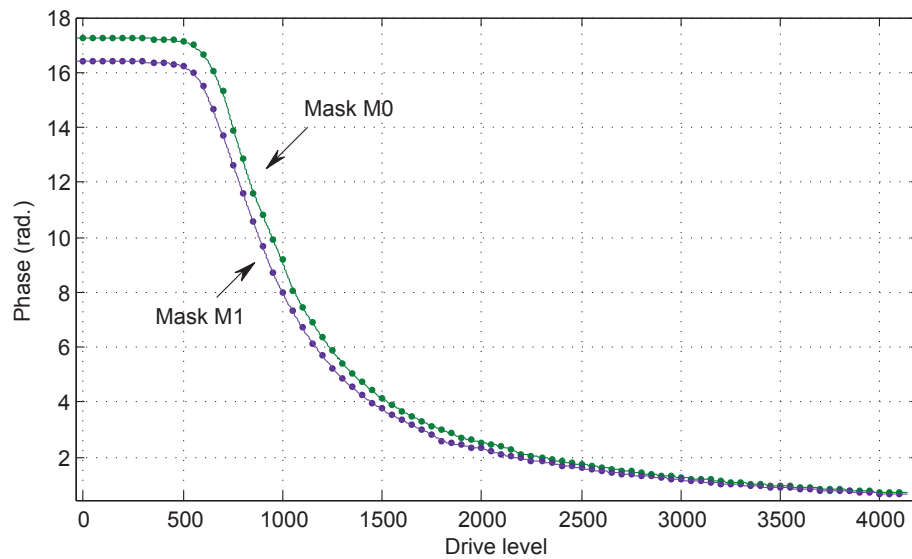

FIGURE 5.12: LC-SLM response curve. The transmission was measured at different voltage drive levels and phase calculated thereafter.

Once the SLM was calibrated, an adaptive loop was employed to optimise the TPA signal generated when the 1042 nm pulses were incident upon a GaAsP detector, using a differential evolution global optimisation algorithm. The adaptive loop and the algorithm are detailed in the next two sections.

5.3.2 Adaptive loop

As discussed in the previous chapter, direct pixel-by-pixel optimisation would give the optimum outcome for an adaptive loop optimisation process. But, this would result in a rather large search space for the global optimisation algorithm. For the experimental work in the last chapter, we used a truncated Taylor series [6]. In this experiment, we optimise only $N_s \leq N_p$ pixels of the SLM. These are then interpolated onto the N_p pixels using piece-wise cubic interpolation, as shown in figure 5.13. The N_s number of pixels controlled during an optimisation run can be gradually increased as was done for the high power results detailed in section 5.4.
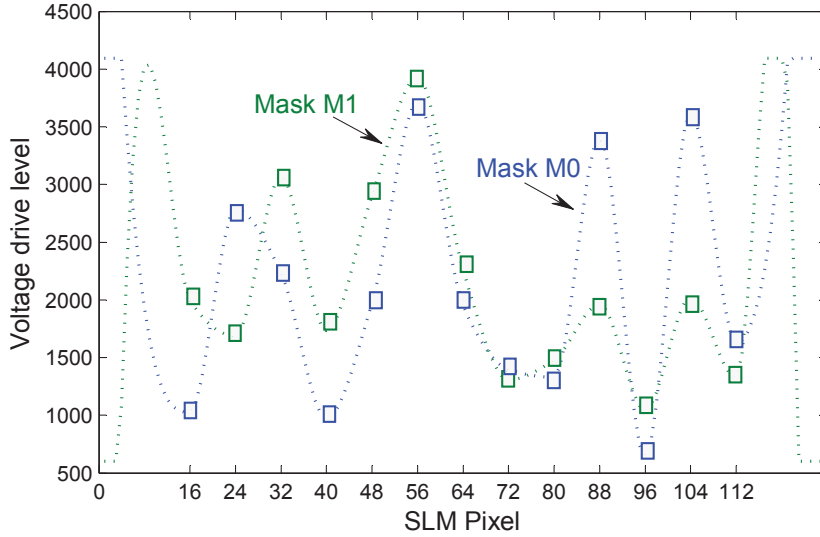
FIGURE 5.13: Illustration of applied voltage on the two masks of the LC-SLM, M0 and M1, as interpolated using the piece-wise cubic interpolation method when only every 8th pixel (indicated by empty squares) is controlled by the adaptive algorithm.

For the adaptive loop, the problem was formulated to maximise the TPA detector signal, usually measured after the compressor, as in the case of the experiments described in this chapter. The DE algorithm [14] was implemented as the global optimisation algorithm. The program was written in Matlab by Jerry Prawiharjo, which was also used to control the SLM, and to read the TPA detector signal. The DE algorithm was chosen, because it has been shown to consistently outperform simulated annealing or genetic algorithms in most cases [14].

5.3.3 Differential evolution

Differential evolution is an evolutionary algorithm (EA) and like most EAs, DE is a stochastic population-based optimisation algorithm. The general EA procedure can be schematically shown, as in figure 5.14. DE was first introduced by Storn and Price [14] and was developed to optimise real parameter, real valued functions.

PROBLEM: The general optimisation problem can be formulated as optimisation of the objective function
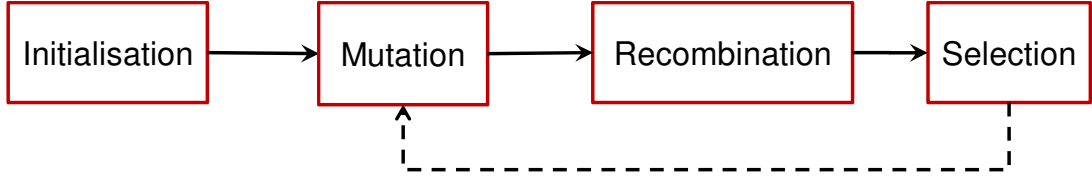
$$f : X \subseteq \mathbb{R}^D \to \mathbb{R}$$

FIGURE 5.14: Illustration of general evolutionary algorithm procedure.

where the minimisation problem is to find

$$x^* \in X \quad \text{such that} \quad f(x^*) \leq f(x) \ \forall \ x \in X$$

where

$$X \neq \emptyset$$

and

$$f(x^*) \neq -\infty$$

.

INITIALISATION: DE maintains a pair of vector population each of which contains N_d D-dimensional vectors of real valued parameters. Let the current population be defined as in equation 5.2,

$$P_{\mathbf{X},g} = (\mathbf{X}_{i,g}), \quad i = 1, \ldots, N_d; \quad g = 1, \ldots, g_{max} \tag{5.2}$$

where,

$$\mathbf{X}_{i,g} = (x_{j,i,g}), \quad j = 1, \ldots, D$$

Here, g indicates the generation to which a vector $\mathbf{X}_{i,g}$ belongs. At the start of the initialisation process, both upper and lower bounds on each parameter are specified. Let them be indicated by b_U and b_L for upper and lower bounds respectively. Once the bounds are set, a random generator, rand(0,1), assigns a value for each of the vector components given by equation 5.3 for the first generation, g=1 and for all values of j.

$$x_{j,i,g=1} = \text{rand}(0,1) \cdot (b_U - b_L) + b_L \tag{5.3}$$

MUTATION: After initialisation, DE mutates and recombines the population to get an intermediate population consisting of N_d trial vectors. As the name suggests, *differential evolution* scales the difference of two randomly chosen vectors and then adds it to a third vector to generate a trial vector. This process is illustrated in figure 5.15 and mathematically expressed in equation 5.4.
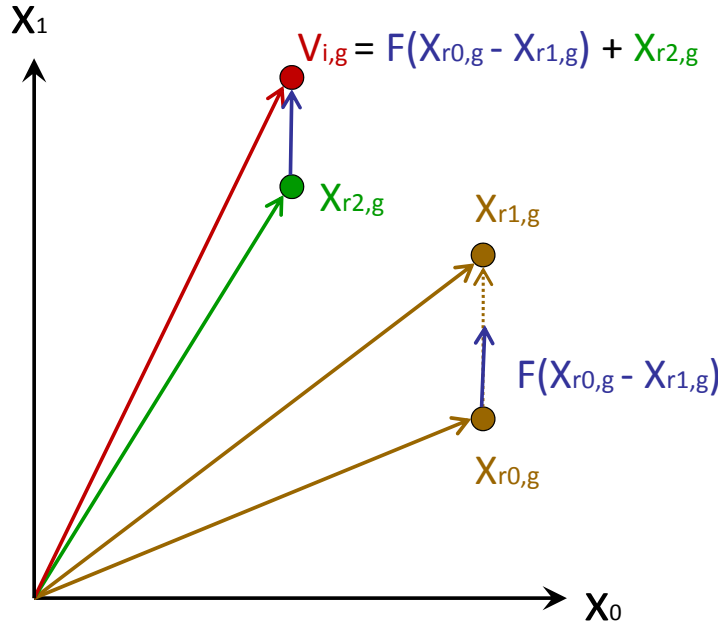

FIGURE 5.15: Illustration of the differential mutation process in a DE algorithm in two-dimensional parameter space.

$$\mathbf{V}_{i,g} = F \cdot (\mathbf{X}_{r0,g} - \mathbf{X}_{r1,g}) + \mathbf{X}_{r2,g} \tag{5.4}$$

The scale factor, $F \in (0,1)$, is a control parameter of the DE algorithm. Although there is usually no upper limit on its value, a value greater than 1 is seldom used. The randomly chosen vectors from the population, $\mathbf{X}_{r0}, \mathbf{X}_{r1}, \mathbf{X}_{r2}$ with, $r0, r1, r2 \in [1, N_d]$ are used to generate the ith mutated individual $\mathbf{V}_{i,g}$ with a condition that $r0 \neq r1 \neq r2 \neq i$.

CROSSOVER: In addition to the differential mutation, DE also applies crossover. Crossover

process generates trial vectors from the parameter values which are copied from two different vectors. That is, DE crosses each vector with a mutant vector. The crossover probability, $Cr \in [0,1]$, is another control parameter of DE and is defined by the user. The random number generator is used again for this stage and the process of crossover is summarised in the equation 5.5.

$$\mathbf{U}_{i,g} = (u_{j,i,g}) = \begin{cases} v_{j,i,g} & \text{if rand}_j(0,1) \leq \text{Cr or } j = j_{\text{rand}} \\ x_{j,i,g} & \text{otherwise.} \end{cases} \tag{5.5}$$

SELECTION: After crossover, the trial vector $\mathbf{U}_{i,g}$ replaces the target vector $\mathbf{X}_{i,g}$ in the next generation if it has a lower or equal value for the objective function compared to that of the target vector. If not, the target vector retains its place in the next generation as well (Equation 5.6). Once the new population is determined, the entire process is repeated until optimum is achieved or the preset value of number of generations, g_{max} is reached.

$$\mathbf{X}_{i,g+1} = \begin{cases} \mathbf{U}_{i,g} & \text{if } f(\mathbf{U}_{i,g}) \leq f(\mathbf{X}_{i,g}) \\ \mathbf{X}_{i,g} & \text{otherwise.} \end{cases} \tag{5.6}$$

For the specific case of this experiment, X is an integer vector, such that each of its components, $x_{j,i,g} \in [600, 4095]$ where $i = 1, \ldots, 2N_s$. X is taken as the concatenation of the pixel voltage from both the LC-SLM layers and thus there are up to $2N_s$ parameters. As explained in the paragraphs above, F, the scaling factor and Cr, the crossover rate are the control parameters of the DE algorithm. In most of the results discussed in this chapter, $F = 0.75$, $Cr = 0.5$, and $N_s = 30$ were chosen as our operating parameters. For these experiments, the optimisation took an average of 0.145 minutes per generation. Most of this time was required for updating the LC-SLM, integrating the detector signal, and on electronic communication with the instruments. The stopping time for each optimisation run was governed by the number of generations that was pre-specified for that particular run. In each optimisation, the diversity among the individuals in the population was used as a check for convergence; lesser diversity was indicative of better convergence.

Experimental results

With the basic fibre laser system in place, two main experiments were conducted. The first experiment aimed at producing high fidelity femtosecond pulses from the complete system via adaptive amplitude and phase shaping [15]. The second experiment focussed on generating energy-scalable femtosecond pulses from the set-up by adaptive pulse shaping [16]. The first experiment is described in the following paragraphs while the latter is discussed in the next chapter.

5.4 High fidelity femtosecond pulse generation

5.4.1 Experimental set-up

Using the components described in sections 5.2 and 5.3, the system shown in fig. 5.1 was constructed. As mentioned earlier, the SSO produced a train of chirped pulses with a duration of $\sim 2\,\text{ps}$ at $50\,\text{MHz}$ repetition rate, $16\,\text{nm}$ spectral FWHM at a centre wavelength of $1042\,\text{nm}$. The spectrum of the pulse had a sharp truncation at the edges with a $20\,\text{dB}$ spectral width of $23\,\text{nm}$ (as indicated in Fig. 5.16(a) in the next section). $2\,\text{mW}$ of the output power from the SSO was routed for this experiment using a fibre-coupler and launched into the first pre-amplifier, PA1 (Sec. 5.2.2). The average power was boosted up to $80\,\text{mW}$ at the output of PA1 stage and launched into the pulse shaper (Sec. 5.3). With the shaper efficiency of $40\,\%$, $30\,\text{mW}$ was launched into the second pre-amplifier, PA2 which further amplified the pulses to an average power of $150\,\text{mW}$. The output from PA2 was then routed by set of dichroic mirrors before being launched into the power amplifier stage, PA3. The beam at the output of this stage was passed through a telescopic arrangement and passed through an optical isolator. At this point, the maximum available average power was measured to be $12.6\,\text{W}$ corresponding to a pulse energy of $252\,\text{nJ}$. Finally, a fraction of this output was compressed using a grating compressor as described in sec. 5.2.3.

5.4.2 Experimental results

Figure 5.16 shows typical measured spectra at the output of the oscillator (SSO), after the first preamplifier (PA1) and the pulse shaper, and after the second pre-amplifier (PA2). It is worth noting, at this point, that the fringes that appear on the oscillator spectrum, are possibly due to the etalon effect. The fringes grow in subsequent amplifier stages, owing to SPM [17]. Although here the fringes are not a huge factor but they do become a limiting factor in high pulse energy experiments where SPM is greater (chapters 4 and 6). These fringes could only be minimised by rotating the wave-plates at different stages but could not be completely eliminated.

Unshaped pulse characterisation

To begin with, the pulses from the compressor were characterised without any intentional shaping, that is, no voltage was applied to the LC-SLM. The final amplifier, PA3, was pumped to produce a train of pulses with an average power of 2.3 W prior to the compressor. The grating pair separation in the compressor was adjusted to maximise the intensity measured by the TPA detector. This was achieved with a grating separation of 10.2 cm. The output pulses were then characterised at two power levels using the SHG FROG; at 2.3 W (low power) and at 12.6 W (high power) average powers, maintaining the grating separation.

Fig. 5.17(a) shows the square-root of the measured SHG FROG trace for low power, after interpolation onto a 128×128 Fourier grid. The detail at low intensity was not clearly visible in simple data plot and hence the square-root of the FROG trace is plotted. The retrieved and measured spectra along with the group delay, $\frac{d\phi(\omega)}{d\omega}$, are shown in fig. 5.17(b) and the retrieved temporal intensity and the chirp, $\frac{-1}{2\pi} \times \frac{d\phi}{dt}$, are shown in fig. 5.17(c). Similar set of data for high power is shown in fig. 5.18.

Fig. 5.17(c) and 5.18(c), indicate that the temporal shapes of the pulses are asymmetric with oscillation structure near the trailing edge of the pulse. This is a typical indication of the influence of accumulated, uncompensated and positive third-order dispersion (TOD) on the output of the system [18]. This is expected due to the absence of any TOD
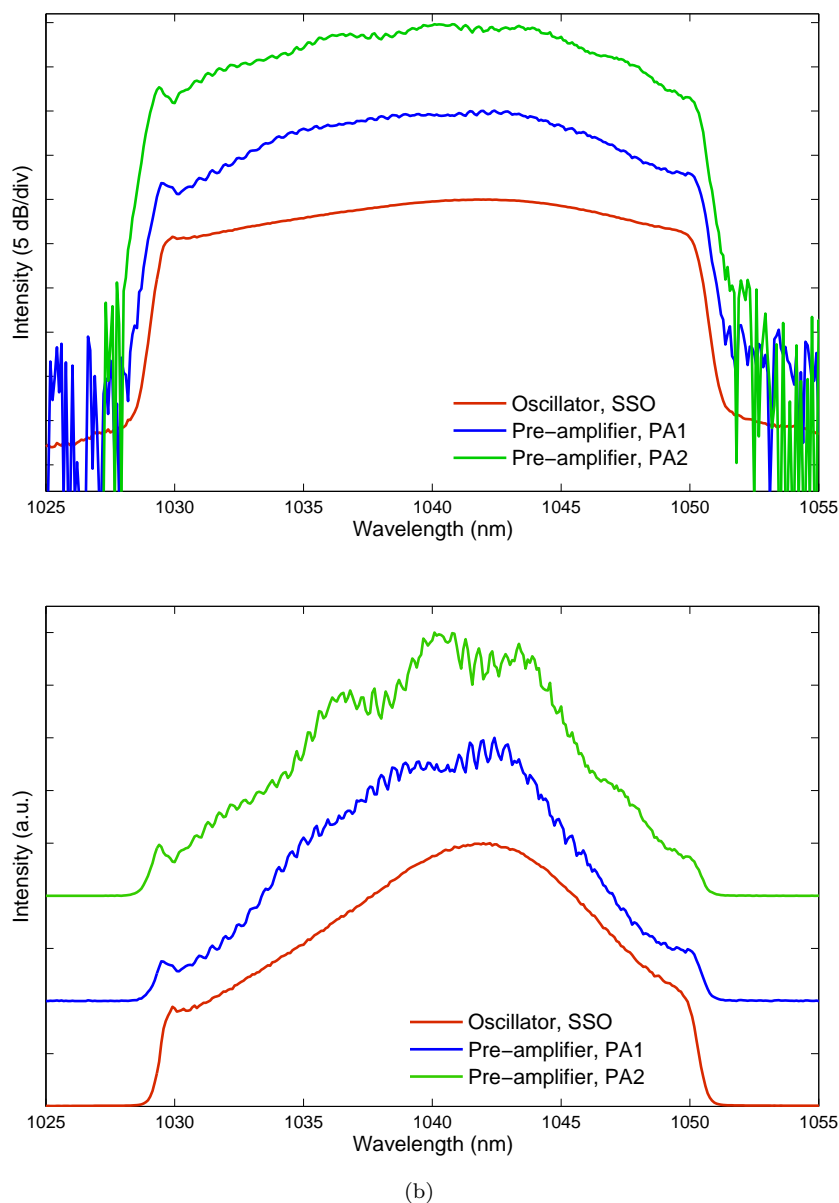
(b)

FIGURE 5.16: Normalised measured spectra at the indicated outputs in (a) logarithmic and (b) linear scale. The spectra are offset in the vertical axis for a clearer picture and understanding.

compensating element in the CPA system (the compressor is set up to compensate for the GVD). Along with this, it is worth noting that the oscillation structure at the edge of the pulses does not monotonically go to zero for the pulse at high power. In addition, there is spectral broadening observed as we increase the power (Fig. 5.17(b) and 5.18(b)) suggesting the presence of SPM. Once again, this is expected, since we do not have any stretcher in the system before the amplification stages.

The estimated upper limit of the accumulated nonlinear phase or the B-integral was

(a)

(b)   (c)
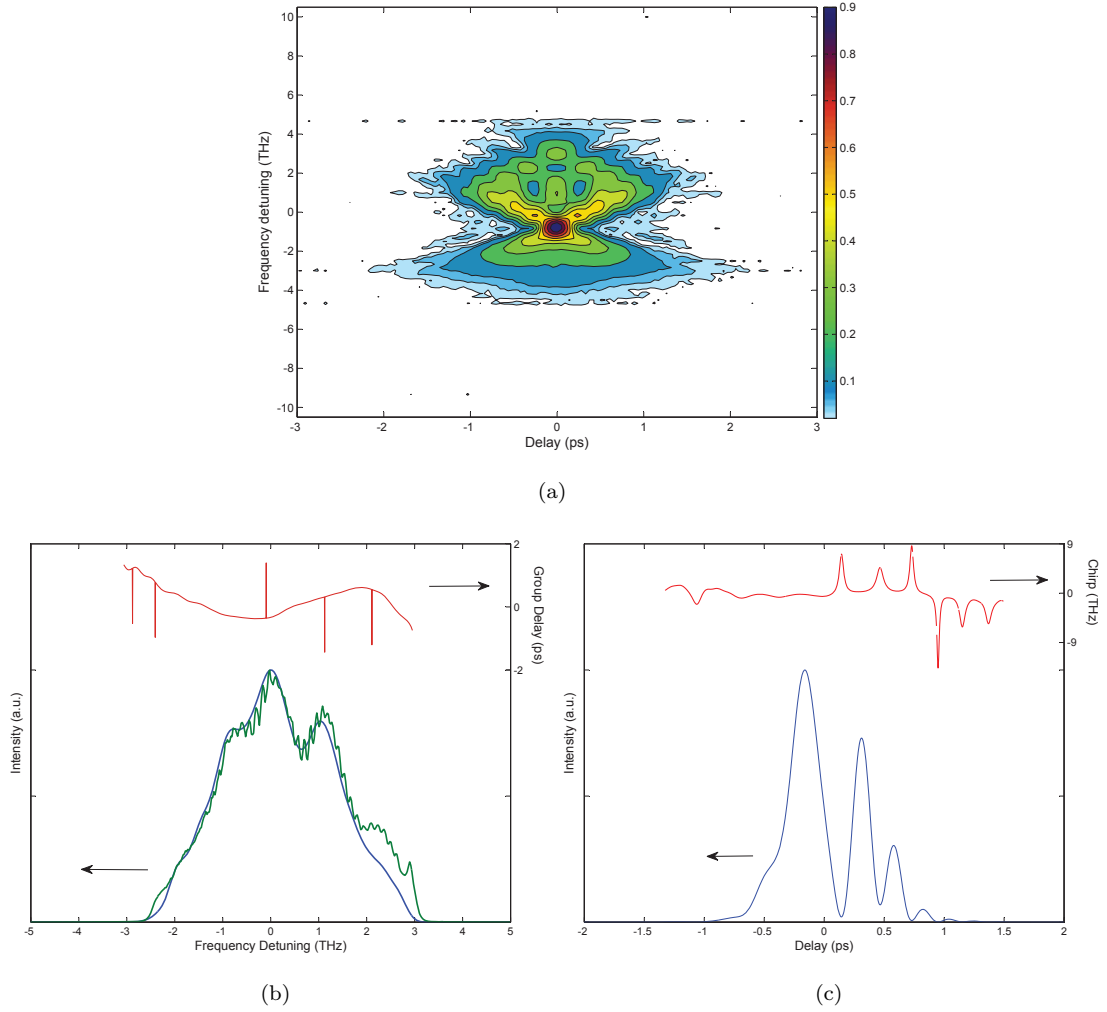
FIGURE 5.17: (a) Square-root of measured SHG FROG trace, (b) Retrieved (blue) and measured (green) spectral intensity with retrieved spectral group delay (red) and, (c) Retrieved (blue) temporal intensity with chirp (red); for unshaped pulses at 2.3 W average power.

calculated using contributions from both the passive lengths of fibre as well as the Yb-doped fibre amplifier lengths in the system. The values for 2.3 W and 12.6 W average powers were calculated to be $\Phi_{NL}^{low} = \pi$ rad and $\Phi_{NL}^{high} = 1.6\pi$ rad respectively. The contribution prior to the pulse shaper, that is, from the EOM, fibre coupler and PA1; was calculated to be 0.78π rad. For these calculations, a simplified version of the standard B-integral equation was employed, assuming exponential amplification, constant gain per unit length, and a flat spectral gain profile in the fibre amplifiers.
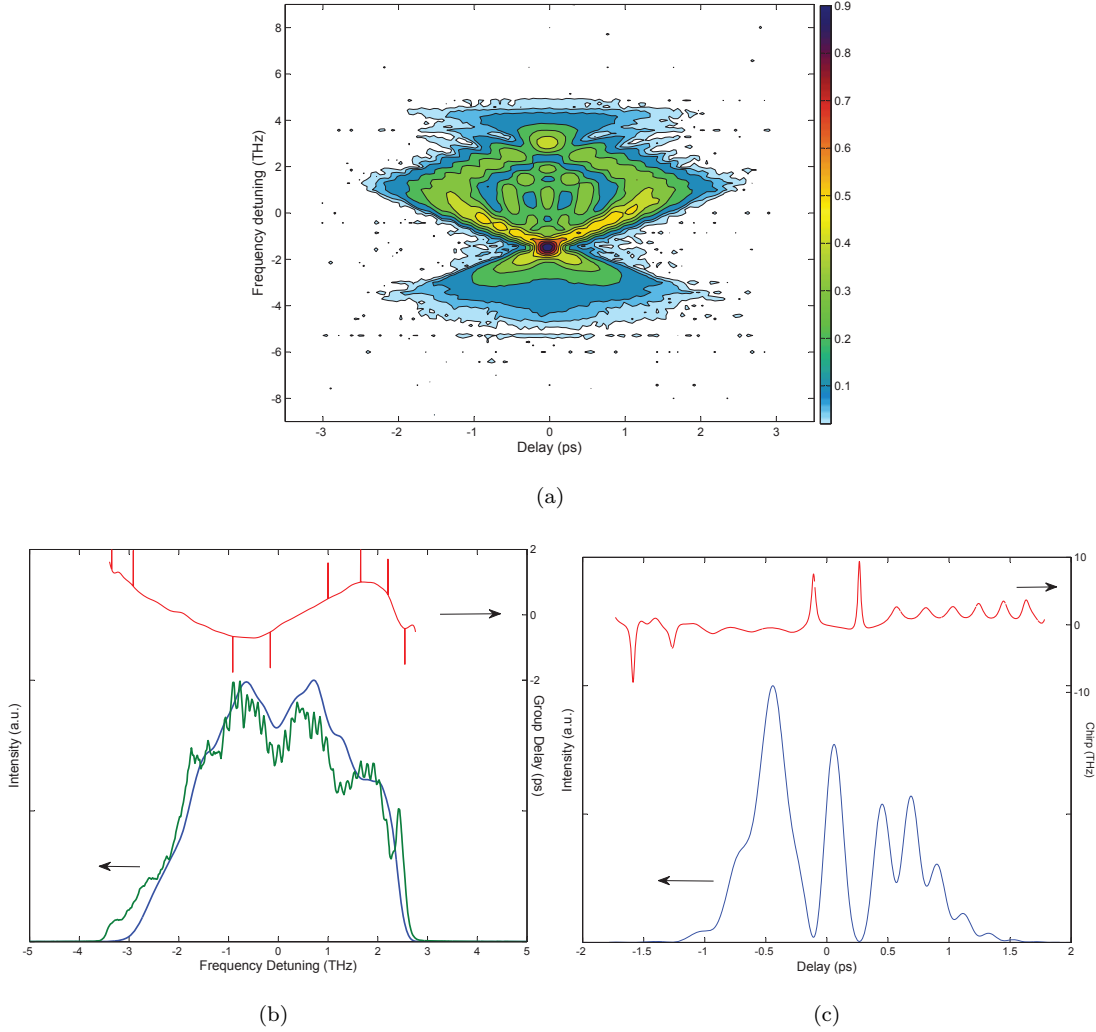
(a)

(b)

(c)

FIGURE 5.18: (a) Square-root of measured SHG FROG trace, (b) Retrieved (blue) and measured (green) spectral intensity with retrieved spectral group delay (red) and, (c) Retrieved (blue) temporal intensity with chirp (red); for unshaped pulses at 12.6 W average power.

Results for low average power pulses

Once the unshaped pulses were characterised, pulses with low average power of 2.3 W measured before the compressor, were optimised using the DE algorithm outlined in sec. 5.3. For this experiment, every 8th pixel of the SLM was controlled starting from pixel number 16 all the way up to and including pixel number 112. This pixel range fully contains the spectrum of the pulses. Pixels 16 and 112 are beyond the physical spread of the spectrum, but were controlled nonetheless to avoid overshoots at the edges of the pulse spectrum after interpolation. Thus, the phase profile was generated by interpolation between a total of $N_s = 15$ pixels that were controlled on each layer of the

SLM. The optimisation algorithm was run for 350 generations and took ~51 minutes to complete.
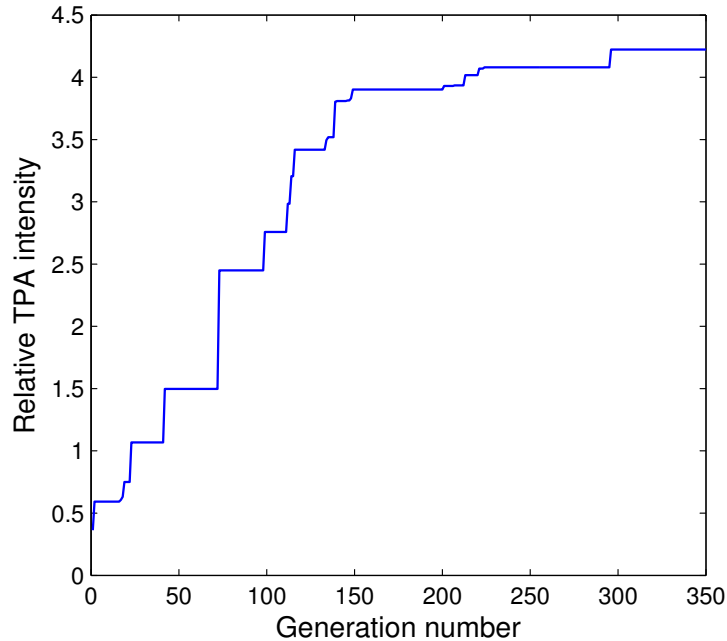

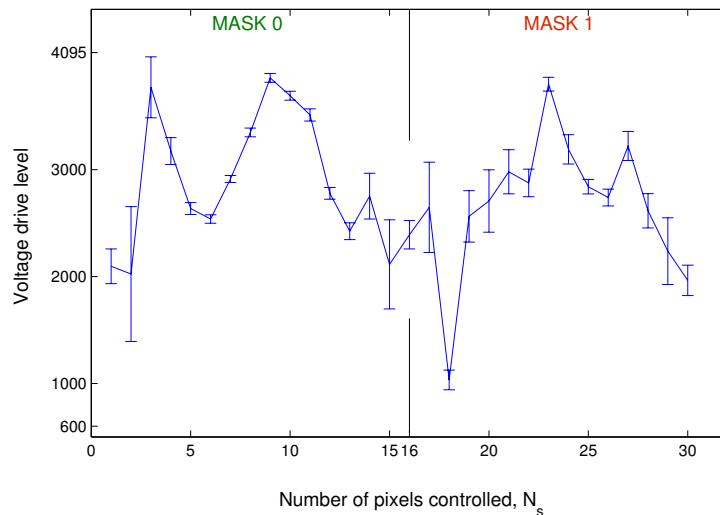FIGURE 5.19: Evolution of the TPA detector signal for low power.

FIGURE 5.20: Diversity in population for TPA optimisation at low power. The main curve represents the best individual, while the error bars indicate the diversity. The applied masks are plotted together and the pixel numbers from 1-15 represent mask, M0 and the pixels 16-30 represent mask M1 as shown.

Fig. 5.19 shows the evolution of the TPA detector signal, normalised to the case without any intentional shaping. The plotted TPA value corresponds to the best performing individual in the population at each generation. Since the algorithm was run from a random initial condition, it is possible for the best individuals at the initial stages of

the optimisation to have a lower TPA detector signal than the case without intentional shaping (corresponding to a value of 1). The TPA signal was improved by a factor of 4.2 compared to the unshaped result after 350 generations, and the algorithm had converged to a solution indicated by less diversity in the population. The total number of pixels controlled by the DE algorithm was 15 for each mask, making $N_s = 15\times2=30$. This is indicated in Fig. 5.20 on the x-axis where pixel numbers 1 to 15 correspond to the first mask, MO and 16 to 30 correspond to the second mask, M1.
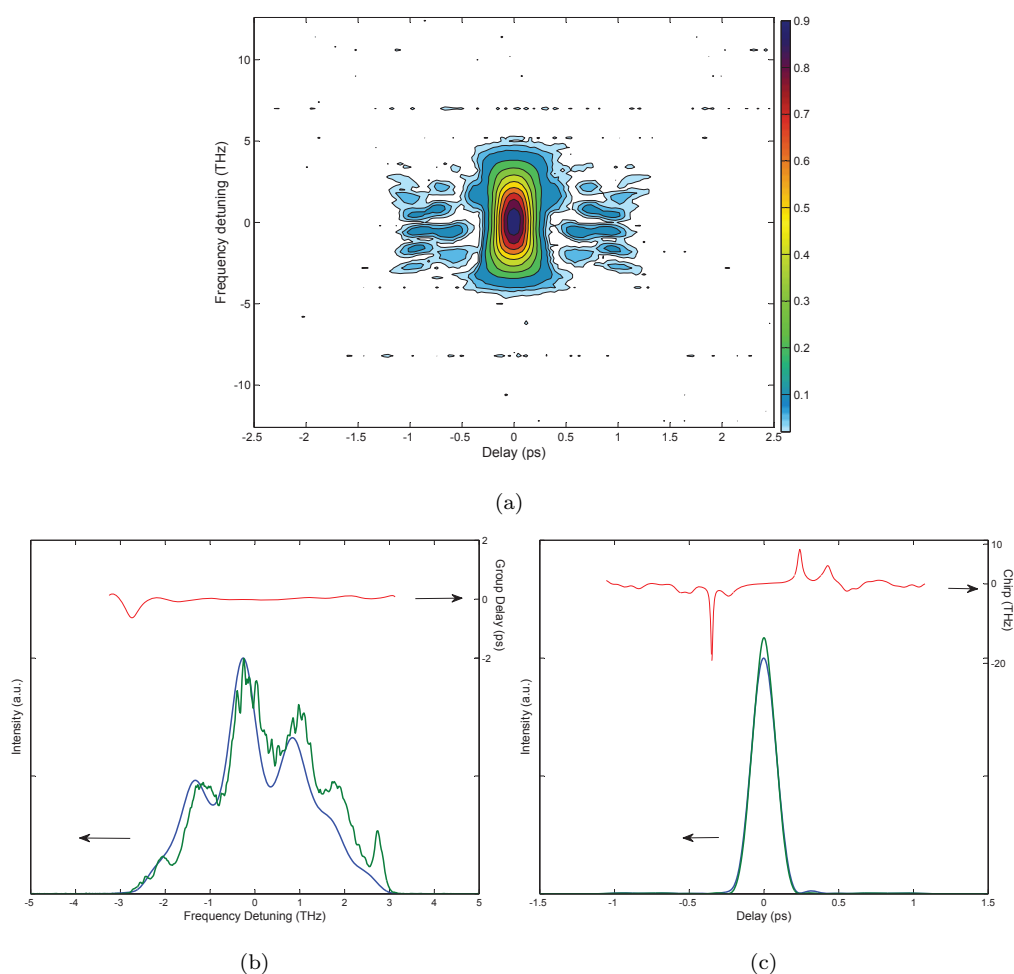

(a)

(b)

(c)

FIGURE 5.21: (a) Square-root of measured SHG FROG trace, (b) Retrieved (blue) and measured (green) spectral intensity with retrieved spectral group delay (red) and, (c) Retrieved (blue) and calculated transform-limited (green) temporal intensity with chirp (red); for shaped pulses at 2.3 W average power.

The masks corresponding to the best individual in the population were then applied to the SLM, and the pulses characterised using the home-built SHG FROG. Fig. 5.21(a) shows the square-root of the measured FROG trace, after interpolation onto a 128×128 Fourier grid. The retrieved spectral intensity and group delay along with the measured
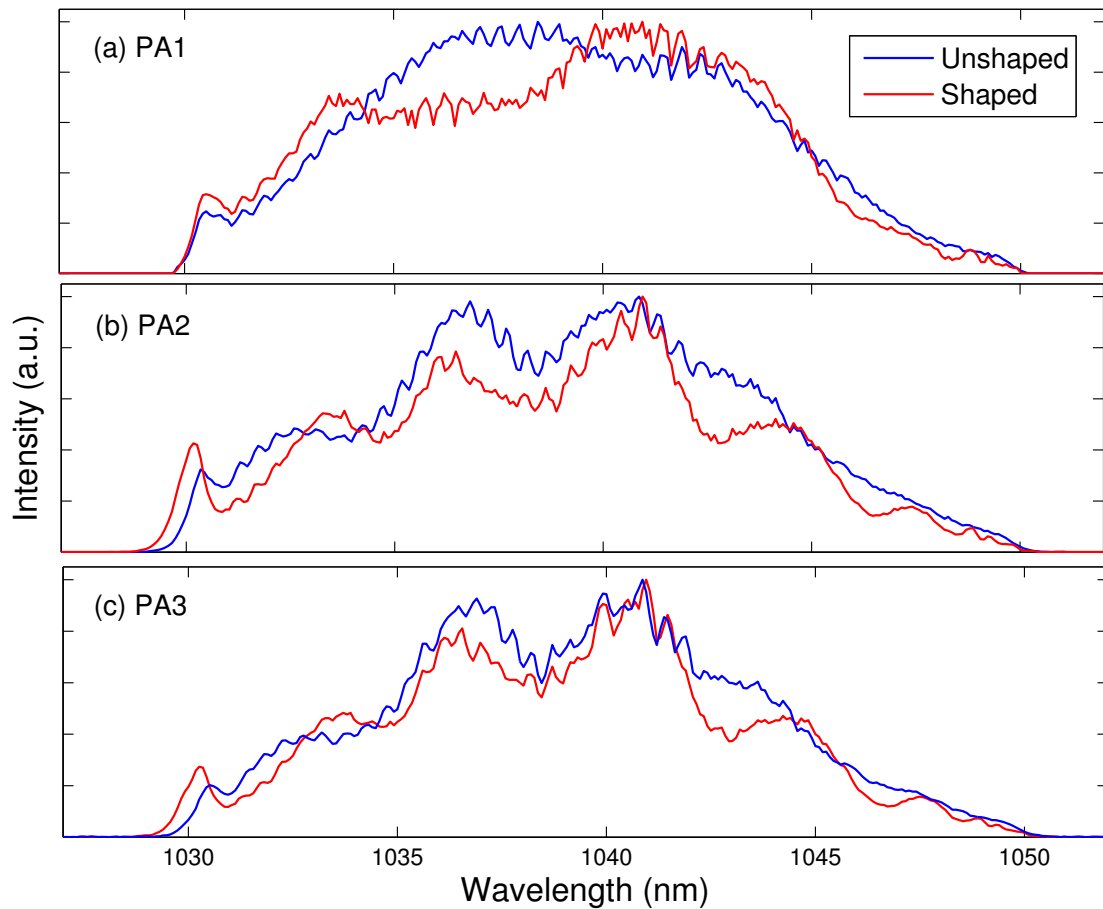
FIGURE 5.22: Measured spectra for low power, before and after optimisation, at the outputs of (a) pre-amplifier 1, PA1 (b) pre-amplifier 2, PA2 and (c) power amplifier, PA3.

spectrum are shown in Fig. 5.21(b), while the retrieved temporal intensity and chirp are shown in Fig. 5.21(c). The root-mean square (rms) retrieval error was less than 2×10^{-3}, and the temporal FWHM of the retrieved intensity profile was measured to be 195 fs. The calculated Fourier transform-limited profile is also shown in Fig. 5.21(c). The a very good agreement between the retrieved pulse profile and the calculated transform-limited profile, reconfirms the success of the optimisation algorithm. The spectrum was also measured at various points in the system and is shown in fig. 5.22, before and after optimisation.

Results for high average power pulses

The system was then operated at its highest power, generating 12.6 W average power prior to the compressor. The grating pair separation was maintained at 10.2 cm as in
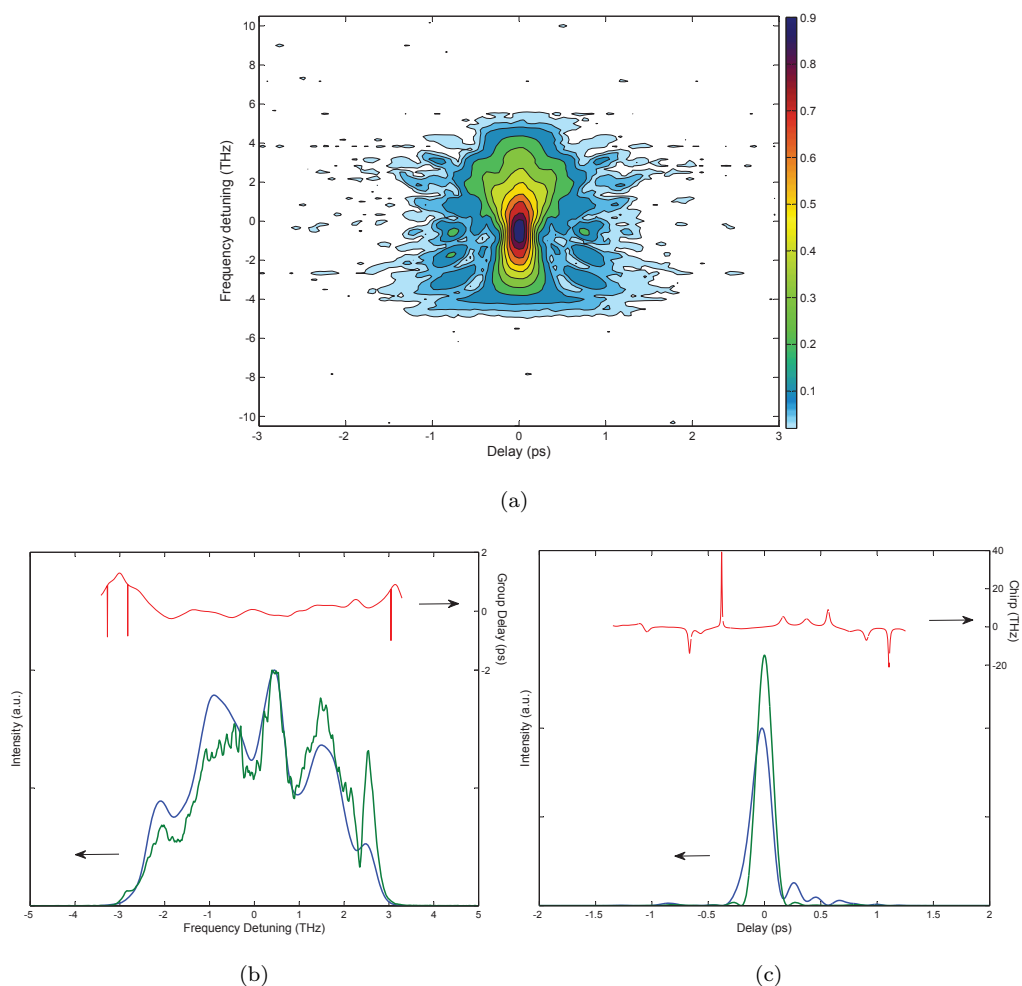
(a)

(b)

(c)

FIGURE 5.23: (a) Square-root of measured SHG FROG trace, (b) Retrieved (blue) and measured (green) spectral intensity with retrieved spectral group delay (red) and, (c) Retrieved (blue) and calculated transform-limited (green) temporal intensity with chirp (red); for shaped pulses at 12.3 W average power for the first attempt.

the previous case. The optimisation algorithm was run with the same parameters as in the previous case for 350 generations, and the pulses were then characterised. Fig. 5.23 shows the measured SHG FROG trace, and the retrieved temporal and spectral data along with the measured spectral profile. The calculated Fourier transform-limited pulse profile is also shown in fig. 5.23(c). The rms retrieval error was less than 4×10^{-3}. The temporal FWHM of the retrieved temporal profile was found to be 200 fs but there is an oscillating structure on the trailing edge of the pulses. Furthermore, the pulse has a lower intensity and a longer duration compared to the calculated Fourier transform-limited profile. Several different permutation and combinations of the optimisation parameters were employed to improve the temporal intensity profile and to reach the Fourier transform-limit. The DE algorithm was extended to 450 generations and the

control parameters of the DE algorithm (F and Cr) were varied, but this did not yield successful results. This was an indication that the inability to fully compress the pulse did not stem from the limitations of the DE algorithm itself.

Finer control over the pulse shaping was then attempted by increasing the number of pixels controlled, N_s. The number was gradually increased from control of every 8th pixel at the beginning, to every 4th pixel at generation 51, and finally to every 2nd pixel at generation 101. The pixel numbers controlled were still maintained between and including 16 to 112 of the SLM as these correspond to where the spectrum is located on the SLM. This resulted in a total of $N_s = 2\times51$ controlled pixels on the two layers of the SLM. The DE algorithm was run with this condition for 450 generations, taking $\sim$65 minutes to complete. As in the previous case, the evolution of the TPA signal was evaluated from the best individual in the population for the given generation, normalised to the case without intentional shaping. This is indicated in Fig. 5.24.
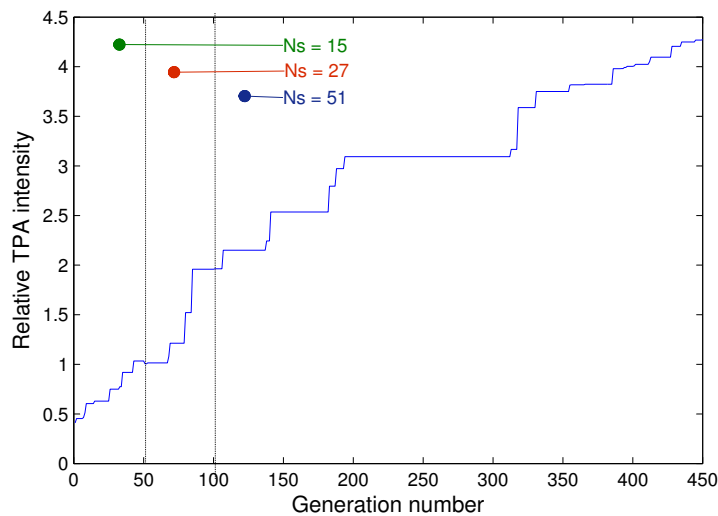

FIGURE 5.24: Evolution of the TPA detector signal for high power. Every 8th pixel was controlled in the region marked by green, every 4th in the next region marked by red label and every 2nd in the last segment marked by blue label.The number of controlled pixels indicated for the different region is for each mask.

Once again, after the optimisation, there was little diversity among the members of the population (fig. 5.25), and the TPA signal was improved by a factor of 4.3 (fig. 5.24). As in previous experiments, the pulses resulting from the optimisation were characterised by SHG FROG and the results are shown in fig. 5.26. The rms retrieval error for this set was less than 1.5×10^{-2}. The temporal FWHM of the retrieved profile was measured to be 170 fs. Although in this case, the square-root of the measured SHG FROG trace exhibits
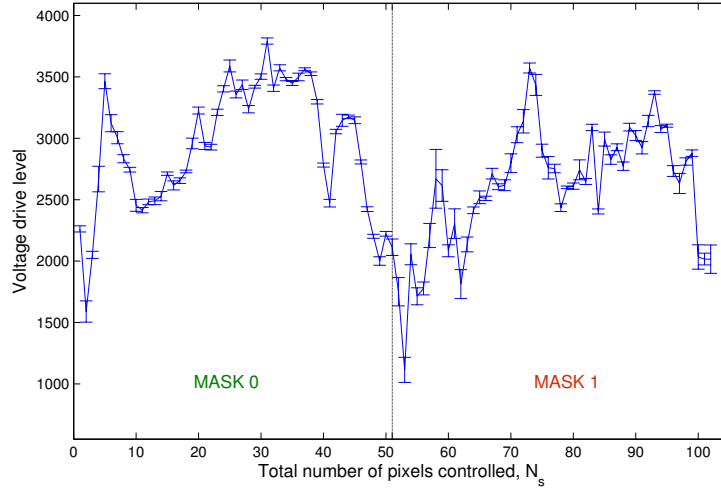
FIGURE 5.25: Diversity in population for TPA optimisation at high power. The main curve represents the best individual, while the error bars indicate the diversity. The applied masks are plotted together and the pixel numbers from 1-51 represent mask, M0 and the pixels 52-102 represent mask M1 as shown.

wings that extend up to 2 ps delay, they have intensity below 0.5%, and most of the trace mass is concentrated at the centre, unlike the case of fig. 5.23(a). The temporal profile shows a high quality pulse with the main pulse having an excellent agreement with the calculated Fourier transform-limited profile (fig. 5.26(c)). The pedestal of the retrieved temporal intensity is negligible everywhere, except for the small satellite pulse at t = -1.4 ps. The measured spectra at various points in the system are shown in fig. 5.28, before and after the optimisation. As in the lower average power case, the optimisation also yielded spectral broadening toward shorter wavelength after the second pre-amplifier and in the final spectrum. In contrast to the low average power case, the use of more control points causes the pulse spectra to exhibit more oscillations after the nonlinear propagation through the second pre-amplifier, PA2 and the final amplifier, PA3.

For better appreciation of the result obtained, the data shown in fig. 5.26(c) is plotted again with a logarithmic scale as indicated in fig. 5.27. Even at this scale, there is an excellent agreement between the retrieved and the transform-limited temporal intensity profiles of the shaped pulses.
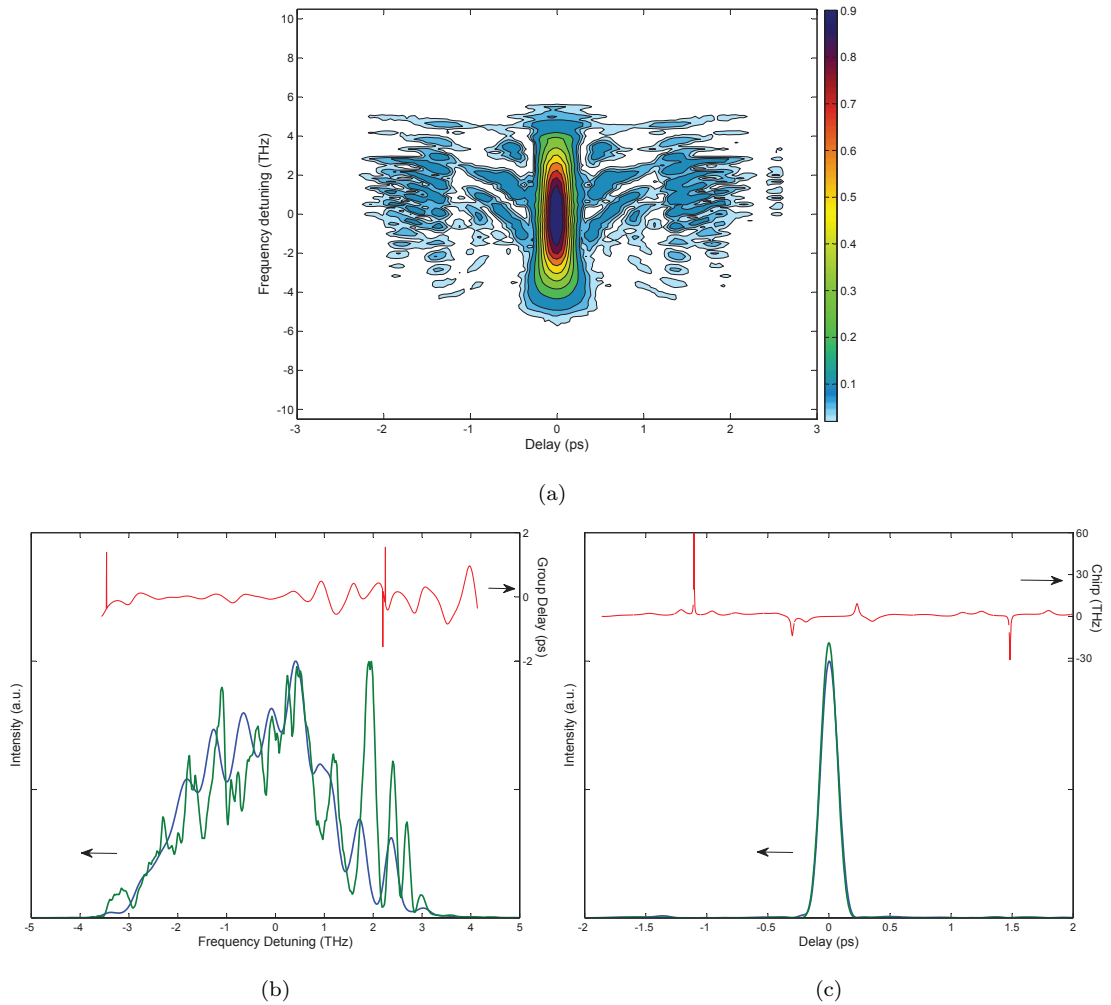
(a)

(b)

(c)

FIGURE 5.26: (a) Square-root of measured SHG FROG trace, (b) Retrieved (blue) and measured (green) spectral intensity with retrieved spectral group delay (red) and, (c) Retrieved (blue) and calculated transform-limited (green) temporal intensity with chirp (red); for shaped pulses at 12.3 W average power for the second attempt.

5.5   Discussion and conclusion

For these set of experiments, the DE algorithm started with random initial candidate solutions, but the final optimisation results obtained were highly reproducible. This was tested by running the optimisation algorithm several times under similar conditions. Furthermore, the resulting applied phase showed little dependence on the initial conditions, yielding similar compressed pulse profiles in each case. This implies that the results must be in the vicinity of the global optimum. The true global optimum could possibly be approached even closer by increasing the number of generations in each optimisation run, but this would require a rather long time and for practicality, a balance
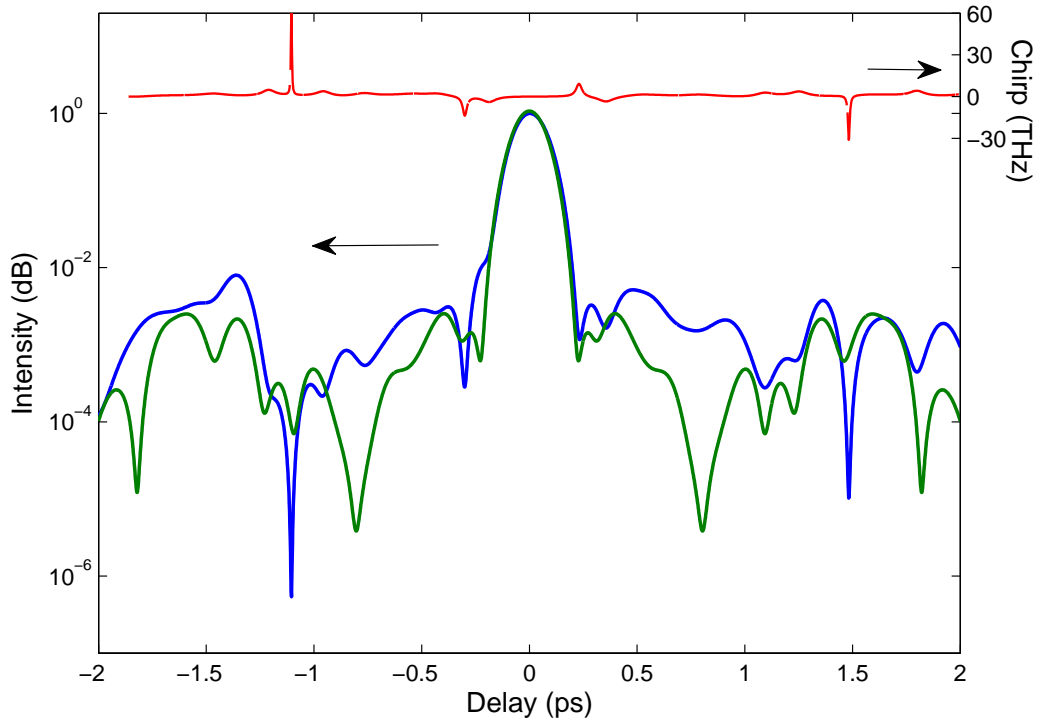
FIGURE 5.27: Retrieved (blue) and calculated transform-limited (green) temporal intensity with chirp (red) for high average power pulses in logarithmic scale.

between the number of generations with time needed was maintained. It is important to note that it is not necessary to start from random initial candidate solutions, but a previously optimised data could be used as one of the initial candidate solutions in order to reduce the optimisation time. This was avoided to retain the true sense of an adaptively shaped system. Moreover, day-to-day use was usually based on employing the adaptively found profile rather than continual optimisation due to day-to-day variation in experimental conditions.

As the pulse propagation through the three stages of amplification and through the system was nonlinear, it follows directly that the search landscape was highly nonlinear as well. However, it is evident from the optimisation results that this did not pose a problem for the DE optimisation algorithm. On the contrary, it highlights the successful performance of the DE even in such a case. In order to achieve high fidelity pulses, maximisation of a TPA detector signal or, similarly, a SHG signal, is the simplest objective function to be implemented although other more complex functions can also be optimised.
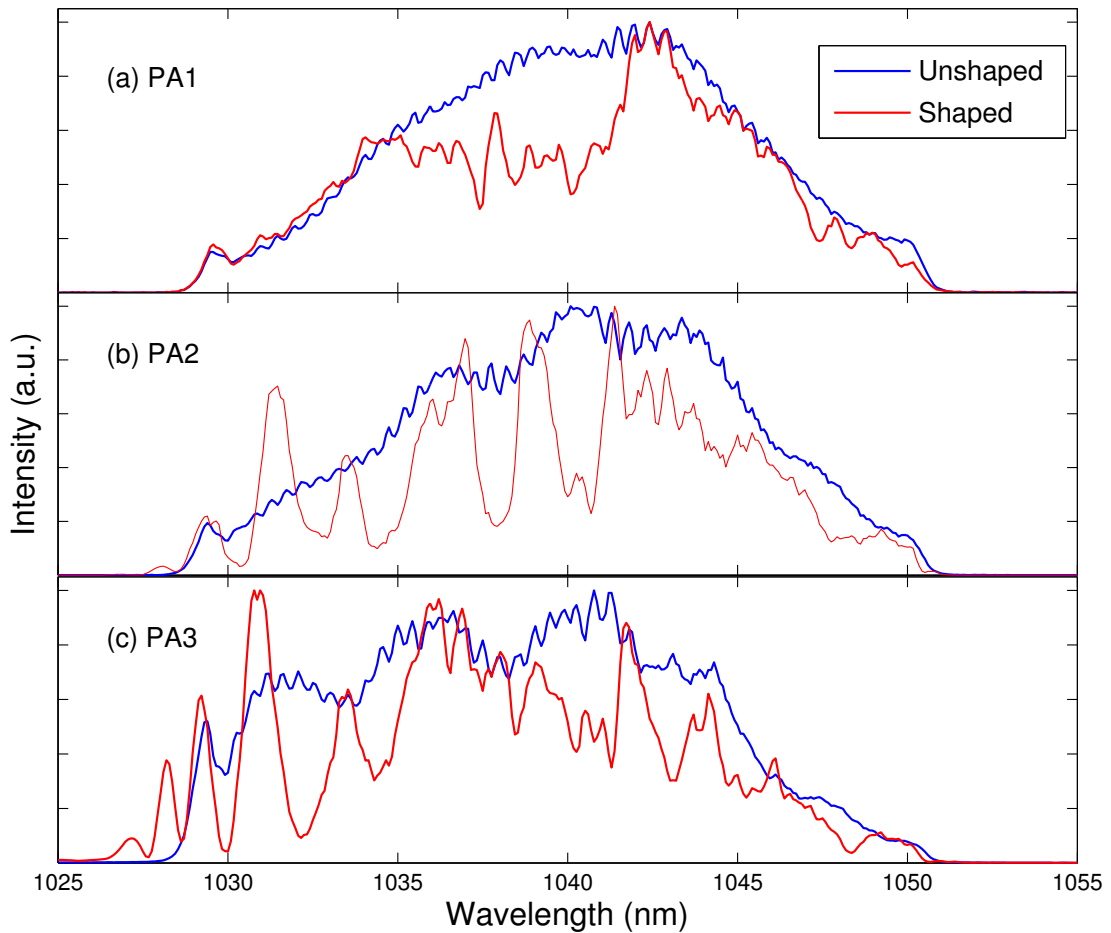
FIGURE 5.28: Measured spectra for high average power pulses, before and after optimisation, at the outputs of (a) pre-amplifier 1, PA1 (b) pre-amplifier 2, PA2 and (c) power amplifier, PA3.

It is important to note here that the maximisation of TPA signal does not guarantee the generation of a specific spectral shape at the output. Another approach was used in ref. [5] to produce a parabolic shaped spectrum after nonlinear amplification via an amplitude-only pre-shaping in order to obtain high fidelity pulses after compression. This approach can can work only up to a certain extent. Moreover, this method calls for extra effort to compensate for accumulated higher-order phase from the material dispersion. To add to this, when a more complex set-up including cascaded amplifier stages, is involved, as in the set-up used for these experiments, this approach is less likely to be successful.

In conclusion, an adaptive amplitude and phase pre-shaping technique for producing high-fidelity femtosecond pulses in a fibre CPA system were successfully demonstrated. This technique has been confirmed to be robust, effective, and efficient, in compensating

for both accumulated phase from higher-order material dispersion as well as nonlinear phase-modulation. Using this technique, a train of pulses was produced with an average power of 12.6 W at a 50 MHz repetition rate from the fibre CPA system, which were compressible to high quality pulses with a pulse duration of 170 fs. This method also eliminates the need for painstaking characterisation and design considerations to optimise fibre CPA system performance. Although it was found that, with increasing nonlinearity (as with higher power pulses), a finer control over the pulse shaping was necessary to achieve high fidelity pulses upon compression. This technique should enable power-scaling to higher average powers (on-going experiment within the group) and also energy-scaling at various repetition rates (briefly investigated in the next chapter). In addition to producing high-fidelity compressed pulses, this technique has the potential to produce arbitrary shaped pulses necessary in various applications, including coherent control [19].

References

[1] F. Roser, D. Schimpf, O. Schmidt, B. Ortac, K. Rademaker, J. Limpert, and A. Tünnermann, "90 w average power 100 μj energy femtosecond fiber chirped-pulse amplification system," *Optics Letters* **32**(15), pp. 2230–2232, 2007.

[2] F. Roser, J. Rothhard, B. Ortac, A. Liem, O. Schmidt, T. Schreiber, J. Limpert, and A. Tünnermann, "131 w 220 fs fiber laser system," *Optics Letters* **30**(20), pp. 2754–2756, 2005.

[3] F. Roser, T. Eidam, J. Rothhardt, O. Schmidt, D. N. Schimpf, J. Limpert, and A. Tünnermann, "Millijoule pulse energy high repetition rate femtosecond fiber chirped-pulse amplification system," *Optics Letters* **32**(24), pp. 3495–3497, 2007.

[4] M. D. Perry, T. Ditmire, and B. C. Stuart, "Self-phase modulation in chirped-pulse amplification," *Optics Letters* **19**(24), pp. 2149–2151, 1994.

[5] D. N. Schimpf, J. Limpert, and A. Tünnermann, "Controlling the influence of spm in fiber-based chirped-pulse amplification systems by using an actively shaped parabolic spectrum," *Optics Express* **15**(25), pp. 16945–16953, 2007.

[6] F. He, H. S. S. Hung, J. H. V. Price, N. K. Daga, N. Naz, J. Prawiharjo, D. C. Hanna, D. P. Shepherd, D. J. Richardson, J. W. Dawson, C. W. Siders, and C. P. J. Barty, "High energy femtosecond fiber chirped pulse amplification system with adaptive phase control," *Optics Express* **16**(8), pp. 5813–5821, 2008.

[7] L. Lefort, J. H. V. Price, D. J. Richardson, G. J. Spuhler, R. Paschotta, U. Keller, A. R. Fry, and J. Weston, "Practical low-noise stretched-pulse yb3+-doped fiber laser," *Optics Letters* **27**(5), pp. 291–293, 2002.

[8] C. E. Shannon, "Communication in the presence of noise," *Proceedings of the IEEE* **86**, pp. 447–457, 1998.

[9] R. L. Fork, C. H. B. Cruz, P. C. Becker, and C. V. Shank, "Compression of optical pulses to 6 femtoseconds by using cubic phase compensation," *Optics Letters* **12**(7), pp. 483–485, 1987.

[10] H. A. Haus and E. P. Ippen, "Self-starting of passively mode-locked lasers," *Opt. Lett.* **16**(17), pp. 1331–1333, 1991.

[11] E. B. Treacy, "Optical pulse compression with diffraction gratings," *IEEE journal of Quantum Electronics* **QE-5**(9), pp. 454–458, 1969.

[12] A. M. Weiner, "Femtosecond pulse shaping using spatial light modulators," *Review of Scientific Instruments* **71**(5), pp. 1929–1960, 2000.

[13] A. Prakelt, M. Wollenhaupt, A. Assion, C. Horn, C. Sarpe-Tudoran, M. Winter, and T. Baumert, "Compact, robust, and flexible setup for femtosecond pulse shaping," *Review of Scientific Instruments* **74**(11), pp. 4950–4953, 2003.

[14] R. Storn and K. Price, "Differential evolution - a simple and efficient heuristic for global optimization over continuous spaces," *Journal of Global Optimization* **11**(4), pp. 341–359, 1997.

[15] J. Prawiharjo, N. K. Daga, R. Geng, J. H. Price, D. C. Hanna, D. J. Richardson, and D. P. Shepherd, "High fidelity femtosecond pulses from an ultrafast fiber laser system via adaptive amplitude and phase pre-shaping," *Opt. Express* **16**(19), pp. 15074–15089, 2008.

[16] J. Prawiharjo, F. Kienle, N. K. Daga, D. C. Hanna, D. J. Richardson, and D. P. Shepherd, "High-quality energy-scalable femtosecond pulses from a fibre-based chirped pulse amplification system via adaptive pulse shaping," *2009 Conference on Lasers and Electro-Optics Europe and 11th European Quantum Electronics Conference (CLEO/EQEC)* , p. 1 pp., 2009.

[17] D. Schimpf, E. Seise, J. Limpert, and A. Tünnermann, "Decrease of pulse-contrast in nonlinear chirped-pulse amplification systems due to high-frequency spectral phase ripples," *Opt. Express* **16**(12), pp. 8876–8886, 2008.

[18] G. P. Agrawal, *Nonlinear Fibre Optics*, Academic Press, third ed., 2001.

[19] B. J. Pearson, J. L. White, T. C. Weinacht, and P. H. Bucksbaum, "Coherent control using adaptive learning algorithms," *Physical Review A* **6306**(6), pp. 063412–(1–12), 2001.

Chapter 6

Energy-scalable femtosecond pulse generation from an ultrafast fibre laser system

6.1 Introduction

Fibre-based systems have been very attractive sources for many applications due to the various attributes such as confined-mode geometry, long propagation length, compact systems, etc. Furthermore, as discussed earlier high average powers and high pulse energies are also required for these different applications. But, achieving high peak powers and high energy in a fibre-based system is non-trivial as the properties like confined mode and long propagation lengths in itself limit the achievable peak powers associated with high energy pulses. The main aim for a fibre-based high pulse energy system is to reach the maximum achievable pulse energy so as to extract most of the stored energy from the gain medium of the amplifier. At present, the CPA technique is well-established for high energy amplification in solid-state laser systems. But it does not comply with the compactness, robustness, ease of alignment, etc. expected from a fibre based system because diffraction grating set-ups used in CPA technique for pulse stretching and compression are typically large and alignment in free-space optics is also more sensitive.

In our previous work [1], the generation of high average power, high quality femtosecond pulses with a repetition rate of 50 MHz in the fibre CPA system was demonstrated. This was achieved at two different power levels with the use of an adaptive pulse pre-shaping technique that compensated for high-order dispersion in fibres with a total length of less than 12 m and a B-integral of up to 1.6π rad. The experimental arrangement described in detail in chapter 5 is modified slightly with an addition of a fibre stretcher before the pre-amplifier (PA1) for the results outlined in this chapter. The primary goal of this experiment was to demonstrate the energy-scalability of the system along with power scaling already highlighted in the previous chapter. The main challenge with this kind of a set-up is to match all the orders of the dispersion parameters between the fibre stretcher and the grating compressor which can be challenging as discussed in chapter 4. Further investigation dealing with different fibre stretcher lengths was later carried out by other members of the group.

In this chapter, the versatility of adaptive pulse pre-shaping technique to generate high-quality pulse train with variable repetition rate and energy in a fibre CPA system is highlighted. The fibre CPA system in this case consists of a 1 km of fibre stretcher with a B-integral reaching as high as 2.2π rad [2].

Section 6.2 outlines the experimental arrangement used for the results outlined in this chapter. Section 6.3 then goes on to describe the experimental results for three different repetition rates starting with an initial repetition rate of 48 MHz. The repetition rate is then reduced by 10 and 100 times to give 4.8 MHz and 480 kHz and similar sets of data are recorded. The chapter ends with a conclusion and future outlook in the last section, sec. 6.4.

6.2   Experimental set-up

The schematic of the experimental arrangement for this set of experiments is shown in fig. 6.1. The seed source is once again, the SSO described in detail in sec. 5.2.1. The SSO produced a train of chirped pulses with a duration of ~ 2 ps at 48 MHz repetition rate, 16 nm spectral FWHM at a centre wavelength of 1042 nm. The repetition rate was
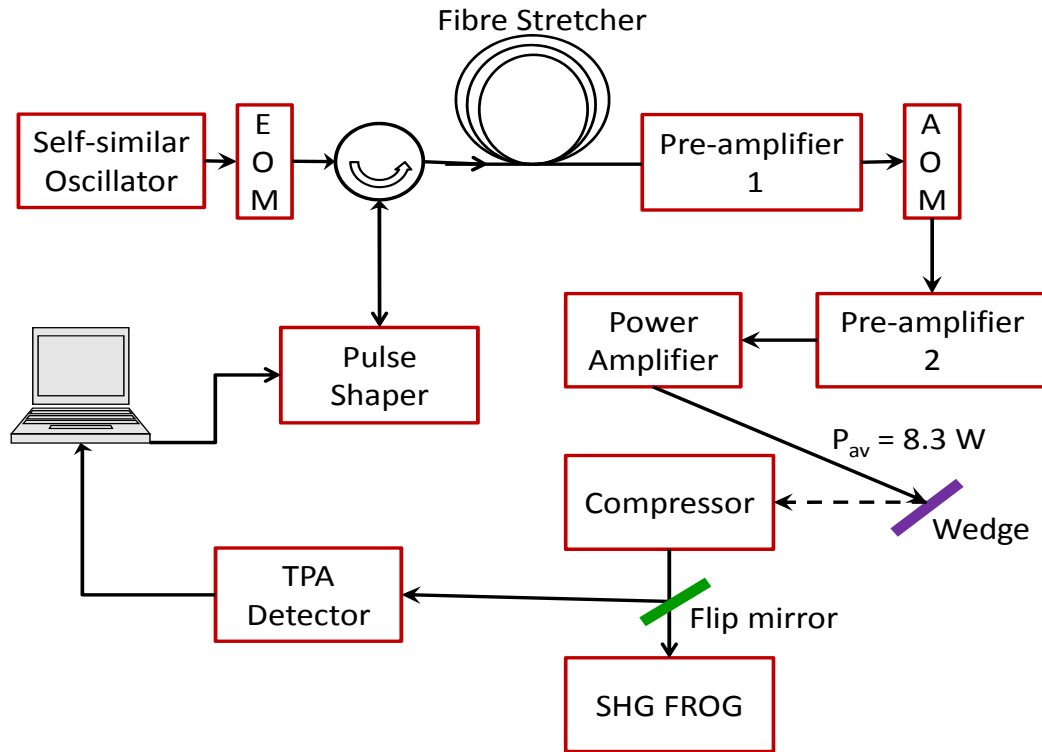
FIGURE 6.1: Schematic of the system for high fidelity energy-scalable femtosecond pulse generation.

reducible by EOM and AOM placed at appropriate places within the amplifier chain as indicated in the figure. The fibre stretcher was a 1 km long HI 1060 single-mode fibre. Adaptive pulse shaping was implemented once again to maximise a TPA signal from a GaAsP photodiode, illuminated by the output pulse train, placed after the compressor. As in the previous case, this was essentially maximising the peak power of the pulse train, by controlling the LC-SLM using a self-adaptive differential evolution algorithm (JADE) [3]. This algorithm is a modified version of the DE algorithm that was employed in the previous work. The pulses were characterised using the home-built SHG FROG and the spectrum was measured using an OSA as in the previous chapter.

6.3   Experimental results

In this set of experiments the repetition rate was reduced by various factors from the initial value of 48 MHz by varying the time delay of the EOM and AOM. Furthermore, in each case, the separation of the gratings pair in the compressor was optimised prior

to implementing the adaptive pulse shaping following from the conclusions of chapter 4 where optimising the grating pair distance prior to adaptive shaping yielded better results. Spectra for pulses with different repetition rates, as measured after the two pre-amplifiers, are indicated in fig. 6.2. These plots for the different repetition rate reduction factors are offset in the vertical axis for a clearer picture. Small ASE and spectral broadening is noted for decreasing repetition rates. Also, a slight reduction in the spectral amplitude for lower repetition rates, accompanied with a reduction in the noise level is observed. The reduction factors 1x, 10x and 100x are highlighted in the figure as the experiments described in the following paragraphs are performed for these values.
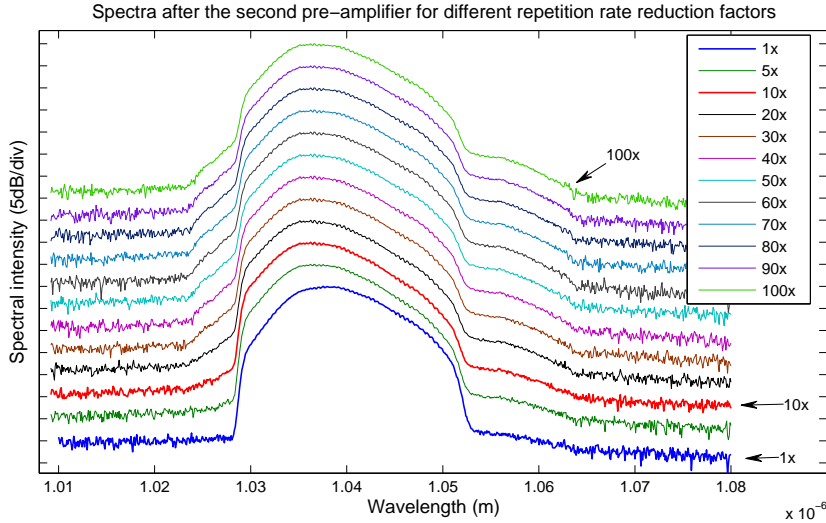

FIGURE 6.2: Spectra comparison for the different repetition rates of the system, measured after the second pre-amplifier, PA2. The initial repetition rate was measured to be 48.7 MHz.
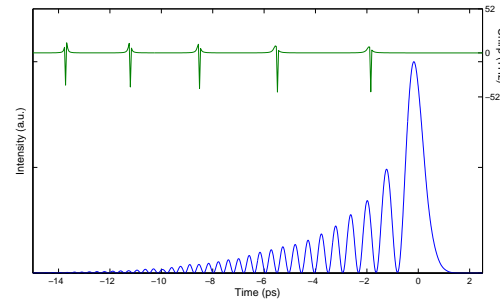
6.3.1 No repetition rate reduction: 48 MHz

Initially, the repetition rate was not reduced by any factor, that is, maintained at 1x or 48 MHz. The power levels in the system were 3 mW and 150 mW, measured after the EOM and the second pre-amplifier respectively. The maximum average power after the final power amplifier was measured to be ∼10 W.
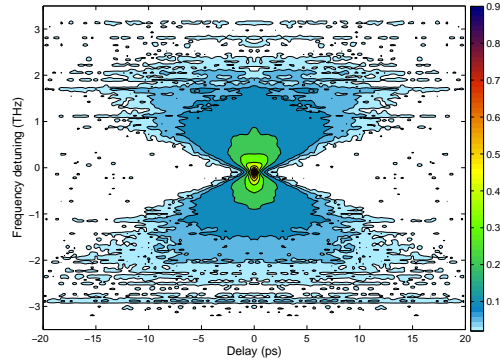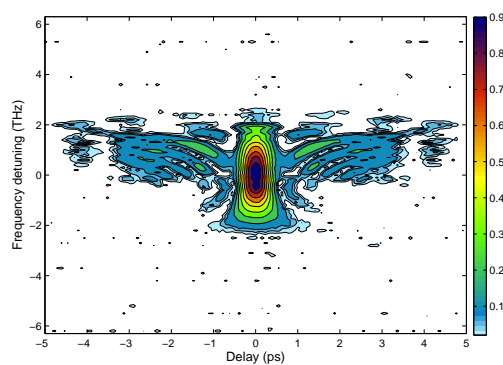
(a)
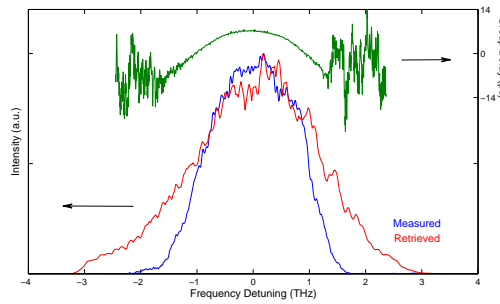
(b)

(c)
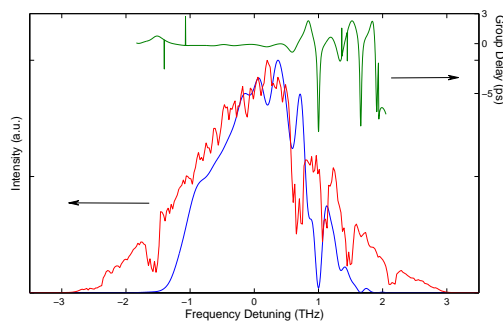
FIGURE 6.3: Unshaped data set for full repetition rate of 48 MHz. (a) Retrieved FROG trace, (b) Measured(blue) and retrieved(red) spectra with group delay (green), (c) Intensity profile (blue) with chirp (green).

To begin with, FROG trace was acquired for the original unshaped pulses, that is with no deliberate phase applied with the LC-SLM. It can be seen in fig. 6.3(c) that the pulses are asymmetric with oscillation structure near the trailing edge of the pulse. As mentioned in the previous chapter, this is an indication of the influence of accumulated, uncompensated and positive TOD on the output of the system [4]. Once again, this is expected due to the absence of any TOD compensating element in the CPA system. But unlike figs. 5.17(c) and 5.18(c), the oscillations do monotonically decrease at the

end, indicative of absence of any SPM [4]. The pulses in the set-up are stretched in the fibre stretcher avoiding very high intensities and thus no significant nonlinear effects like SPM are observed. It is worth noting here that in fig. 6.3(c) it appears that the oscillatory structure is towards the leading edge. This is an indication and an example of the ambiguity in the sense of direction in a SHG-FROG result. We know from the experimental set-up and component contributions that the TOD should be positive in this case and therefore the oscillations should be near the trailing edge.

(a)

(b)
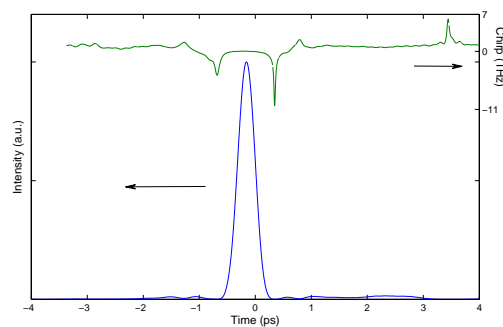
(c)

FIGURE 6.4: Shaped data set for full repetition rate of 48 MHz. (a) Retrieved FROG trace, (b) Measured(blue) and retrieved(red) spectra with group delay (green), (c) Intensity profile (blue) with chirp (green).

Once the unshaped pulses were characterised, pulses with an average power of 10 W measured before the compressor, were optimised using the JADE algorithm. For this experiment as well, every 8th pixel of the SLM was controlled starting from pixel number 16 all the way up to and including pixel number 112. 6 times improvement in the TPA signal, measured after the compressor was noted after 250 generations. The optimisation was run for more generations but showed no further improvement and low diversity in the population indicated that the optimum was reached. The shaped data set is indicated in fig. 6.4.

6.3.2   10 times repetition rate reduction: 4.8 MHz

(a)

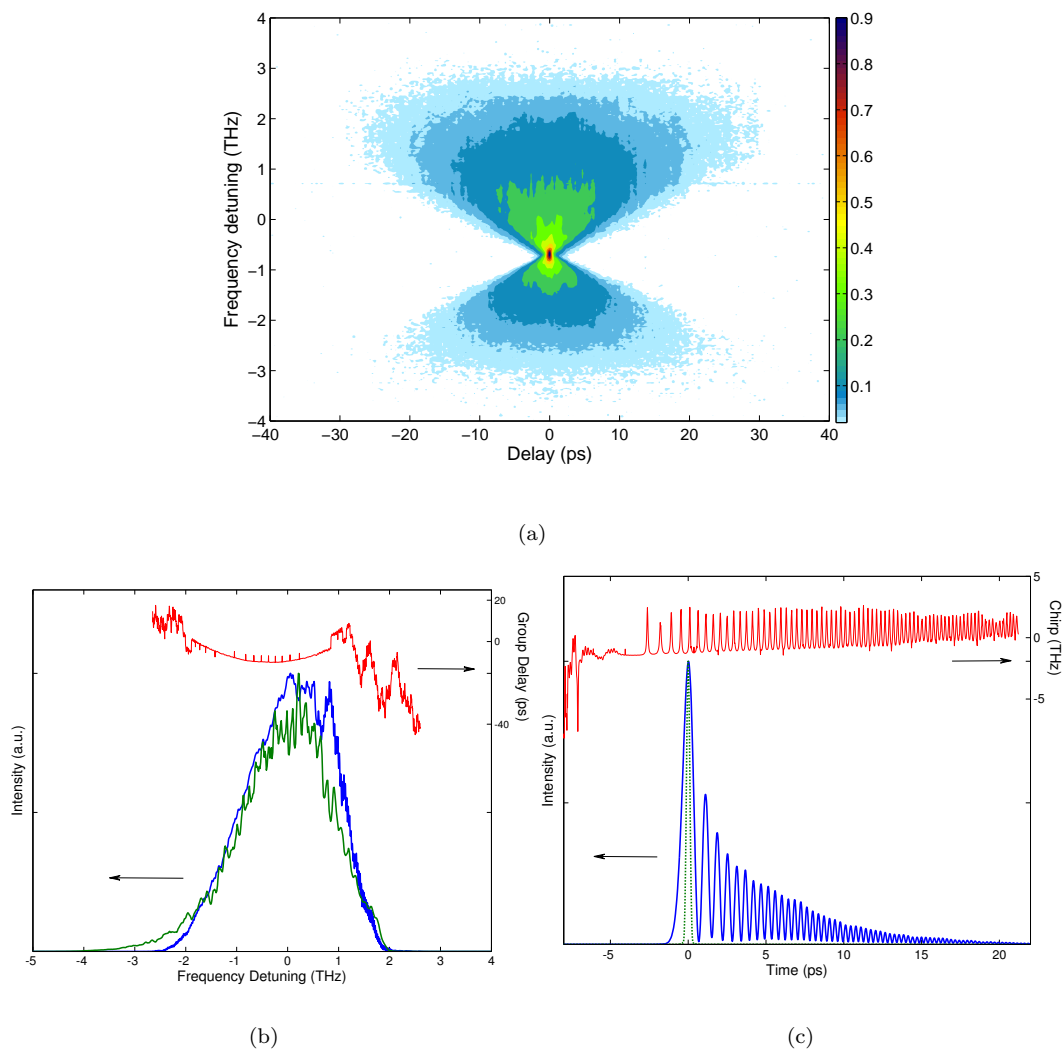(b)   (c)

FIGURE 6.5: Unshaped data set for 4.8 MHz repetition rate. (a) Retrieved FROG trace, (b) Measured (blue) and retrieved (green) spectra with group delay (red), (c) Intensity profile (blue) with transform limited pulse (green) and chirp (red).
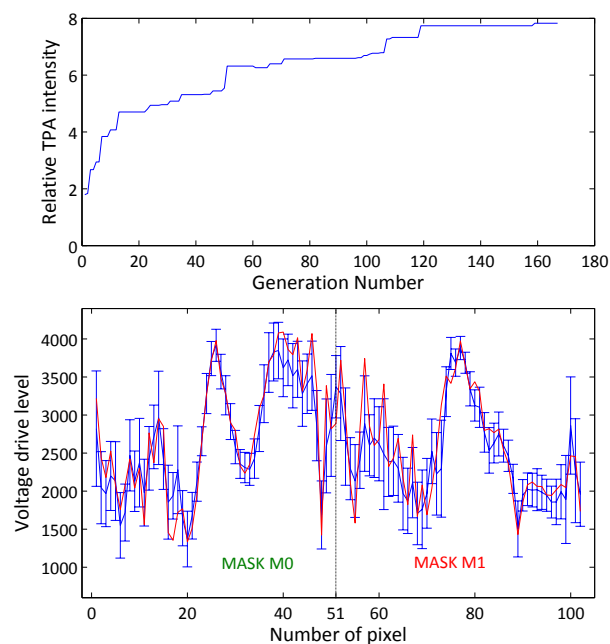
FIGURE 6.6: Evolution of the TPA detector signal for 10x reduction in repetition rate. Initially every 8th pixel was controlled followed by every 4th pixel from the 50th generation.

Moving on, the repetition rate was reduced to one-tenth of the original value, that is, to $4.8\,$MHz by varying the time delay as mentioned earlier. Once again, data sets for unshaped and shaped pulses were recorded and are highlighted in figures 6.5 and 6.7 respectively. The TPA signal optimisation with every generation along with the best individual with diversity in population are indicated in fig. 6.6 (a) and (b) respectively. Almost 8 times improvement in the TPA signal was observed in this case. Also, the autocorrelation traces in fig. 6.7(c) indicate that the pulse was compressed to $\sim$428 fs for a transform-limited pulse duration of $\sim$280 fs. Far more oscillations are observed on the spectra as one moves on from higher repetition rate to lower values (higher energies). Oscillations on the spectra also increase for the shaped pulses as compared to the unshaped spectrum.
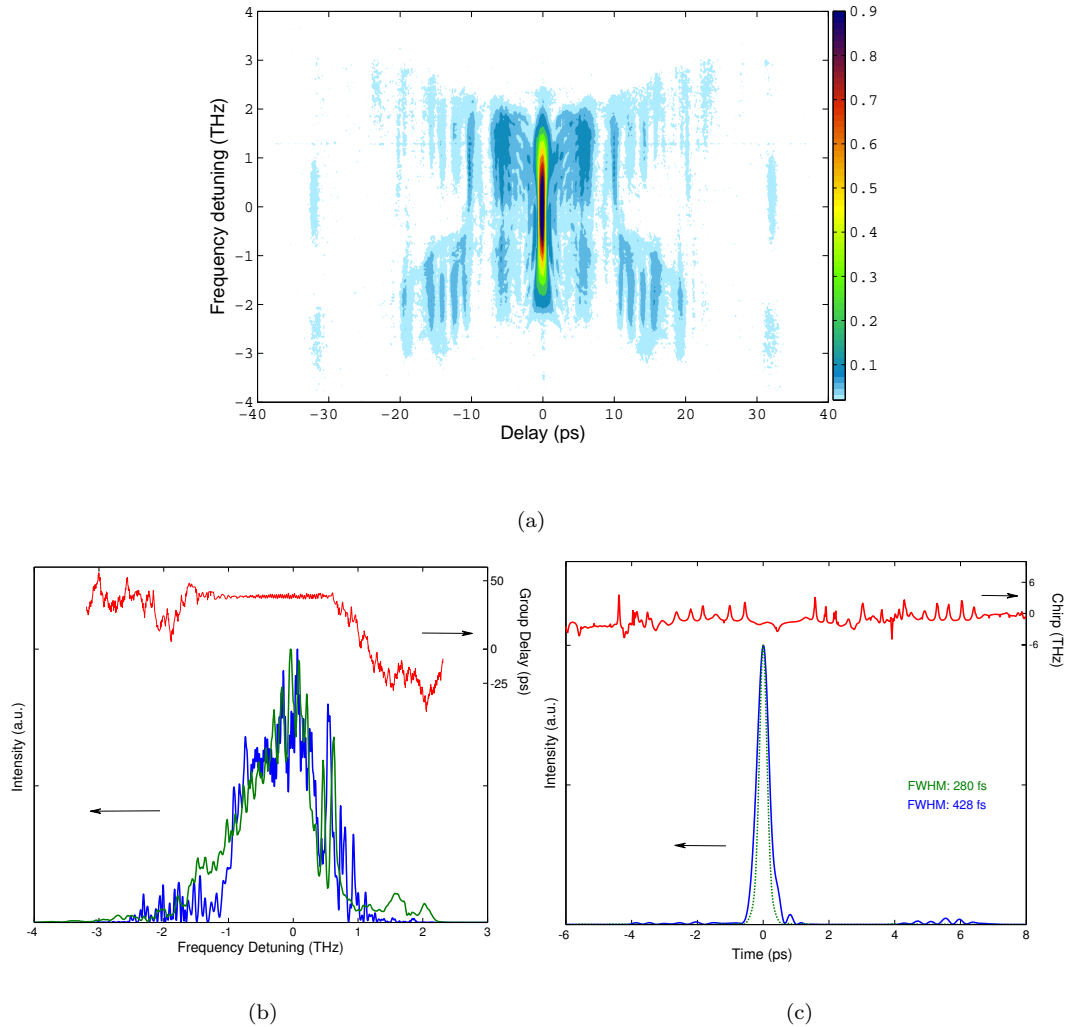
(a)

(b)

(c)

FIGURE 6.7: Shaped data set for 4.8 MHz repetition rate. (a) Retrieved FROG trace, (b) Measured (blue) and retrieved (green) spectra with group delay (red), (c) Intensity profile (blue) with transform limited pulse (green) and chirp (red).

Here for the repetition rate of 4.8 MHz, the average power was measured to be 6.2 W after the final power amplifier, resulting in the calculated pulse energy of 1.3 μJ with a B-integral of 0.4π rad. The peak power for the unshaped pulse is estimated to be 0.6 MW with the value increasing to 2.1 MW for the shaped pulse. The shaped pulse with a pulse duration of ~428 fs was measured to be roughly 1.5 times the transform limited pulse duration.

6.3.3   100 times repetition rate reduction: 480 kHz
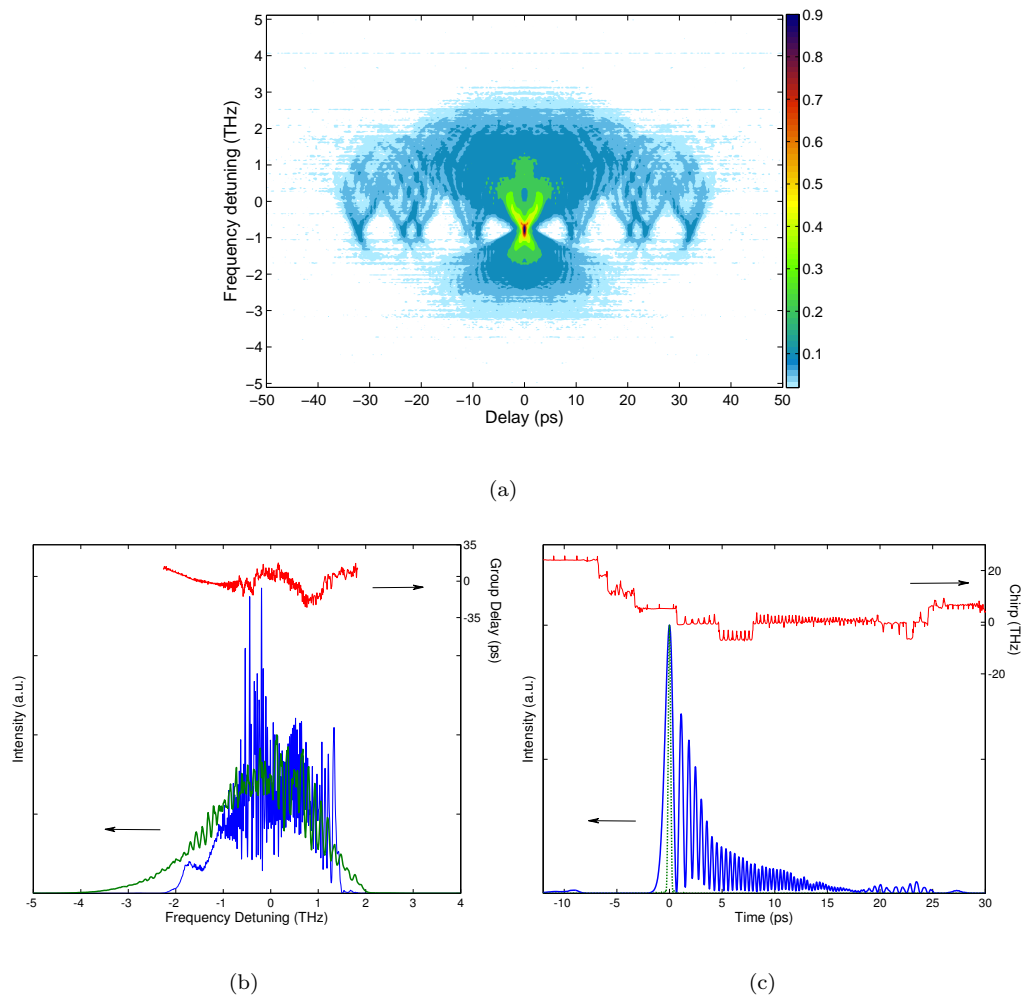

(a)

(b)

(c)

FIGURE 6.8: Unshaped data set for 480 kHz repetition rate. (a) Retrieved FROG trace, (b) Measured (blue) and retrieved (green) spectra with group delay (red), (c) Intensity profile (blue) with transform limited pulse (green) and chirp (red).
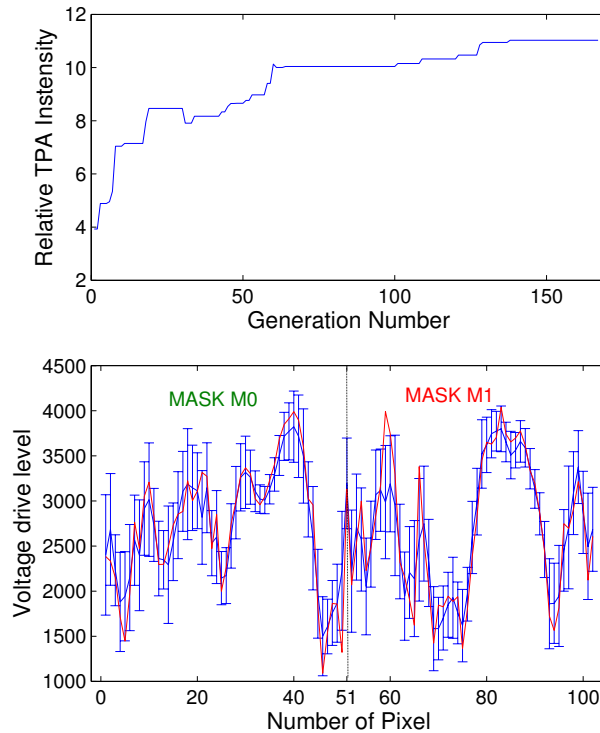
FIGURE 6.9: Evolution of the TPA detector signal and optimum phase profile for 100x repetition rate reduction. Initially every 8th pixel was controlled followed by every 4th pixel from the 50th generation.

Finally, the repetition rate was reduced to one-hundredth of the original value to 480 kHz. It was also possible to achieve intermediate reduction factors for the repetition rate, but only the extreme was considered to test the limit of the system with available equipment and set-up. As before, data sets for unshaped and shaped pulses were recorded and are highlighted in figures 6.8 and 6.10 respectively. The TPA signal optimisation with every generation along with the best individual with diversity in population are indicated in fig. 6.9 (a) and (b) respectively. This time, almost 11 times improvement in the TPA signal was observed. Also, the autocorrelation traces in fig. 6.10(c) indicate that the pulse was compressed to ∼512 fs for a transform limited pulse duration of ∼330 fs. Once again, far more oscillations are observed on the spectra as compared to the spectra for no reduction or 10 times repetition rate reduction spectra.

Under these conditions, for the repetition rate of 480 kHz, the average power was measured to be 4.3 W resulting in the calculated pulse energy of 8.9 μJ with a B-integral of 2.2π rad. The peak power for the unshaped pulse is estimated to be 3.4 MW with the

value increasing to 12 MW for the shaped pulse. The shaped pulse with a pulse duration of ~512 fs was measured to be roughly 1.5 times the transform limited pulse width.

(a)

(b)

(c)
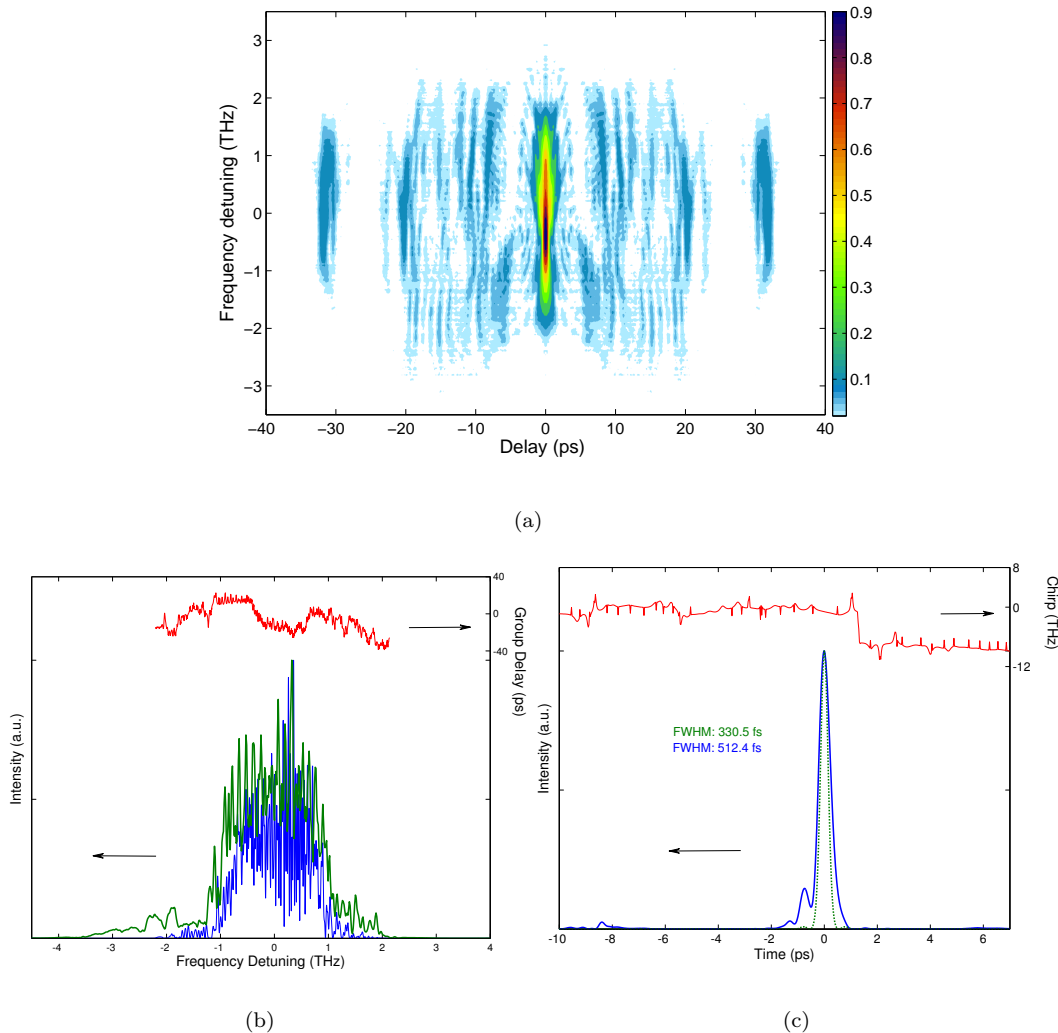
FIGURE 6.10: Shaped data set for 480 kHz repetition rate. (a) Retrieved FROG trace, (b) Measured (blue) and retrieved (green) spectra with group delay (red), (c) Intensity profile (blue) with transform limited pulse (green) and chirp (red).

6.4   Discussion and conclusion

The spectral data set for the pulse as it propagated through the system with fibre stretcher, was briefly studied for different energy levels by manipulating the different repetition rates. This is highlighted in fig. 6.2. We can see that there is apparently no distortion after the shaper even for the high energy pulse or the 480 kHz set of data

indicated by 100× in the figure. The spectrum is not significantly changed by pre-shaping when there is no SPM in the stretcher. This is consistent with the observation made previously in Chapter 4.

To summarise the results, figures 6.5(c) and 6.7(c) compare the FROG characterised pulse intensity profiles of the fibre CPA system before and after implementing the adaptive pulse pre-shaping for 10× repetition rate reduction. It can be seen that when the pulse is shaped the AC pulse width is measured to be ∼430 fs which is roughly 1.5 times the calculated transform-limited pulse width. The peak power was estimated to be 2.1 MW (for the output average power of 6.2 W) compared to 0.6 MW for the unshaped pulse and the energy per pulse was calculated to be 1.3 μJ with a B-integral of 0.4πrad, indicating that the main contribution to the pulse degradation at the output was the accumulation of TOD from the fibre stretcher and grating compressor. For a similar set of experiment with 100× repetition rate reduction, figures 6.8(c) and 6.10(c) compare the FROG characterised pulse intensity profiles before and after implementing the adaptive pulse pre-shaping respectively. The shaped AC pulse duration was measured to be ∼510 fs which was close to 1.5 times the estimated transform-limited AC pulse width. When the repetition rate of the pulse train was reduced to 480 kHz, the pulse energy increased to 8 μJ, with an increased B-integral of 2.2πrad, implying a significant contribution of accumulated nonlinear phase to the degradation of the pulse quality. The calculated peak power increased to 12 MW when shaped compared to 3.4 MW for the unshaped pulses at this reduced repetition rate. The average power with shaped pulses was measured to be 4.3 W in this case. In both the above repetition rate reduction experiments, adaptive pulse shaping improved the pulse quality, thereby increasing the peak power by a factor of 3.9 and 3.6 for the 1.3 μJ and 8 μJ pulse trains, respectively.

In conclusion, adaptive pulse pre-shaping has been demonstrated to be a powerful technique to achieve high-quality energy-scalable femtosecond pulses in a fibre-chirped pulse amplification system, without major system reconfiguration. Further work with different fibre stretcher lengths has been carried out by other members of the group. In the meantime, for the work presented in this thesis, the focus was shifted towards implementing the fibre CPA set-up as the pump source for a synchronously pumped optical parametric oscillator and the results thus obtained are discussed in the following chapter.

References

[1] J. Prawiharjo, N. K. Daga, R. Geng, J. H. Price, D. C. Hanna, D. J. Richardson, and D. P. Shepherd, "High fidelity femtosecond pulses from an ultrafast fiber laser system via adaptive amplitude and phase pre-shaping," *Opt. Express* **16**(19), pp. 15074–15089, 2008.

[2] J. Prawiharjo, F. Kienle, N. K. Daga, D. C. Hanna, D. J. Richardson, and D. P. Shepherd, "High-quality energy-scalable femtosecond pulses from a fibre-based chirped pulse amplification system via adaptive pulse shaping," *2009 Conference on Lasers and Electro-Optics Europe and 11th European Quantum Electronics Conference (CLEO/EQEC)* , p. 1 pp., 2009.

[3] Z. Jingqiao and C. S. Arthur, "Jade: Adaptive differential evolution with optional external archive," *IEEE Transactions on Evolutionary Computation* **13**(5), pp. 945–958, 2009.

[4] G. P. Agrawal, *Nonlinear Fibre Optics*, Academic Press, third ed., 2001.

Chapter 7

Adaptive pulse shaping in an ultrafast optical parametric oscillator

7.1 Motivation

Bond selective manipulation of matter with light has been a study of great interest to physicists, chemists and biologists. With ultrafast optical pulses, the bond excitation occurs faster than the rapid redistribution of the energy away from the specific bond making it possible to drive a chemical reaction towards a desired product or even away from an undesired one [1]. Although many experiments have already achieved coherent control in the visible and NIR wavelength regimes, the most common molecular vibrational modes are in the MIR region. Therefore, shaped femtosecond pulses in this fingerprint regime become important. These shaped pulses find various applications in driving conformational changes in proteins, spectroscopy, coherent control and imaging [2–6].

Direct pulse shaping in the MIR has been demonstrated with a free-electron laser [7] but the method used was not programmable and could generate only simple, linearly chirped pulses. Such a MIR source has been used in successful demonstrations of coherent control [8–11] leading to molecular dissociation, but this method is not capable of dynamically finding the optimum linear chirp required.

Coherent control in the MIR regime can be achieved through indirect pulse shaping for producing arbitrarily shaped pulses. It involves shaping a visible or NIR pulse using a LC-SLM or AOM before transferring the pulse shape to the MIR via a nonlinear optical process. Indirect pulse shaping in the MIR has been shown via DFG [12, 13], and OPA [14, 15]. Recently, Shim et al. reported direct pulse shaping in the MIR using a germanium AOM [16, 17].

Prior experiments in the Optical Parametric Oscillator group at the ORC have successfully demonstrated adaptive pulse shaping using a SPOPO, allowing idler wavelengths of $3.5\,\mu$m. Furthermore, the principles for applying adaptive control, including implementation of a SA algorithm to the system, have already been explored. Indirect control of the idler has been achieved via optimisation of a TPA signal demonstrating simple pulse compression and the generation of compressed double pulse with variable time delay [18].

More recently, the fidelity of parametric transfer in a SPOPO has been studied numerically and experimentally. This included a detailed numerical investigation of parametric transfer via DFG [19], followed by a numerical study to understand the effects of various parameters on fidelity of transfer in a SPOPO [20].

This chapter is divided in two main parts. The experimental work described in the first part aimed to investigate the parameters that affect parametric transfer in an SPOPO [21]. This is based on the conclusions from the previous theoretical work [20]. In particular, effects of signal bandwidth, output coupler reflectivity, input pump power, cavity length tuning and pump and idler temporal walk-off (TWO) are investigated. By considering all these factors high fidelity transfer from the NIR to the MIR is demonstrated. In this part, after a brief introduction describing the motivation for this work in section 7.1, the experimental set up is detailed in section 7.2. The results from the first set of experiments are described in section 7.3. This set of experimental work was carried out in collaboration with Hazel S.S. Hung.

In the second part of the chapter, an adaptively shaped fibre CPA system, described in detail in chapter 5, is used as the pump source instead of the picosecond Nd:YLF source used in part one, for a femtosecond OPO to demonstrate adaptive shaping. After a brief

description of the OPO set-up in section 7.4.1, the initial results of shaped MIR idler from this set of experiments are presented in section 7.4.2. The author was responsible for the design, set-up and characterisation of the femtosecond OPO, whereas the code used for the adaptive shaping was written by Jerry Prawiharjo.

7.2 Experimental set-up for measurement of pump to idler transfer fidelity

The experimental set-up is shown schematically in fig. 7.1. It consists of a pump source, an SPOPO and a sonogram. The pump source is a Nd:YLF laser with pulse repetition rate of 120 MHz, typical peak power of 15 kW, and average pump power of up to 4 W, with a 4 ps pulse width at a central wavelength of 1047 nm. The pump is directed through a telescopic arrangement so as to efficiently launch into the core of a PM single mode fibre. The average input power is reduced to a maximum of 3.5 W to avoid PM fibre and SLM damage.
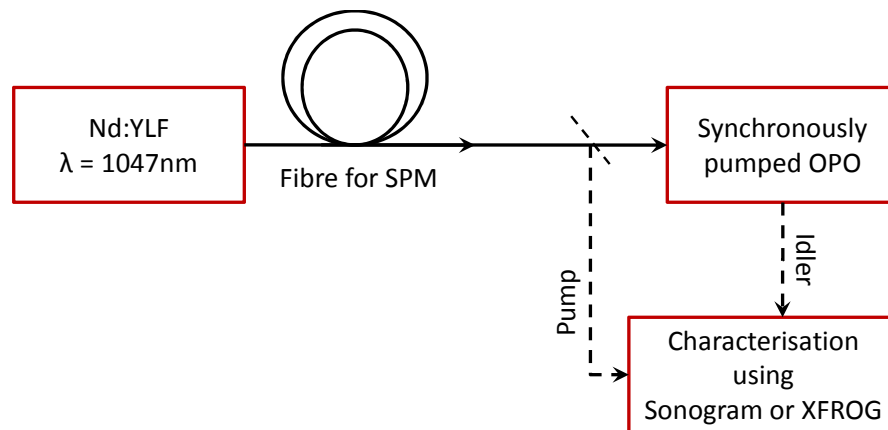

FIGURE 7.1: Schematic layout of the experimental set-up.

The 50 cm long PM fibre in the set-up introduces SPM, spectrally broadening the pump pulse to give a FWHM of 3.5 nm while having negligible effect on the pulse duration. This is done so as to give a more complex pulse characteristic to investigate fidelity as opposed to a simpler flat-phase bandwidth-limited pulse.
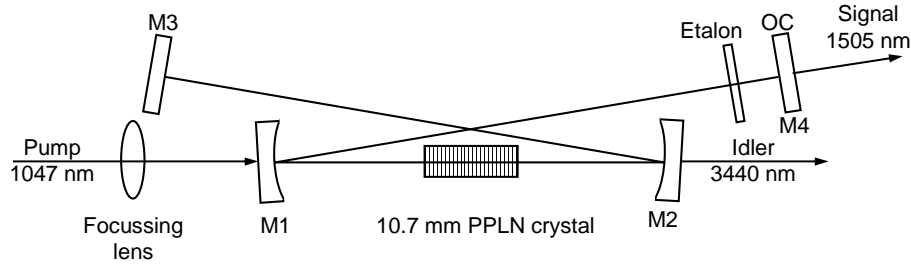
FIGURE 7.2: The SPOPO set-up with four cavity mirrors: M1:M4 and 10.7 mm PPLN crystal and an etalon.

The shaped pulses from the output of the fibre, at an average power of 1.15 W, are then fed into the SPOPO. The resonator cavity of the SPOPO, as shown in fig. 7.2, consists of four mirrors, M1-M4, arranged in a bow-tie configuration with a 10.7 mm long PPLN crystal placed between the 150 mm radius of curvature mirrors, M1 and M2. The crystal is heated in an oven at a temperature of 110^oC. It has five different poling periods ranging from 29.2 μm to 30.2 μm. This gives a signal wavelength range of 1480-1600 nm, with the corresponding idler wavelengths of 3580-3030 nm. M1 is highly transmitting (HT) at the input wavelength of 1047 nm and highly reflecting (HR) in the signal wavelength region of 1200-2000 nm. M2 and M3 (plane mirror) are also HR in the signal waveband. The plane mirror M4 acts as an output coupler (OC) or is HR in the signal waveband. All the mirrors have low reflectivity in the idler wavelength range. The resonator cavity length is set so that the signal round trip time is comparable to the inverse of the pump pulse repetition rate of 120 MHz. Mirrors M1 and M2 have small radii of curvature to ensure near confocal focussing of the signal (38 μm) at the centre of the PPLN, to achieve high gain and give a good match to the near confocally focussed pump (30.5μm). The pump M^2 was measured to be 1.1 in both the axes.

The pump and signal spectral intensity profiles were obtained using an OSA with a resolution of 0.1 nm. The idler on the other hand, was acquired using a Bentham M300 monochromator with a nitrogen cooled InSb detector, with a resolution of 0.4 nm. The cross-correlation sonogram technique [22] was employed for the complete characterisation of the pump and idler pulses. The layout of the sonogram set-up is presented in fig. 7.3. It consists of a temporal delay arm using a motorised corner cube reflector, and a spectral gating arm with a diffraction grating as shown. The spectral gating arm includes a
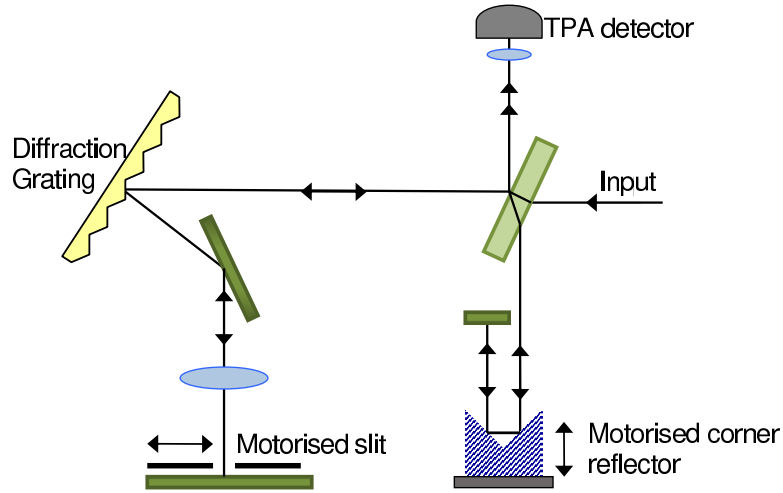
FIGURE 7.3: The sonogram set-up.

motorised slit whose width is set to allow one-tenth of the spectrum through to get enough spectral resolution without throwing away too much power. Similar set-ups, but using different TPA detectors, were employed for the pump and idler characterisations. A GaAs TPA detector was used for the NIR pump while an extended InGaAs TPA detector replaced it for the MIR idler characterisation. A lock-in amplifier was added to the set-up to improve its sensitivity. The results of the experiment are discussed in the next section.

7.3 Results and Analysis

The experimental results showing the effects of various factors on the parametric transfer in an SPOPO are detailed in this section.

To begin with, the idler wavelengths corresponding to the available SPOPO signal wavelengths for different poling periods were measured. The temporal walk-off between pump and idler and pump and signal, for different wavelengths in lithium niobate, were calculated using the Sellmeier equation [23]. These values are summarised in fig. 7.4. As specific periods in steps of $0.2\,\mu$m were available, only discrete idler wavelengths are observed. The operating wavelengths for the signal and idler were chosen to be $1505\,$nm and $3440\,$nm respectively to give the minimum pump-idler TWO.
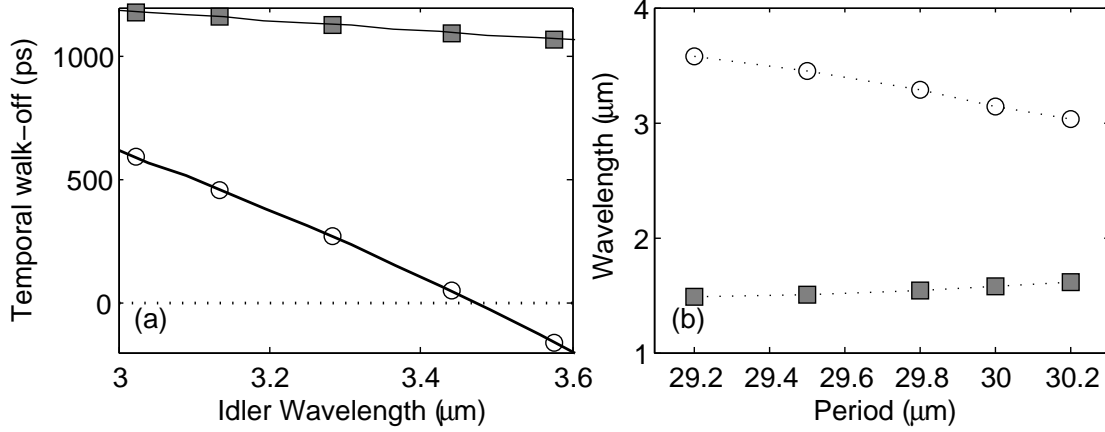
FIGURE 7.4: (a) Pump-signal (squares) and pump-idler (circles) temporal walk-off (TWO).(b)The signal (squares) and idler (circles) wavelengths corresponding to the five different poling periods used.

The effects of different resonator parameters on the transfer fidelity were then studied followed by an investigation of the effects of TWO in the PPLN crystal. For the experimental parameters used here, the GVD effects are expected to be negligible.

In these experiments, the autocorrelations, spectral intensities and pump and idler sonograms were used as the basis of pulse characterisation. However, in practice, the spectra offered a near complete analysis, as it was observed that the changes occurred mainly in the spectral domain. The measured and retrieved input pump pulse characteristics are shown in figure 7.5.

For ease of comparison, we define a quantitative measure of fidelity of transfer z used for the analysis only in terms of the spectrum, as:

$$z = \frac{\int \left| \widetilde{E}_p(\Omega) \right|^2 \left| \widetilde{E}_i(\Omega) \right|^2 d\Omega}{\left[\int \left| \widetilde{E}_p(\Omega) \right|^4 d\Omega \int \left| \widetilde{E}_i(\Omega) \right|^4 d\Omega \right]^{1/2}}, \tag{7.1}$$

where Ω is the frequency detuning and $\left| \widetilde{E}_{p,i}(\Omega) \right|^2$ is the spectral intensity of the pump, or idler denoted by subscripts p and i, respectively. This equation has been adapted from the expression for Z given in ref. [20] which also incorporates phase. Fidelity z, ranges between zero and unity, where zero corresponds to no overlap and unity indicates perfect overlap.
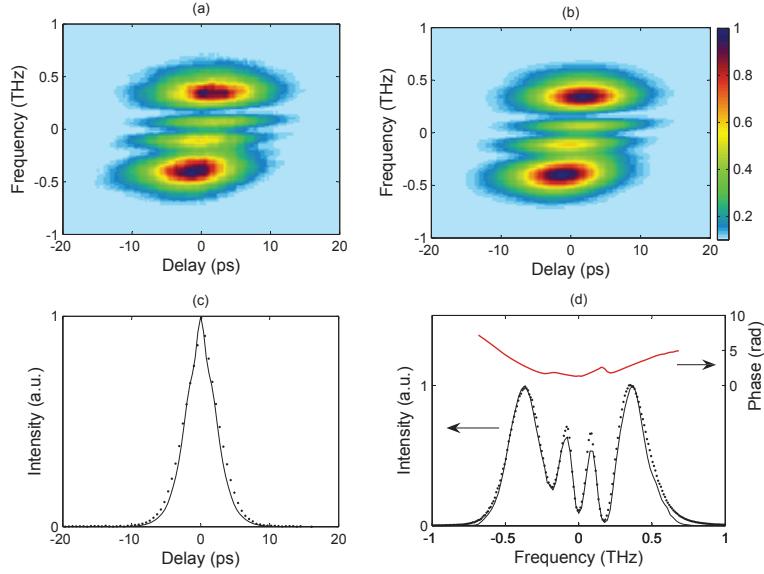
FIGURE 7.5: Input pump pulse characteristics (a)measured sonogram (b)retrieved sonogram (c)measured(dotted) and retrieved(solid line) autocorrelations (d)measured (dotted) and retrieved (solid line) spectra with retrieved phase.

The experiment was set up to give high fidelity parametric transfer, as suggested by the numerical investigations [20]. This included factors such as placing an optical band pass filter (OBPF) in the resonator to narrow the signal bandwidth, working at high pump depletion, high OC reflectivity for signal, cavity length tuning to compensate for the pump-signal TWO, etc. The following sections summarise the results obtained when one of these parameters was varied individually. It is worth noting here that due to slight changes in the system operation from day to day, there is a minor variation in the spectral intensity profile as seen in the different experiments performed on different days.

7.3.1 Effects of Resonator Parameters

Optical band pass filter

The effect of an etalon on signal bandwidth and on pulse shape transfer fidelity is investigated first. Etalons of different thicknesses were introduced in the resonator cavity and the corresponding fidelities of transfer compared. Without an etalon, the signal bandwidth after the OC was found to be 1.3 nm (172.2 GHz) at 1505 nm with ~100 mW
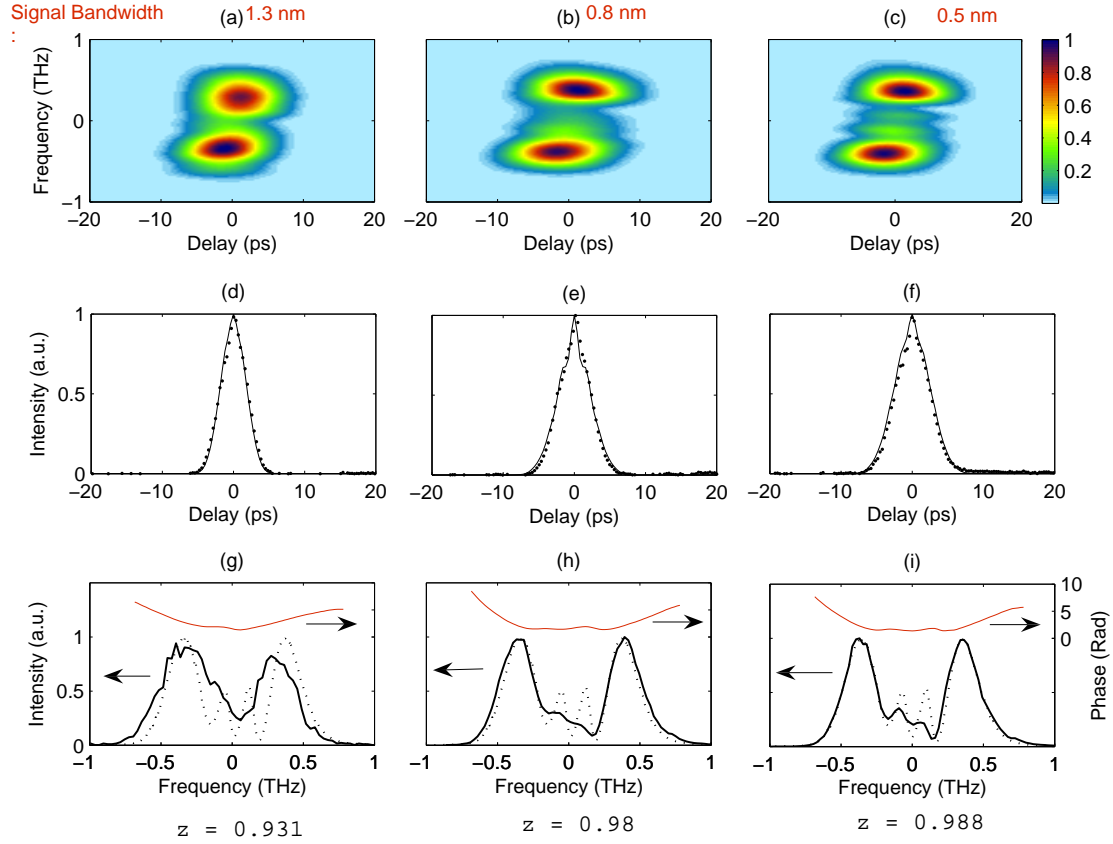
FIGURE 7.6: Idler sonogram data: (a)-(c): retrieved sonogram; (d)-(f): measured (dotted) and retrieved (solid) autocorrelations; (g)-(i): measured (solid) idler spectra with retrieved phase (red) and measured pump spectra (dashed).

threshold for OPO operation. An etalon, when placed in the resonator, resulted in a significant reduction in the signal bandwidth with an increase in the threshold of operation. With etalons of two different thicknesses, $150\,\mu$m and $200\,\mu$m, signal bandwidths of $0.8\,$nm ($106\,$GHz) and $0.5\,$nm ($66.2\,$GHz) were obtained. In both the cases, the threshold was found to be $\sim180\,$mW. The angles of the etalons were varied to maintain the signal wavelength at $1505\,$nm. Fine-tuning of the cavity length helped maintain the two main idler spectral peaks at the same height (see section 7.3.2), as in the pump spectrum (fig. 7.5). Figure 7.6 shows the retrieved idler sonogram plots with corresponding z values. Placing an etalon in the resonator results in a narrower signal bandwidth, that is, a longer signal pulse, making the SPOPO stable over a wider range of cavity lengths and therefore fine tuning the cavity length does not affect the extent of transfer investigated here. For the set of data presented in this figure, the retrieved spectra are very similar to the measured and are therefore left out for clarity.

Figure 7.6 clearly indicates the improvement in transfer fidelity with an etalon in the cavity to narrow the signal bandwidth, as would be expected from equation 2.32.

Pump depletion

Next, the effect of pump depletion is studied. In line with the numerical investigations [20], higher pump depletion should generally result in improved transfer fidelity, until back conversion becomes significant. Figure 7.7 highlights the results obtained from this set of experiments. The power levels indicated are multiples of the SPOPO threshold of $\sim$180 mW. It is clear from figure 7.7 that the idler spectrum changes with increasing input power along with the transfer fidelity.
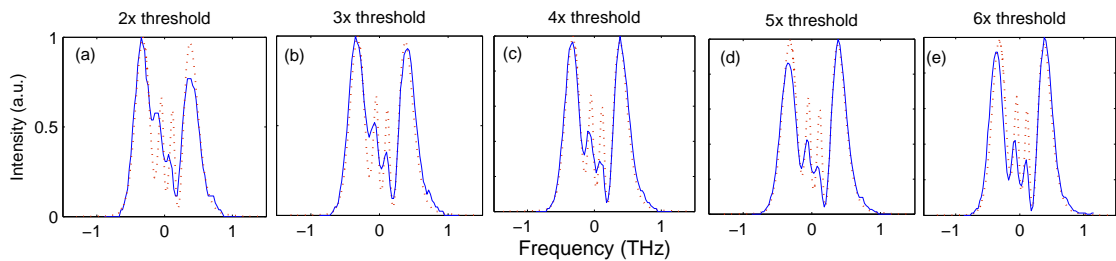

FIGURE 7.7: Measured idler (solid curve) and pump (dashed) spectra for increasing pump power as indicated.

The changing z values with increasing pump power are plotted in figure 7.8(b). An optimum is seen roughly at 4 times above threshold. This is in agreement with maximum pump depletion region as shown in fig. 7.8(a) supporting the numerical modelling results.

Output coupler reflectivity

The final resonator parameter that was investigated was the OC reflectivity. The resonator loss was varied by replacing the M4, as seen in fig. 7.2, with mirrors of different signal reflectivities. With increasing OC reflectivity, the resonator loss decreases and hence lower signal gain is needed to saturate to the cavity losses.

For this set of experiments, the SPOPO was operated at 2.5 times above the threshold due to a limit on the maximum available pump power. OCs with reflectivity of 100%,
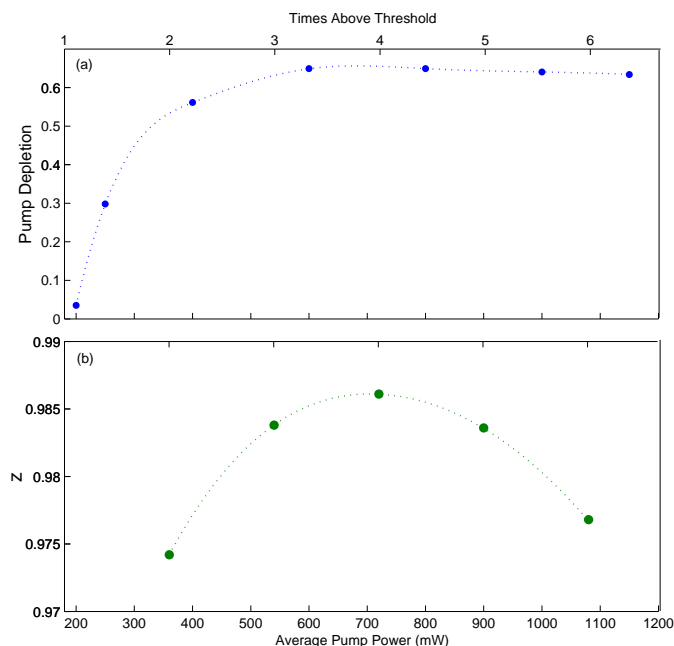
FIGURE 7.8: (a)Pump depletion as a function of average input power. Threshold value is 180 mW. (b)Spectral transfer fidelity as a function of average input pump power.
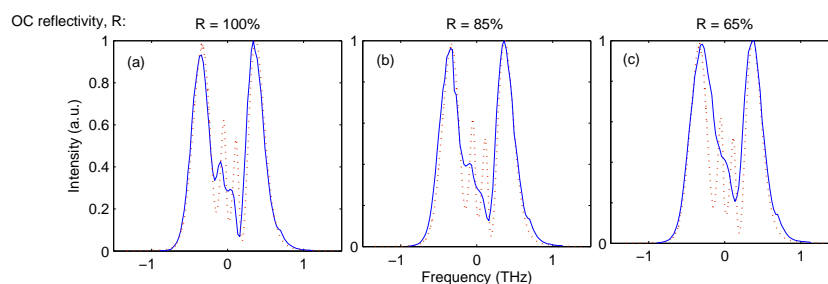
FIGURE 7.9: Measured idler spectra (solid) and pump spectrum (dashed) for OC reflectivity as indicated.

85% and 65% were used and the idler spectra seen for the different OC reflectivity are plotted in fig. 7.9. The resulting values of fidelity z achieved are 0.986, 0.983 and 0.960 corresponding to figures 7.9 (a), (b) and (c), respectively. From figure 7.9 and z values, it is apparent that the fidelity improves with increasing OC reflectivity, as expected from the numerical studies.

7.3.2 Temporal walk-off between interacting pulses

In this section, the effect of TWO between the interacting pulses: pump-signal and pump-idler will be investigated.

Pump and signal temporal walk-off

For the pump and signal wavelengths used here, the signal group velocity exceeds the pump group velocity. The signal thus walks through the pump in the PPLN altering the parametric transfer. This effect was compensated by tuning the cavity length, resulting in the pump arriving earlier in the crystal. As a result, timing-controlled walk-through of the signal was achieved in the PPLN.

The typical configuration where pump and signal TWO was ∼1 ps, with ∼48 fs pump and idler TWO, was used for this study. The signal bandwidth was restricted to ∼100 GHz at 1505 nm by placing an etalon in the resonator cavity. The cavity length was then detuned to ±80 μm, ±40 μm and 0 μm corresponding to ∓267 fs, ∓133 fs and 0 fs round trip mismatch respectively. The zero round trip mismatch described here corresponds to the resonator length which gives minimum threshold. The resultant idler spectra are shown in figure 7.10.
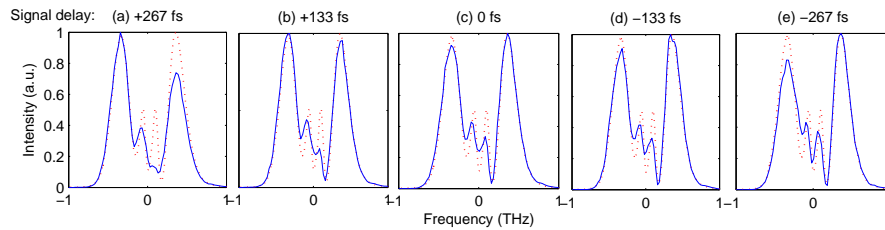
FIGURE 7.10: Measured idler (solid) and pump (dashed) spectra for increasing cavity lengths corresponding to the signal delays as indicated.

It is clear from figure 7.10 that as the cavity length increases, the higher frequency peak is transferred better than the lower frequency. This is because with longer cavity length, the signal arrives later than the pump at the crystal resulting in the trailing edge of the pump to be transferred more effectively. On the other hand, decreasing the cavity length results in the central peaks being transferred with more detail. Symmetric transfer occurs somewhere between 0 and +133 fs.

Pump and idler temporal walk-off

The pump and idler TWO was varied by changing the idler wavelength. The idler wavelength was altered by using different poling periods, as seen earlier in figure 7.4

and the signal bandwidth was maintained at $\sim$100 GHz. The input pump power was also maintained at three times above threshold value. Figure 7.11 shows the comparison between the idler spectra and the pump spectrum as the PPLN poling period is changed. The corresponding z values as a function of pump idler TWO are plotted in figure 7.12.
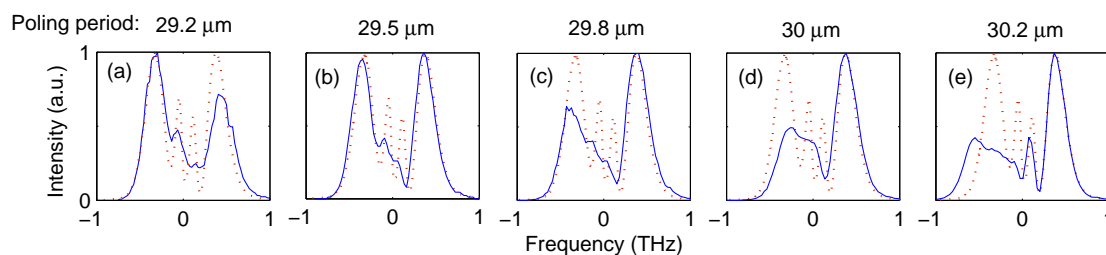
FIGURE 7.11: Measured idler (solid) and input pump (dashed) spectra for poling periods as indicated.
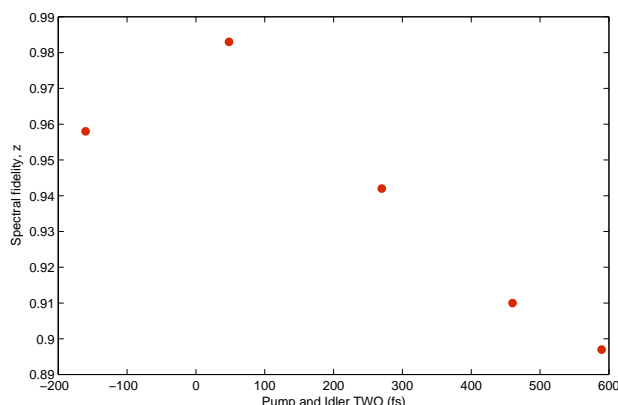
FIGURE 7.12: Spectral fidelity as a function of pump and idler TWO.

From the two figures it is evident that, as expected, the best transfer is achieved at near zero value of pump and idler TWO. As the TWO becomes more positive, the transfer of lower frequency peak is affected adversely. Correspondingly, as the TWO takes on a negative value, the higher frequency peak transfer is degraded.

To complete the study, the signal wavelength was maintained at 1600 nm and cavity length varied to as far as $\pm120\,\mu$m to see if any compensation effect could be achieved in this case. In other words, the idler wavelength was maintained at a certain value corresponding to a certain value of pump-idler TWO. The cavity length was then varied to see if it could compensate for the set pump-idler TWO. Various idler spectra thus

obtained are shown in figure 7.13. It is seen that increasing the lower frequency peak intensity impedes the central peaks' transfer without improving the overall z value.

FIGURE 7.13: Measured pump(dotted) and idler (solid line) spectra for signal delays as indicated, with pump and idler TWO 589 fs.
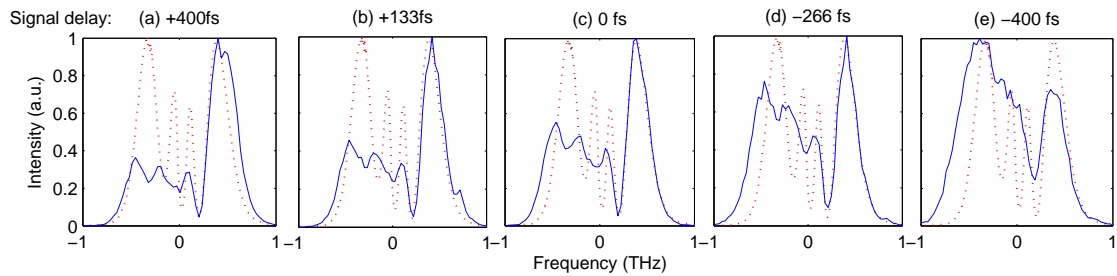
Finally, to draw a comparative result, z values were found for a choice of cavity length offsets at two different signal wavelengths of operation. This is plotted in figure 7.14. Results show that for 1600 nm, the maximum pump depletion is lower, and the rate of change of depletion with cavity length detuning is faster, as compared to those for 1505 nm. Even with a very little change in pump depletion value there is a drastic difference in the z values for this wavelength.

7.3.3 Demonstration of High Fidelity Transfer

To sum up the results and observations, the SPOPO was operated with an etalon in the resonator cavity reducing the signal FWHM to $\sim$80 GHz. The idler wavelength was maintained at 3440 nm, the pump and signal TWO compensated for by adjusting the cavity length, and an HR M4 was used. The input power was kept at four times above the threshold to maximise pump depletion.

It is apparent from figure 7.15 that with careful choice of experimental conditions the retrieved idler sonogram trace closely resembles the retrieved pump sonogram trace. This similarity is lost when no efforts are undertaken to preserve fidelity as in fig. 7.15(c). Active conservation of these factors has led to an order of magnitude difference in approach to a perfect fidelity of $z = 1$ in z value, from 0.85 to 0.985.

Having successfully demonstrated high fidelity pulse shape transfer from the NIR to the MIR in an SPOPO, the next step was to employ the fibre CPA system as described in
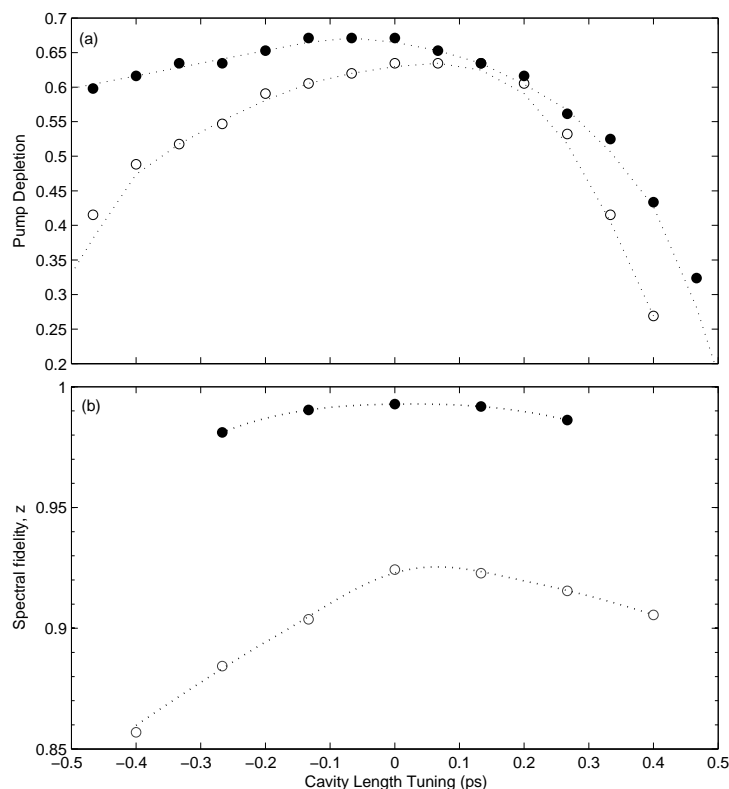
FIGURE 7.14: (a) pump depletion and (b) fidelity as function of cavity length. $\lambda_s = 1505\,\mathrm{nm}$(solid) and $1600\,\mathrm{nm}$(empty).

chapter 5 as the pump source for the OPO. The results obtained are described in the following section.

7.4 Synchronously pumped optical parametric oscillator and adaptive loop set-up

7.4.1 Experimental Set-up

The experimental set-up is shown schematically in fig. 7.16. It consists of a pump source, a femtosecond SPOPO and pulse diagnostic arrangements including a sonogram and an autocorrelator. The pump source is the fibre CPA system, described in detail in chapter 5 with the pulse repetition rate of $50\,\mathrm{MHz}$, average power of up to $7\,\mathrm{W}$, with possible pulse widths as short as $300\,\mathrm{fs}$ at a central wavelength of $\sim 1042\,\mathrm{nm}$. The required pump spot size within the OPO is obtained by combination of an appropriate telescopic arrangement
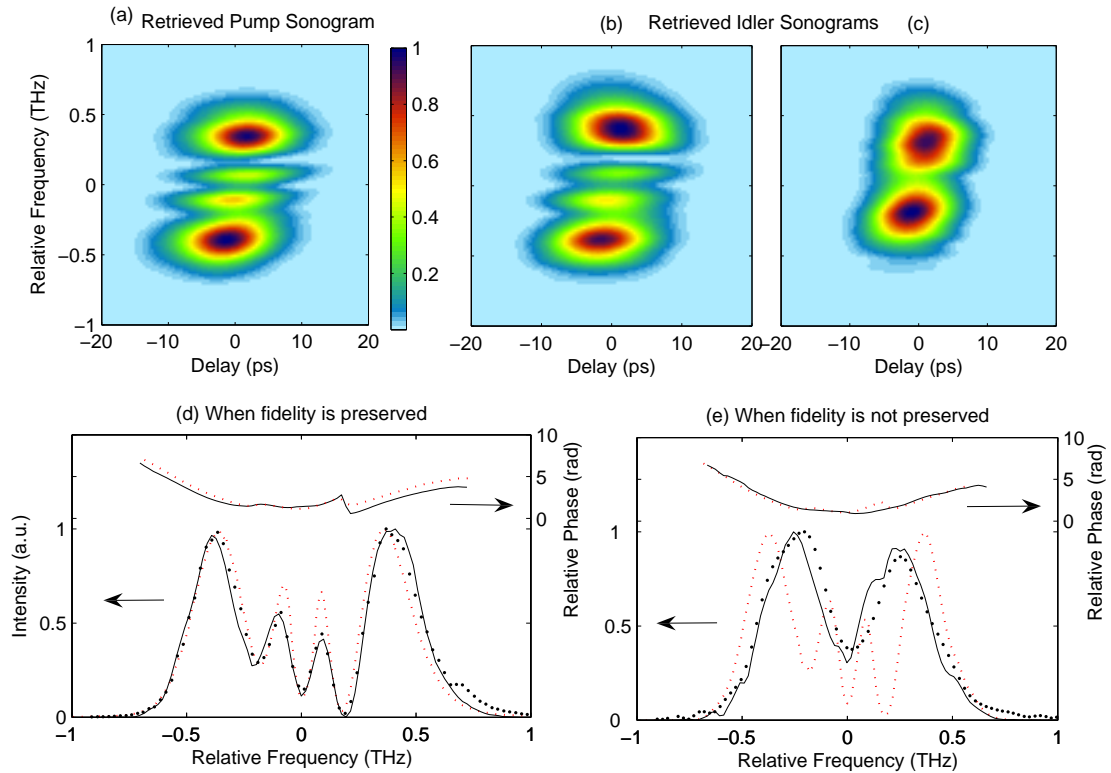
FIGURE 7.15: High fidelity parametric transfer(a)retrieved pump sonogram (b)retrieved idler sonogram where fidelity is preserved (c)retrieved idler sonogram where fidelity is not preserved (d)and(e) retrieved pump and phase (red-dashed) compared with measured (dotted) and retrieved (solid line) idler spectrum and phase (solid).

along with the focussing lens at the input of the OPO. The resonator length is set at $\sim3\,$m so as to be proportionate to the inverse of the repetition rate of the pump. Initially, a 5 mm long PPLN crystal was used to get the OPO oscillating. The pump beam spot size inside the crystal was maintained to be as close to the confocal length as possible; in this case, it was $\sim30\,\mu$m with an M^2 of approximately 1.2 in both the axes.

FIGURE 7.16: Schematic layout of the femtosecond OPO.

With the OPO oscillating and the input pump wavelength, $\lambda_p = 1043\,\text{nm}$, the oscillating signal wavelength, $\lambda_s = 1580\,\text{nm}$ the output idler wavelength was measured to be $\lambda_i = 3069\,\text{nm}$. The idler can be tuned by changing the grating on the PPLN and thus tuning the signal.

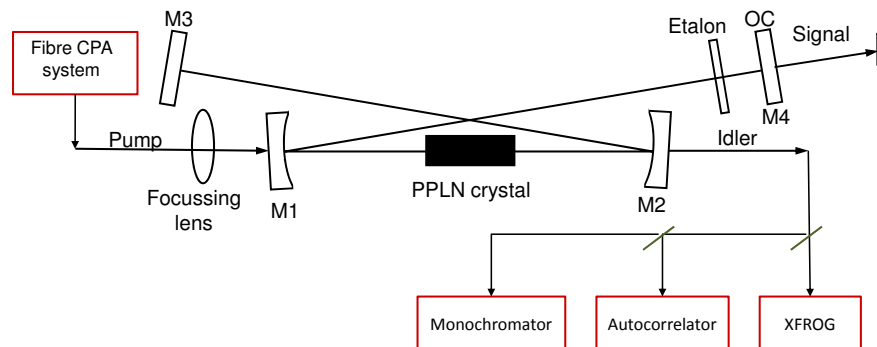The PPLN inside the cavity was later replaced by shorter, that is $3\,\text{mm}$ and $1\,\text{mm}$ crystals. This was to reduce the group velocity mismatch between the pulses. But on the negative side, the threshold of operation increases with decreasing crystal length. Moreover, the spot size inside the crystal had to be reduced to match the confocal length which increased the possible damage to the PPLN during alignment and operation.

7.4.2 Results and Discussion

With $1\,\text{mm}$ PPLN in the OPO cavity, the threshold was measured to be $\sim 1\,\text{W}$ with HR mirror (M4) for the signal. An OSA was used to measure the pump and signal wavelengths with a resolution of $0.1\,\text{nm}$, whereas a Bentham M300 Monochromator was employed to measure the idler spectrum with a resolution of $0.54\,\text{nm}$. The wavelength values obtained for the pump, signal and idler were $1042\,\text{nm}$, $1540\,\text{nm}$ and $3213\,\text{nm}$ respectively. The signal bandwidth was measured to be $7.8\,\text{nm}$.

Due to recurring damage to the $1\,\text{mm}$ crystal and high threshold power values of more than $1\,\text{W}$, the $5\,\text{mm}$ PPLN was used for the results presented here. Initially the input pump was adaptively shaped for minimum pulse duration. This shaped pump was fed as the input to the SPOPO with the $5\,\text{mm}$ crystal. The performance of the SPOPO was then characterised under the four different conditions: with or without phase profile applied to the pump and with either a HR mirror (M4) or an 85% OC for the signal for both the cases. Figure 7.17 gives the pump depletion for the case with HR mirror (M4), and figure 7.18 gives the idler slope efficiencies for this case. It is interesting to note that the idler slope efficiency seems to be higher for the case without the phase applied (blue) when an average slope of the data points is considered. But, when the values only up to 3 times above threshold are considered, the slope efficiencies are higher for the case with the phase applied, as expected. With $1043\,\text{nm}$ pump wavelength, the signal was tuned to a central wavelength of $1515\,\text{nm}$ as it was found to be the region of most stable

operation. The threshold of OPO oscillation was measured to be 57 mW of shaped pump and 100 mW of unshaped pump. The signal slope efficiency was not measured as it was an HR cavity, indicating practically no signal coming out of the cavity.
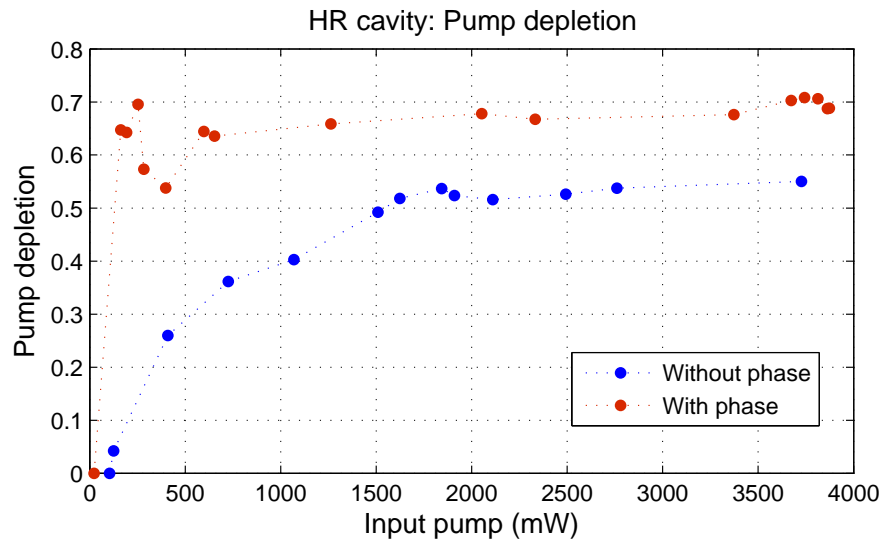

FIGURE 7.17: Pump depletion for 5 mm PPLN SPOPO with HR cavity for signal with (red) and without (blue) phase applied.

Similar sets of data were recorded for the cavity when an 85% transmitting OC for signal was used in the set-up in place of mirror M4. The measured threshold of operation in this case was 140 mW and 230 mW for the cases of with and without phase applied, respectively. The idler power in both the cases was measured to be around 210 mW with output signal power of 365 mW measured after the 85% OC. Figure 7.19 gives the pump depletion. From this figure we see that there is not much difference between shaped and unshaped results unlike in the case of fig. 7.17 where a distinctly better result is seen for the shaped data. The plot for the idler slope efficiencies is not shown here but values as high as 12% and 8% were obtained for measurements just outside the crystal and at point of measurement respectively for shaped pump input. For unshaped pump input, these values reduced to 11.7% and 7.95% respectively. The idler power was measured at the first convenient point in the set-up. The various optics between the output end of the crystal and point of measurement included the curved OPO cavity mirror, a lens, LWP filter and two highly reflecting gold mirrors. The losses associated
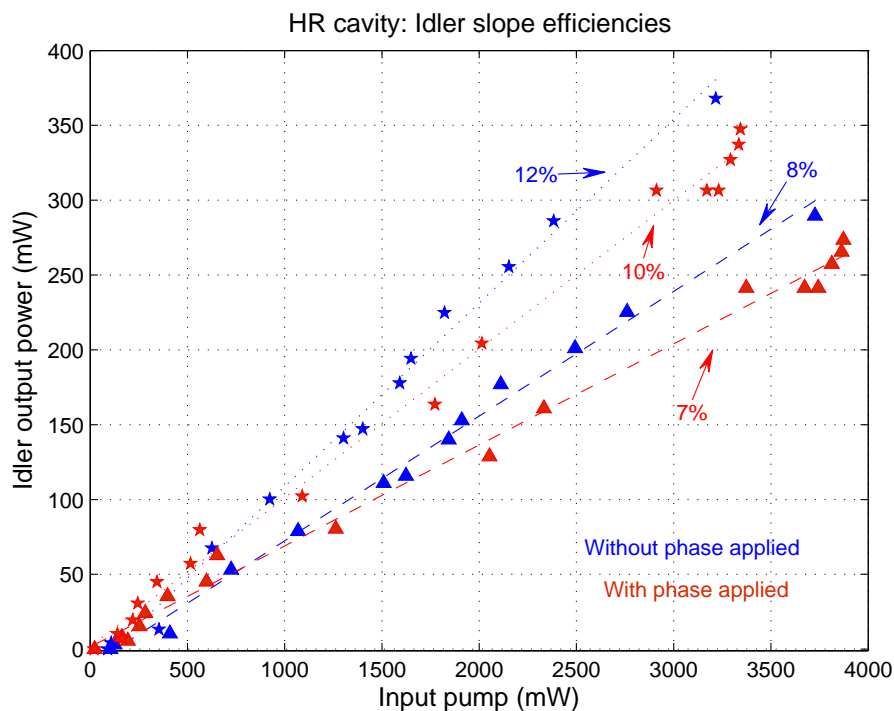
FIGURE 7.18: Idler slope efficiency for 5 mm PPLN SPOPO with HR cavity for signal. Calculated just outside the crystal (⋆) and recorded at a further away point of measurement outside the crystal (▲)

with these optics were measured and taking this into account, the power at the output of the crystal was estimated.
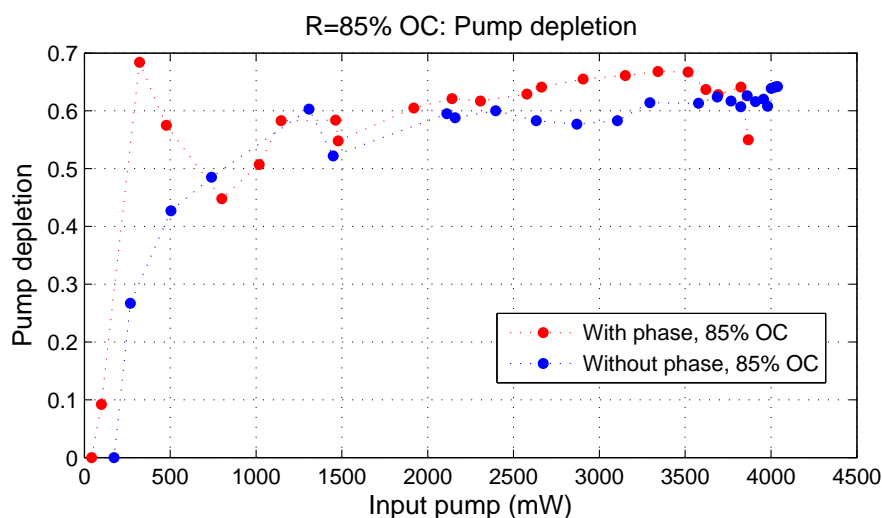
FIGURE 7.19: Pump depletion for 5 mm PPLN SPOPO with 85% OC for signal.

With these values for different thresholds for either HR or OC for signal, using the Findlay-Clay analysis, the internal cavity losses were calculated to be ~18%. It is

important to note that these results were taken without an etalon in the set-up. In order to control signal bandwidth, a birefringent filter had to be used which increased the threshold of operation for the OPO. Due to this increase in the threshold, it was practical that only a 5 mm PPLN crystal could be used in the cavity.

The adaptive loop was then incorporated to the entire set-up so that the OPO idler output was now used to give the feedback for the adaptive shaping instead of the pump. One arm of the interferometric autocorrelator for idler characterisation was blocked and the existing extended InGaAs detector in the set-up was used for TPA optimisation for idler pulse compression. Figure 7.20 gives the IAC trace for the shaped (green) and unshaped (blue) idler pulse. An improvement of 9 times was observed in the TPA signal. The threshold values were measured to be 1.2 W and 750 mW for unshaped and shaped pulses respectively. The idler power was 140 mW and 175 mW for the unshaped and shaped pulses respectively. The pulse width estimated from the AC trace width were calculated to be 372 fs and 507 fs for shaped and unshaped idler pulses respectively compared to the pump pulse durations of 364 fs and 716 fs.

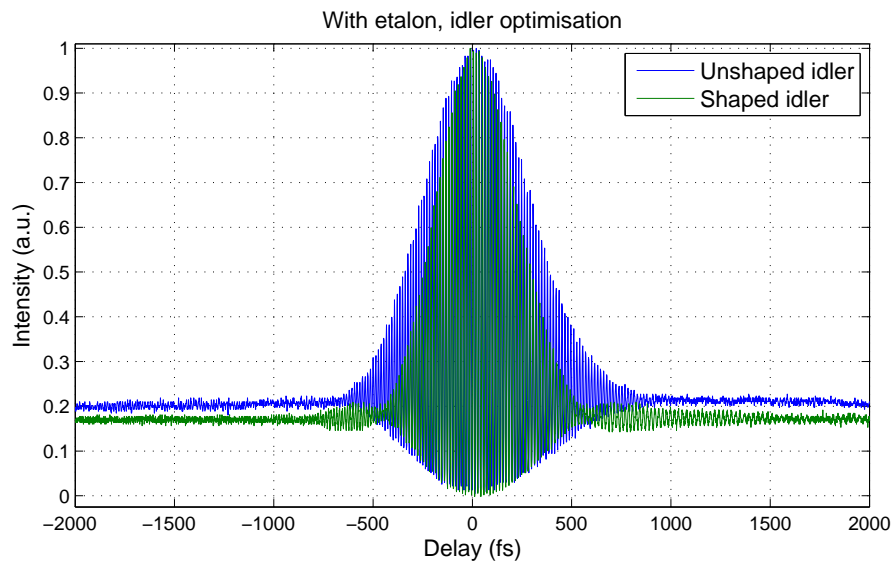FIGURE 7.20: Idler pulse compression with etalon in the OPO cavity.

It is worthwhile to note here that in this set-up the shaping occurs as early as in the amplifier chain to affect the pulse shape of the OPO output near the end of the chain. After initial verification that the adaptive loop was working even with this considerable long beam path, attempts were made to transfer the shape from the NIR to the MIR

pulse with high fidelity. As mentioned earlier, this was important for the proposed surface sum frequency generation and coherent control experiments.

In preparation, all the parameters were favourably adjusted as per the conclusions from the work presented in section 7.3. That is, cavity length was adjusted, HR mirrors were used in the cavity for the signal, a birefringent filter was used in the cavity to restrict signal bandwidth and the shortest possible crystal (5 mm) that could be used with available maximum pump power was employed. The temperature of the PPLN was maintained at 170°C.

To test the transfer of relatively complex pulses, the unshaped pump pulses were used as the input to the SPOPO. Figure 7.21 indicates the measured pump and idler spectra. The idler overall takes the structure of the pump but has failed to transfer all the small details.

FIGURE 7.21: Pulse shape transfer between unshaped pump and idler with birefringent filter in the cavity.

For a better understanding, the birefringent filter was removed from the cavity and the transfer studied once again. Figure 7.22 highlights the spectra obtained. The idler again takes the basic shape of the pump but picks up much less of the finer structure detail.

The reason for the lack of detailed structure shape transfer from the NIR to the MIR could be attributed to long crystal length and inappropriate etalon for signal bandwidth
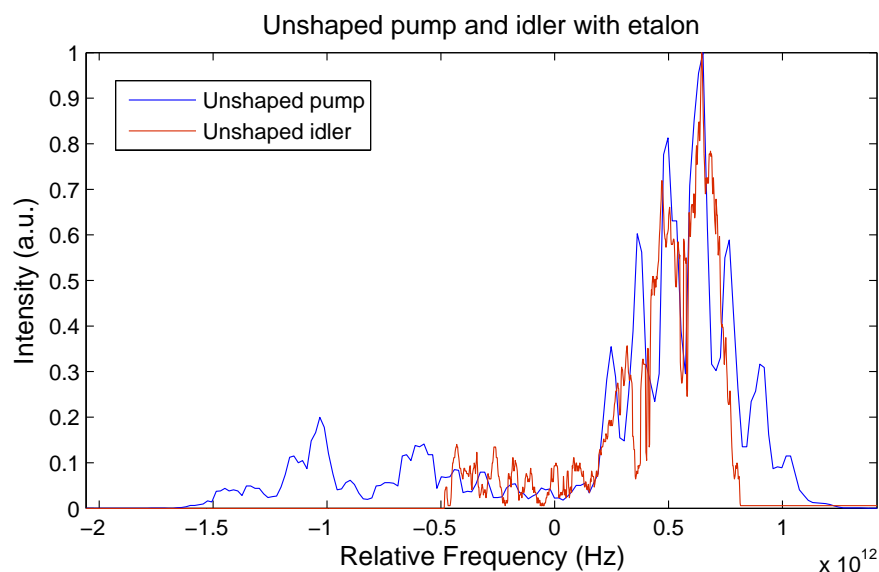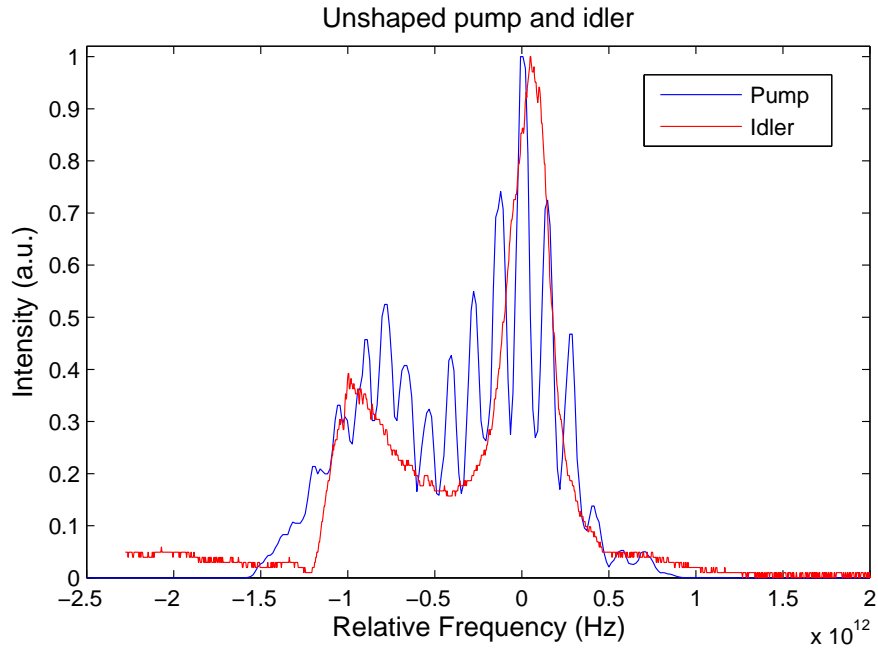
FIGURE 7.22: Pulse shape transfer between unshaped pump and idler without birefringent filter in the cavity.

restriction. The transfer is much worse in this case compared to the previous study due to bigger bandwidths. Another important thing to note here is that with time, the pump source had become highly unstable requiring thorough alignment more than once a week. Moreover, it needed to be realigned every hour to maintain the power levels. To add to this, even a slight touch to the resonator length had started affecting the signal considerably. The long beam paths coupling the fibre CPA to its compressor and then the OPO required additional optics and could be one of the causes of instability in the system. To verify this, the pump spectrum was measured at regular intervals during the day. The central wavelength along with the structure on the spectra changed considerably over a span of time less than even two hours. This could be one the reasons that the transfer of pulse shape was not as expected. If these stability problems could be overcome, the initial results (see fig 7.21 and fig. 7.22) are promising for pulse shape transfer and adaptively shaping the idler for applications such as the sum frequency generation discussed in the next chapter.

7.5 Summary

To summarise the results, in the first part of this chapter it was concluded experimentally that with careful choice of experimental conditions the retrieved idler sonogram trace closely resembled the retrieved pump sonogram trace. The transfer significantly degraded when no efforts were undertaken to preserve fidelity as in fig. 7.15(c). Active conservation of these factors has lead to an order of magnitude difference in approach to a perfect fidelity of $z = 1$ in z value, from 0.85 to 0.985.

In the second section, the pump source was replaced with the fibre CPA system to enable the use of power-scalable fiberised system as the pump source. Initial experiments for pulse shape transfer from the NIR to the MIR are promising along with positive results for adaptively shaping the idler from the femtosecond OPO at the end of the long system set-up. However, stability of the overall system needs to be improved.

References

[1] N. Bloembergen and A. H. Zewail, "Energy redistribution in isolated molecules and the question of mode-selective laser chemistry revisited," *Journal of Physical Chemistry* **88**(23), pp. 5459–5465, 1984.

[2] R. S. Judson and H. Rabitz, "Teaching lasers to control molecules," *Physical Review Letters* **68**(10), pp. 1500–1503, 1992.

[3] R. N. Zare, "Laser control of chemical reactions," *Science* **279**(5358), pp. 1875–1879, 1998.

[4] A. P. Peirce, M. A. Dahleh, and H. Rabitz, "Optimal-control of quantum-mechanical systems - existence, numerical approximation, and applications," *Physical Review A* **37**(12), pp. 4950–4964, 1988.

[5] R. J. Levis, G. M. Menkir, and H. Rabitz, "Selective bond dissociation and rearrangement with optimally tailored, strong-field laser pulses," *Science* **292**(5517), pp. 709–713, 2001.

[6] J. M. Dela Cruz, I. Pastirk, M. Comstock, V. V. Lozovoy, and M. Dantus, "Use of coherent control methods through scattering biological tissue to achieve functional imaging," *PNAS* **101**, pp. 16996–17001, 2004.

[7] G. Knippels, A. v. d. Meer, R. Mols, P. v. Amersfoort, R. Vrijen, D. Maas, and N. L.D., "Generation of frequency-chirped pulses in the far-infrared by means of a sub-picosecond free-electron laser and an external pulse shaper," *Optics Communications* **118**, pp. 546–550, 1995.

[8] L. Windhorn, T. Witte, J. S. Yeston, D. Proch, M. Motzkus, K. L. Kompa, and W. Fuss, "Molecular dissociation by mid-IR femtosecond pulses," *Chemical Physics Letters* **357**(1-2), pp. 85–90, 2002.

[9] D. J. Maas, D. I. Duncan, R. B. Vrijen, W. J. van der Zande, and L. D. Noordam, "Vibrational ladder climbing in NO by (sub)picosecond frequency-chirped infrared laser pulses," *Chemical Physics Letters* **290**(1-3), pp. 75–80, 1998.

[10] V. D. Kleiman, S. M. Arrivo, J. S. Melinger, and E. J. Heilweil, "Controlling condensed-phase vibrational excitation with tailored infrared pulses," *Chemical Physics* **233**(2-3), pp. 207–216, 1998.

[11] L. Windhorn, J. S. Yeston, T. Witte, W. Fuss, M. Motzkus, D. Proch, K. L. Kompa, and C. B. Moore, "Getting ahead of ivr: A demonstration of mid-infrared induced molecular dissociation on a sub-statistical time scale," *Journal of Chemical Physics* **119**(2), pp. 641–645, 2003.

[12] N. Belabas, J. P. Likforman, L. Canioni, B. Bousquet, and M. Joffre, "Coherent broadband pulse shaping in the mid infrared," *Optics Letters* **26**(10), pp. 743–745, 2001.

[13] T. Witte, K. L. Kompa, and M. Motzkus, "Femtosecond pulse shaping in the mid infrared by difference-frequency mixing," *Applied Physics B-Lasers and Optics* **76**(4), pp. 467–471, 2003.

[14] H. S. Tan and W. S. Warren, "Mid infrared pulse shaping by optical parametric amplification and its application to optical free induction decay measurement," *Optics Express* **11**(9), pp. 1021–1028, 2003.

[15] H. S. Tan, E. Schreiber, and W. S. Warren, "High-resolution indirect pulse shaping by parametric transfer," *Optics Letters* **27**(6), pp. 439–441, 2002.

[16] S. H. Shim, D. B. Strasfeld, E. C. Fulmer, and M. T. Zanni, "Femtosecond pulse shaping directly in the mid-IR using acousto-optic modulation," *Optics Letters* **31**(6), pp. 838–840, 2006.

[17] S. H. Shim, D. B. Strasfeld, and M. T. Zanni, "Generation and characterization of phase and amplitude shaped femtosecond mid-IR pulses," *Optics Express* **14**(26), pp. 13120–13130, 2006.

[18] N. A. Naz, H. S. S. Hung, M. V. O'Connor, D. C. Hanna, and D. P. Shepherd, "Adaptively shaped mid-infrared pulses from a synchronously pumped optical parametric oscillator," *Optics Express* **13**(21), pp. 8400–8405, 2005.

[19] J. Prawiharjo, H. S. S. Hung, D. C. Hanna, and D. P. Shepherd, "Theoretical and numerical investigations of parametric transfer via difference-frequency generation for indirect mid-infrared pulse shaping," *Journal of the Optical Society of America B-Optical Physics* **24**(4), pp. 895–905, 2007.

[20] J. Prawiharjo, H. S. S. Hung, D. C. Hanna, and D. P. Shepherd, "Numerical investigations of parametric transfer in synchronously pumped optical parametric oscillators for indirect mid-infrared pulse shaping," *Journal of the Optical Society of America B-Optical Physics* **24**, pp. 2484–2493, 2007.

[21] H. S. S. Hung, J. Prawiharjo, N. K. Daga, D. C. Hanna, and D. P. Shepherd, "Experimental investigation of parametric transfer in synchronously pumped optical parametric oscillators," *Journal of the Optical Society of America B-Optical Physics* **24**(12), pp. 2998–3006, 2007.

[22] I. G. Cormack, W. Sibbett, and D. T. Reid, "Rapid measurement of ultrashort-pulse amplitude and phase from a two-photon absorption sonogram trace," *J. Opt. Soc. Am. B* **18**(9), pp. 1377–1382, 2001.

[23] D. H. Jundt, "Temperature-dependent sellmeier equation for the index of refraction, n(e), in congruent lithium niobate," *Optics Letters* **22**(20), pp. 1553–1555, 1997.

Chapter 8

Future work and conclusion

8.1 Introduction

Once the adaptively shaped MIR femtosecond pulse generator is developed, the proposed coherent control experiment is to investigate the molecular orientation of surface water molecules using vibrational sum frequency spectroscopy (VSFS) [1, 2]. The water surface plays an important part in many biological processes, such as, protein folding and formation of lipid bilayers, so understanding more about the vapour-water interface is of great interest. Sum frequency generation (SFG) is used to study the details of molecular structure and dynamics at surfaces and interfaces. As SFG is highly surface selective, it is used to focus on the thin layer of a few atoms or molecules only near the surface/interface. The physical principle behind this is that SFG is an even-order nonlinear process and therefore does not exist in bulk media such as gases, liquids and isotropic solids which have inversion symmetry. However, at an interface between two such media, the inversion symmetry is broken, and the SFG optical signal can be generated and detected. Usually, a fixed visible beam and a tunable infra-red laser [3] is used for the VSFS experiments, in this coherent control experiment, the NIR pump and MIR idler are employed. This is a unique approach where, for the final coherent control experiments, the shaped MIR idler will be directly resonant with the -OH stretching mode at $\sim 3\,\mu$m.

With the femtosecond OPO set and working satisfactorily (see chapter 7), preliminary experiment involving adaptive pulse shaping for enhancement of sum frequency mixing on simple gold film molecules is carried out and described in sections 8.2 and 8.3. This work proceeded under the guidance of, and in collaboration with Prof. J. G. Frey and Dr. Sarah Stebbings of the Dept. of Chemistry, University of Southampton. Finally, the work presented in this thesis is summarised in section 8.4.

8.2 Experimental Set-up

The experimental apparatus for initial experiments for SFG employed the fibre-based CPA system as the laser source, operating at a central wavelength of 1042 nm (NIR) with the pulse duration of $\sim$350 fs, repetition rate of $\sim$50 MHz and 3 W average power as input to the SPOPO. The OPO uses a 3 mm PPLN as the nonlinear crystal which is tuned to generate idler (MIR) at $\sim$3.2 μm for this experiment. The experimental set-up for the SFG experiment is shown in fig. 8.1.
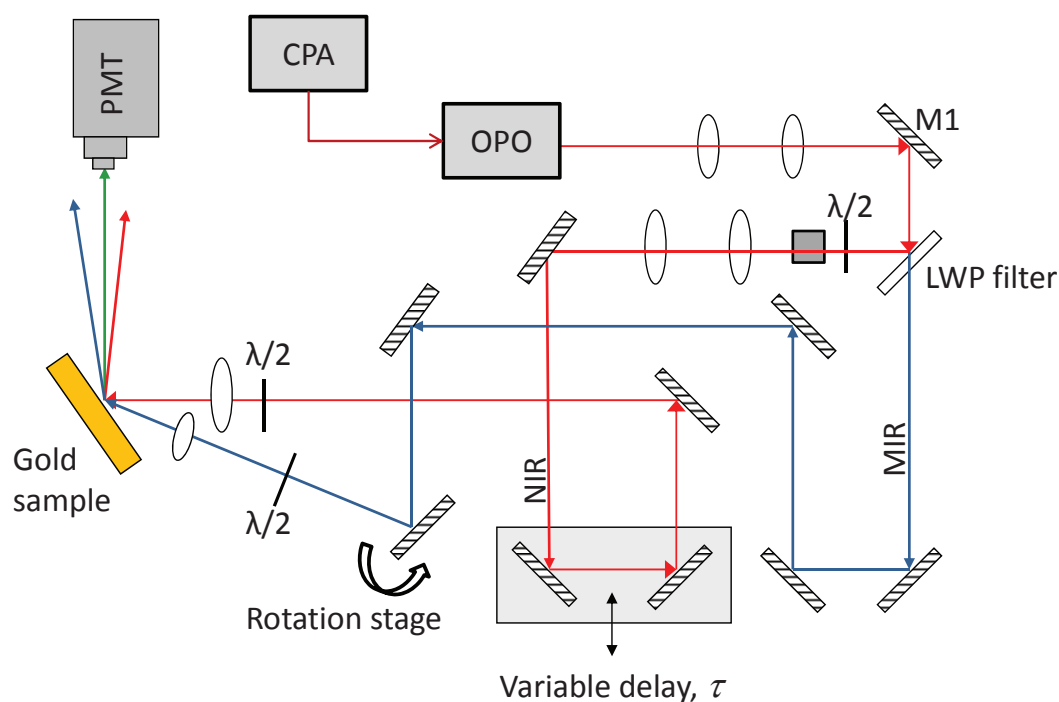

FIGURE 8.1: Experimental set-up for sum frequency generation.

Here, the NIR pump and the MIR idler pulses are spatially and temporally overlapped coming out of the OPO. The first pair of lenses is used to collimate the MIR. The two

beams are then separated using a long wave pass filter. A half-waveplate ($\lambda/2$) and a polarising beam-splitter are used in the NIR arm to allow a pure linear polarisation state to be incident upon the sample. A telescope is then used to collimate the NIR as shown in the figure. The path length of this arm can be varied using a variable delay stage, controlled by a motor as indicated. Another half-waveplate is then added to this arm to control the polarisation so that the NIR beam incident upon the gold sample is purely p-polarised [3], and a focussing lens is used to achieve a $1/e^2$ radius of $\sim 10\mu$m at the sample. It was ensured that the NIR beam was incident at an angle of 46 degrees to the sample normal. The M^2 for NIR was measured to be between 1.1-1.4.

The MIR path length was matched to the NIR path length and with an appropriate focussing lens, a 10μm spot size was obtained for the MIR as well. This beam was incident at 61 degrees to sample normal. These angles were chosen to be close to the angles as suggested by M.Bonn et.al [3] for SFG experiments. The gold sample itself was placed on a 3-axis translation stage so that its position could be fine-tuned. The M^2 for the MIR beam was measured to be 1.5.

Measured average powers of $800\,$mW of depleted NIR (that is, NIR at the output of the OPO when it is oscillating) and $\sim 50\,$mW of MIR were available at sample site for the experiments. For the first set-up indicated in fig. 8.1, which employed the MIR and the depleted NIR from the OPO, for sum frequency mixing (SFM), the peak intensities available were $I_{MIR} = 2\times10^9\,$W/cm^2 (P_{avg}=55$\,$mW, τ=350$\,$fs) and $I_{NIR} = 3.78\times10^{10}$ W/cm^2 (P_{avg}=1$\,$W, τ=350$\,$fs); whereas, Shen et.al [4] have mentioned using intensity as high as $\sim 10^{11}$ W/cm^2 for their experiments. Higher intensities for our set-up were not achievable due to the low damage threshold of the PPLN and MIR transmission efficiency of the SFG set-up which was as low as 10% due to the number of mirrors (average reflectivity of 95% at idler wavelength) used to guide the beam. However, the experiment was still carried out to see if these intensities could work.

The alignment and detection procedures that were carried out are described in the next section. No SFG signal was detected in any of the different procedures with this set-up. With no SFM signal detected with the first set-up, the set-up was reconfigured. Now, a part of the undepleted pump was taken before the OPO as the input to the SFG set-up,

instead of the depleted pump as indicated previously in fig. 8.1. The schematic of the modified set-up is shown in fig. 8.2.
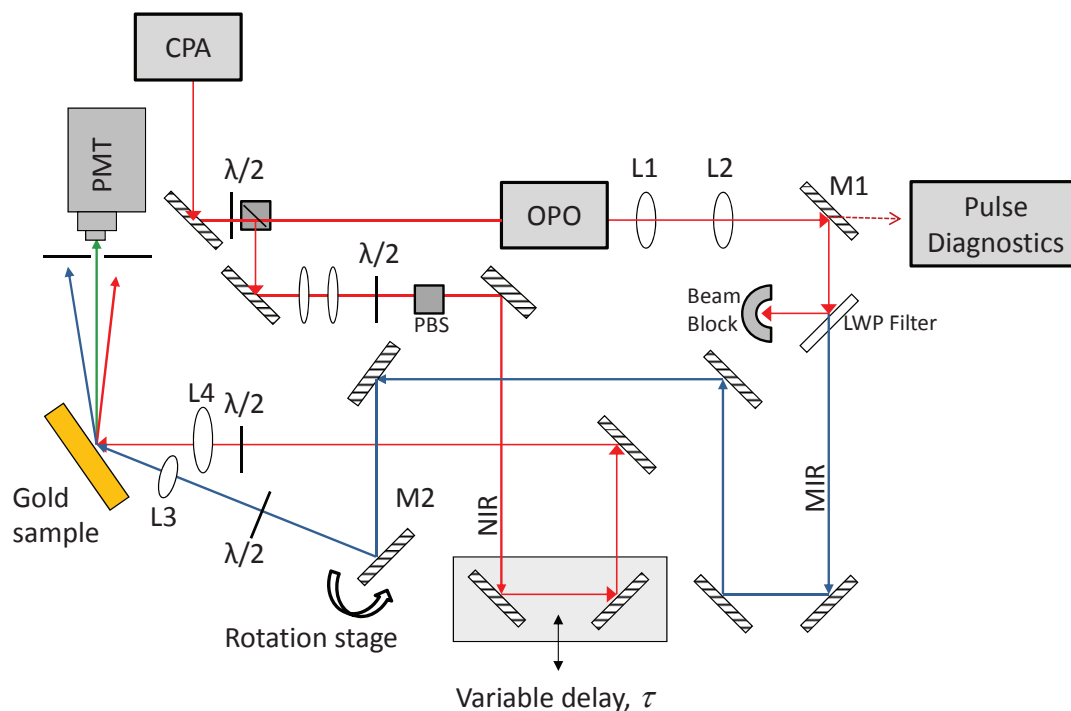
FIGURE 8.2: Modified experimental set-up for sum frequency generation. M1 is a flip-mirror.

Once again the same alignment and detection procedures were followed as with the first set-up. These are described in the following paragraphs.

Alignment procedure

A $200\,\mu$m pinhole was used to get maximum spatial overlap between the NIR and the MIR beams at the focus (sample site). The pinhole was first moved to achieve maximum NIR transmission. This was then fixed and the focussing lens for the MIR was moved around to get maximum MIR transmission through the same pinhole. After the alignment, the MIR lens was kept fixed for the rest of the experiment.

A GaAs detector was then placed where the beams overlapped spatially. This detector was used to obtain maximum temporal overlap. The translation stage in the NIR arm was moved until the SFM signal detected using GaAs detector was maximum. This procedure confirmed spatial and temporal overlap of the beams. The detector used here

peaked at $\sim$790 nm, which is close to the generated sum frequency of the NIR (1042 nm) and the MIR ($\sim$3200nm). This greatly helped in detecting the generated TPA signal as a result of one photon each from the NIR and the MIR. Furthermore, the detector did not respond to the SHG from the MIR and was much less responsive to the SHG from the NIR as well. A chopper was added to the MIR to ensure that the signal that was being maximised was indeed the SFG and not the SHG.

A lock-in amplifier along with the photo-multiplier tube (PMT), as shown, was used for signal detection at the calculated angle of 58 degrees to the normal, after the gold sample. Background light was minimised by covering the PMT with a black cloth. This improved the signal-noise ratio significantly. The PMT was set at roughly the estimated angle for generated signal. The gold sample was then tweaked a little to detect the signal. In another attempt, the gold sample was kept steady and the PMT was moved around instead. When these techniques did not work, in another try, the PMT was first set to detect the SHG generated from the NIR alone, keeping the MIR blocked. Once the PMT successfully detected the SHG from the NIR, the MIR arm was then 'unblocked' and the PMT was moved towards the expected direction for the SFG signal.

8.3 Results and Discussion

With the first set-up, the SHG signal of NIR was easily observed when either a PPLN or a 1 mm thick $LiIO_3$ crystal was placed at the focus or the sample site. This was then replaced by the gold sample, placed at the desired angle. SHG for the NIR was generated off the gold surface and conveniently detected using the PMT.

This SHG signal was adaptively optimised resulting in an 8 times improvement in the generated SH signal. Minimum detectable signal was generated with 30 mW of depleted NIR and 6 mW of undepleted pump, that is, when OPO was not oscillating. With the 'detection threshold' value in hand for the set-up, the numbers were scaled to calculate the expected threshold for SFM, keeping in mind the wavelength sensitivity for the PMT as well. This calculation is based on the equations shown below where subscripts p, i and s stand for pump, idler and sum frequency respectively.

For SHG signal:

$$\omega + \omega = 2\omega$$

$$I_{SHG} \sim [I(\omega_p)]^2 \omega_p^2$$

For SFG signal:

$$\omega_p + \omega_i = \omega_s$$

$$I_{SFM} \sim I(\omega_p).I(\omega_i).\omega_s^2$$

If we assume that all the beams have the same spot size and take into account the relative sensitivity of the PMT at the SFM and SHG wavelengths, we would expect a minimum $6\,\mathrm{mW}$ of idler for $30\,\mathrm{mW}$ of pump to be sufficient to observe a detectable SFM signal.

Comparing the two set-ups, much better SHG signal was observed with the modified set-up as compared to the previous one. SHG from NIR was easily observed when the gold sample was placed at the focus although SFG was still not observed. It was ensured that p-polarised light was used throughout the experiment. The possible causes for failure and the way forward is discussed in the following paragraphs.

The first cause appears to be the low intensities as mentioned earlier. According to experiments by Shen et.al [4], around $10^{11}\,\mathrm{W/cm^2}$ is needed whereas with this current set-up only up to $10^{10}\,\mathrm{W/cm^2}$ is available. The second cause could be considerable background light even after placing a black cover over PMT. The third reason appears to be that the PMT was not sensitive enough at the desired wavelength of $800\,\mathrm{nm}$. With the current PMT, this problem can be overcome by employing the SHG from NIR pump and the available MIR idler to generate blue light ($\lambda \sim 450\,\mathrm{nm}$). The available PMT was an order of magnitude more sensitive at $450\,\mathrm{nm}$ than at $800\,\mathrm{nm}$. It is worth noting here that the required SHG of the NIR for this solution can be easily generated using the $1\,\mathrm{mm}$ thick $LiIO_3$ crystal. With these new values, and applying similar scaling

calculations we would then expect that only $336\,\mu\text{W}$ of idler will be needed for detectable SFM signal generation, assuming 50% conversion efficiency from the NIR to the SHG.

These options appear promising for future experiments to generate sum frequency using an adaptively shaped fs-OPO powered by an ultrafast fibre-CPA system as a source. A new more sensitive PMT was later purchased but the experiment could not be repeated due to time constraints, and is left for future work.

8.4 Conclusion

The main aim of the work presented in this thesis was to build and develop an adaptively shaped advanced ultrafast laser source for application in coherent control experiments.

The motivation of such coherent control experiments and the background leading up to the development of an adaptively shaped fibre-based femtosecond CPA source was given in chapter 1. A theoretical overview of processes of pulse generation including optical parametric processes and pulse manipulation was given in chapter 2 before a discussion of pulse characterisation techniques such as such as the autocorrelator, XFROG and sonogram, in chapter 3. In particular, experimental results for MIR pulse characterisation using the CCS and XFROG were shown and a comparison of the two techniques was carried out. The experimental results of the comparison indicated that the XFROG technique is more sensitive and therefore the preferred choice of MIR pulse characterisation for spectral phase and amplitude retrieval. However, it is worthwhile to note that the experimental results of parametric transfer in chapter 7 use the CCS for characterisation as the experimental comparison of these two pulse characterisation techniques was carried out after the experiments reported in chapter 7.

Experimental investigation of adaptive phase control of the input pulse of a high pulse energy CPA system is presented in chapter 4. Two different CPA systems were investigated where one had a grating stretcher and the other had a fibre stretcher in the set-up. The output pulse for the grating stretcher setup was found to be significantly better in quality since the pulse shaper had to compensate for fewer nonlinear effects. In the fibre stretcher system, the shaper was placed before the stretcher in a pre-compensation

arrangement. However, it was found that full pre-compensation of large SPM broadening could not be achieved and therefore resulted in relatively poor pulse quality. The results also highlighted the limitations of the pulse shaper, particularly at high pulse energies. It was found that, at these energies, oscillatory structure on the pulse spectrum increased as a result of SPM, challenging the resolution limits of the shaper. Despite these limitations, high quality pulses up to $65\,\mu$J were obtained and it was demonstrated that adaptive pulse shaping improved the pulse quality in all situations.

Chapter 5 presented a detailed description and characterisation of a fibre-based CPA system with adaptive phase and amplitude shaping, which was then tested for its average power scalability while maintaining very high quality pulses of $\sim$300 fs duration. In this case, the fibre CPA system produced a train of pulses with an average power of 12.6 W at 50 MHz repetition rate. These were compressible to pulses of 170 fs duration. In chapter 6 the versatility of adaptive pulse pre-shaping technique to generate high-quality pulse train with variable repetition rate and energy in a fibre CPA system was highlighted. The fibre CPA set-up for this experiment included a 1 km fibre stretcher and pulses with a B-integral reaching as high as 2.2π rad were successfully shaped.

Chapter 7 was divided in two main parts. The experimental work described in the first part aimed to investigate the parameters that affect parametric transfer in an SPOPO. In particular, effects of signal bandwidth, output coupler reflectivity, input pump power, cavity length tuning and pump and idler temporal walk-off were investigated. By considering all these factors high fidelity transfer from the near-infrared pump to the mid-infrared idler was demonstrated. In the second part of the chapter, the adaptively shaped fibre CPA system, described in detail in chapter 5, was used as the pump source, instead of the picosecond Nd:YLF source, for a femtosecond OPO to demonstrate adaptive shaping. Initial experiments for pulse shape transfer from the NIR to the MIR are promising along with positive results for adaptively shaping the idler from the femtosecond OPO at the end of the long system set-up. However, stability of the overall system needs to be improved for future experiments.

With the successful demonstration of an adaptively shaped femtosecond MIR pulse generator, preliminary experiments were undertaken to generate sum frequency from

the surface of a gold film as described in the first part of this chapter. Although the sum frequency could not be generated, second harmonic was easily generated and future possible line of action for successful completion of the experiment has been discussed.

For the future, along with surface sum frequency generation, further power scaling of the fibre CPA system is anticipated for which a second power amplifier stage will be used. For the SPOPO, it is expected that more novel PPLN crystals, such as MgO-doped PPLN [5] may be used to enhance the tuning range of the adaptive MIR source. Employing the adaptively shaped ultrafast pulse generator for various other applications like supercontinuum generation is also of interest.

References

[1] A. G. F. de Beer and S. Roke, "Sum frequency generation scattering from the interface of an isotropic particle: Geometrical and chiral effects," *Physical Review B* **75**, 2007.

[2] G. L. Richmond, "Molecular bonding and interactions at aqueous surfaces as probed by vibrational sum frequency spectroscopy," *Chemical Reviews* **102**(8), pp. 2693–2724, 2002.

[3] M. Bonn, H. Ueba, and M. Wolf, "Theory of sum-frequency generation spectroscopy of adsorbed molecules using the density matrix method - broadband vibrational sum-frequency generation and applications," *Journal of Physics-Condensed Matter* **17**(8), pp. S201–S220, 2005.

[4] N. Ji, V. Ostroverkhov, C. S. Tian, and Y. R. Shen, "Characterization of vibrational resonances of water-vapor interfaces by phase-sensitive sum-frequency spectroscopy," *Physical Review Letters* **100**(9), p. 096102, 2008.

[5] H. Ishizuki, I. Shoji, and T. Taira, "High-energy quasi-phase-matched optical parametric oscillation in a 3-mm-thick periodically poled mgo:linbo$_3$ device," *Opt. Lett.* **29**, pp. 2527–2529, 2004.

Appendix A

Publications

Journal papers

1. J.Prawiharjo, N.K.Daga, R.Geng, J.H.V.Price, D.C.Hanna, D.J.Richardson, D.P.Shepherd, "High fidelity femtosecond pulses from an ultrafast fiber laser system via adaptive amplitude and phase pre-shaping," Optics Express 2008 Vol.16(19) pp.15074-15089.

2. F.He, H.S.S.Hung, J.H.V.Price, N.K.Daga, N.Naz, J.Prawiharjo, D.C.Hanna, D.P.Shepherd, D.J.Richardson, J.W.Dawson, C.W.Siders, C.P.J.Barty, "High energy femtosecond fiber chirped pulsed amplification system with adaptive phase control, " Optics Express 2008 Vol.16(8) pp.5813-5821.

3. H.S.S.Hung, J.Prawiharjo, N.K.Daga, D.C.Hanna, D.P.Shepherd, "Experimental investigation of parametric transfer in synchronously pumped optical parametric oscillators, " Journal of the Optical Society of America B (JOSA B) 2007 Vol.24(12) pp.2998-3006.

Contributions to Conference Proceedings

1. N.K.Daga, F.He, H.S.S.Hung, N.Naz, J.Prawiharjo, D.C.Hanna, D.J.Richardson, and D.P.Shepherd, "Adaptive phase shaping in a fiber chirped pulse amplification system," in Proc. Ultrafast Phenomena XVI, P.Corkum, S.De Silvestri, K.A.Nelson, E.Riedle, R.W.Schoenlein, eds. Springer Series in Chemical Physics , Vol.92, pp. 953-955, 2008.

Conference publications

1. J. Prawiharjo, F. Kienle, N.K. Daga, D.C. Hanna, D.J. Richardson, D.P. Shepherd, "High-quality energy-scalable femtosecond pulses from a fibre-based chirped pulse amplification system via adaptive pulse shaping," CLEO/Europe-EQEC 2009 Munich 14-19 Jun 2009 CJ9.5 (Invited)

2. D.P.Shepherd, N.K.Daga, R.Geng, Hanna D.C., H.S.S.Hung, J.Prawiharjo, "Adaptive pulse shaping of ultrafast mid-IR optical parametric oscillators," LPHYS '08 Trondheim 30 Jun - 4 Jul 2008 (Invited)

3. N.K.Daga, F.He, H.S.S.Hung, J.Prawiharjo, D.C.Hanna, D.J.Richardson, D.P.Shepherd, "Adaptive phase shaping in a fiber chirped pulse amplification system, " Ultrafast Phenomena Stresa 9-13 Jun 2008 TUEIIb.4

4. F.He, H.S.S.Hung, N.K.Daga, N.Naz, J.Prawiharjo, J.H.V.Price, D.C.Hanna, D.P.Shepherd, D.J.Richardson, J.W.Dawson, C.W.Siders, C.P.J.Barty, "High energy femtosecond fiber chirped pulse amplification system with adaptive phase control," CLEO/QELS 2008 San Jose 4-9 May 2008 CThB5

5. H.S.S.Hung, J.Prawiharjo, N.K.Daga, D.C.Hanna and D.P.Shepherd, "Parametric transfer in a synchronously pumped optical parametric oscillator," International Laser Physics Workshop (LPhys '07) Leon, Mexico 20-24 Aug 2007.

6. J.Prawiharjo, H.S.S.Hung, N.K.Daga, D.C.Hanna, D.P.Shepherd, "Parametric transfer in a synchronously pumped optical parametric oscillator: toward coherent control," 6th ISMOA 2007 Bandung, Indonesia 6-10 Aug 2007 (Invited).

7. H.S.S.Hung, J.Prawiharjo, N.K.Daga, D.C.Hanna, D.P.Shepherd, "Spectral phase and amplitude measurements of parametric transfer in a SPOPO," CLEO/QELS 2007 Baltimore 6-11 May 2007 CTuM4.